The BABAR Light Pulser System

Philip James Clark

Thesis submitted for the degree of Doctor of Philosophy

The University of Edinburgh

To my parents

Abstract

The *BABAR* experiment and the PEP-II e^+e^- collider at SLAC in California started taking data in May 1999. The aim of the experiment is to study *CP* violation in the B meson system. A central part of the *BABAR* detector is the CsI(Tl) electromagnetic calorimeter. To make precision measurements with a calorimeter in a high luminosity environment requires that the crystals are well calibrated and continually monitored for radiation damage. However, this should not impact the total integrated luminosity. To achieve this goal a fibre-optic light pulser system was designed. The light sources chosen were xenon flash lamps. A novel light distribution method was developed using an array of graded index microlenses. Initial results from performance studies are presented.

Declaration

This work represents the efforts of many members of the *BABAR* collaboration at SLAC, in California. I have been an integral part of a small team of people who designed and built a fibre optic light pulser calibration and monitoring system for the *BABAR* calorimeter. The writing of this thesis is entirely my own work.

Acknowledgements

Firstly, I would like to thank my supervisor Steve Playfer who patiently guided me throughout my research. Together we built a hardware system to meet the design requirements of the calorimeter. The *BABAR* detector was built in a short period of time and this was not easy.

My first enthusiasm for the subject came from Ken Peach whose passion for the subject rubbed off not a little on myself. I am grateful to him for inviting me to work at the University of Edinburgh.

In the initial stages of my PhD, Derek Newman-Coburn and Jim Lidbury provided me with a lot of encouragement and inspired some confidence in myself to build hardware. Sadly, Derek died in 1997 and he is very much missed by the community. In addition, Jim Lidbury also had to leave the experiment at around the same time. They were both heavily involved in the design of the calorimeter and it was a blow to lose them.

Jim King and Andrew Downie provided workshop support throughout. Andrew was particularly helpful. There were times when he manufactured more than could be reasonably expected of him so that I could meet a deadline. I particularly enjoyed many technical discussions with him in the workshop. A big thank you to Will Hossack for the loan of various optical components and for his helpful advice.

It has been a great pleasure to work alongside many very efficient and hardworking physicists. Two people who particularly stand out are Martin Kocian and Bernd Lewandowski. There are many other people to whom I am grateful. A few of these are: Steve McMahon for his help and advice, Francesca di Lodovico for helping me understand the Bhabha and minimum-ionising particle calibrations, Roland Bernet for his help with many things especially electronics, and lastly James Swain who helped considerably with the analysis of the large amounts of light pulser data taken in 1999.

Thank you to my family for their continuous support. I am very grateful to Ian Knowles for his help with some of the more theoretical aspects of particle physics, for providing a sharp sense of humour, and for much beer drinking! Thanks to Juliana for introducing me to music, Lavazza coffee, and Bajadera. Thank you to Courtney for patiently putting up with me, especially when I was working excessively long hours, talking about linux incessantly, and spending a disproportionate amount of time thinking about physics.

Lastly, I am grateful to PPARC for the support provided for the duration of my PhD.

Contents

List of Tables

List of Figures

1

Introduction

It was long thought that CP symmetry was exact in nature and that only theories which had this property could be viable descriptions of the world. The observation of the CP violating decay $K_L \to \pi\pi$ by Christenson, Cronin, Fitch and Turlay in 1964, shattered this view. Since that time, much effort has gone into studying the nature of CP violation. It is understood that it is a crucial feature of any theory that attempts to explain the asymmetry between matter and anti-matter in the Universe starting from initially symmetric conditions. It is also well understood that CP violation is a natural feature of the three generation Standard Model of elementary particle physics. However, this sector of the Standard Model is not well tested and so far the effect has not been observed in any other system than the neutral kaon system. In addition, it seems that the Standard Model does not generate enough matter-antimatter imbalance to produce the baryon number asymmetry observed in the Universe. Hence, it is important that this effect is investigated further. The *BABAR* experiment is designed specifically to study CP violation in the B meson system for the first time.

In the B meson system many CP violating effects are expected to manifest themselves, some of which are very cleanly predicted by the Standard Model. The *BABAR* experiment should be able to make enough independent measurements to directly test the Standard Model predictions. The possibility that new physics beyond the Standard Model is playing an important rôle in CP violation is still open and may even be required, given the matter-antimatter discrepancy mentioned above. This makes the investigation of CP violation in the B meson system fascinating. At the very least, it will allow accurate measurements of some of the remaining parameters of the Standard Model, parameters as fundamental as the quark masses themselves. If the results are inconsistent with Standard Model predictions then they will provide information about physics beyond the Standard Model. CP violation is directly linked to the mass-generating mechanism through the CKM matrix and therefore has fundamental implications for particle physics.

The PEP-II accelerator will collide beams of unequal energy and so will Lorentz boost the centre-of-mass frame. The beam energies are tuned to the $\Upsilon(4S)$ resonance. The B mesons produced have appreciable velocities in the lab frame, enabling their decay lengths to be measured. From these we can extract their relative decay times and measure time-dependent CP asymmetries. The *BABAR* detector has excellent vertex resolution which is crucial for measuring the flight times; a low mass drift chamber which can track particles over a wide range of momenta; and a specially designed Čerenkov-ring particle identification system, which is necessary for tagging the B meson flavour. One sub-detector which is essential for the experiment is the *BABAR* electromagnetic calorimeter which is constructed from CsI(Tl)

crystals to give excellent photon energy resolution. The branching ratios are small for the exclusive B decays which are CP eigenstates. Therefore the *BABAR* experiment must be able to reconstruct neutral particles with high efficiency over a large energy range. To achieve this requires that the calorimeter be well calibrated and continually monitored. A fibre-optic light pulser system was proposed with just these characteristics. It was designed to be a fast diagnostic tool which could monitor very precisely radiation damage, and measure any relative changes which may occur in the calorimeter between successive runs. This allows the calorimeter to be continually checked between other absolute calibrations which take longer periods of time and occur less frequently.

2

CP violation in the *B* meson System

2.1 Introduction

In this chapter we will discuss some of the basic theory of *CP* violation. We start by looking at a generic neutral meson system and develop a general formalism for mixing and *CP* violation. The first specific system of particles which we will discuss is the neutral K meson system. This is the only place where *CP* violation has been observed to date. Then we will look at the different manifestations of *CP* violation which are possible in the B meson system. We will then turn to consider the current interpretation of *CP* violation in the Standard Model with a look at some of the bounds on the parameters given by experiments so far. Lastly we will discuss *CP* violation beyond the Standard Model.

2.2 The general phenomenology of mixing and *CP* violation

2.2.1 General formalism for mixing

The discussion in this section is general and may refer to either K^0, D^0, B^0, or B_s^0 meson pairs. Consider a system of two neutral pseudo-scalar mesons, P^0 and $\overline{P}^0$, which have opposite flavour content. They are assumed to be stable with respect to the strong and electromagnetic interactions and to decay only via the weak interaction. Since the weak interaction does not conserve flavour it is possible for P^0 and $\overline{P}^0$ to have real and virtual transitions to the *same* common state n. This allows P^0 and $\overline{P}^0$ to oscillate between themselves via this common state, before finally decaying. This is called mixing.

We will represent the two charge conjugate states, which are eigenstates of the strong and electromagnetic Hamiltonian, $H_0 = H_s + H_{em}$, by $|P^0\rangle$ and $|\overline{P}^0\rangle$. The flavour changing transitions $\langle \overline{P}^0|\widehat{T}_0|P^0\rangle$ and $\langle P^0|\widehat{T}_0|\overline{P}^0\rangle$, where $\widehat{T}_0$ represents the transition operator, are not possible and the matrix elements are zero. However, when the weak Hamiltonian, $\widehat{H}_w$, is turned on the mixing transitions $\langle \overline{P}^0|\widehat{T}_w|P^0\rangle$ and $\langle P^0|\widehat{T}_w|\overline{P}^0\rangle$ become possible. This means $|P^0\rangle$ and $|\overline{P}^0\rangle$ are not eigenstates of the total Hamiltonian $H = H_0 + H_w$. They are not stationary states, nor simply decaying states, and do not have a straightforward $e^{-iEt/\hbar}$ time dependence. In general both $|P^0\rangle$ and $|\overline{P}^0\rangle$ mix and decay to other states. Therefore we

would like a formalism to describe the evolution of a state of the general form:

$$|\psi(t)\rangle = a(t)|P^0\rangle + b(t)|\bar{P}^0\rangle + c_1(t)|n_1\rangle + c_2(t)|n_2\rangle + c_3(t)|n_3\rangle + \dots \tag{2.1}$$

where $n_1, n_2, \dots$ are the states to which either P^0 or $\bar{P}^0$ may decay and t is the proper time *i.e.* the time as measured in the P^0–$\bar{P}^0$ rest-frame. The evolution of such a state is very complicated. It is simplified greatly if we are only interested in calculating $a(t)$ and $b(t)$, if only $a(t)$ and $b(t)$ are non-zero at $t = 0$, and if we only consider times t greater than the strong interaction time-scale. This is called the Wigner-Weisskopf approximation [1, 2].

Consider a state, $|\psi(t)\rangle$ at proper time t, which has evolved from a linear combination of $|P^0\rangle$ and $|\bar{P}^0\rangle$ states at $t = 0$, such as a beam of oscillating and decaying neutral mesons. If we take $P^0(t)$ and $\bar{P}^0(t)$ to be the probability amplitudes of having a P^0 or $\bar{P}^0$ meson at time t we can represent this as

$$|\psi(t)\rangle = P_0(t)|P^0\rangle + \bar{P}_0(t)|\bar{P}^0\rangle \tag{2.2}$$

The time dependence of $P^0(t)$ and $\bar{P}^0(t)$ is given by the coupled Schrödinger equation:

$$i\hbar\frac{d}{dt}\begin{pmatrix} P^0(t) \\ \bar{P}^0(t) \end{pmatrix} = \begin{pmatrix} H_{11} & H_{12} \\ H_{21} & H_{22} \end{pmatrix}\begin{pmatrix} P^0(t) \\ \bar{P}^0(t) \end{pmatrix} \tag{2.3}$$

with $H_{11} = \langle P^0|\widehat{T}_w|P^0\rangle$, $H_{22} = \langle \bar{P}^0|\widehat{T}_w|\bar{P}^0\rangle$, $H_{12} = \langle P^0|\widehat{T}_w|\bar{P}^0\rangle$, $H_{21} = \langle \bar{P}^0|\widehat{T}_w|P^0\rangle$.

This matrix H is not in general Hermitian *i.e.* H_{11},$H_{22} \notin \mathbb{R}$ and $H_{12} \neq H_{21}^*$, and H is referred to as the *effective* Hamiltonian. *CPT* conservation implies that the diagonal terms are equal, $H_{11} = H_{22}$. As for every matrix, H can be split into a Hermitian, and an anti-Hermitian part giving

$$H = M - \frac{i}{2}\Gamma \tag{2.4}$$

where $M = M^\dagger$ and $\Gamma = \Gamma^\dagger$. M is called the Hermitian mass matrix, and Γ the decay matrix. The mass matrix M is due to contributions from processes involving intermediate virtual states (the so-called dispersive part). The decay matrix Γ is due to processes involving intermediate real states (the so-called absorptive part).

Equation (2.3) can be diagonalised using linear combinations of the $|P^0\rangle$ and $|\bar{P}^0\rangle$ basis.

$$p|P^0\rangle \pm q|\bar{P}^0\rangle \tag{2.5}$$

The eigenvalues are $\lambda_\pm = H_{11} \pm (H_{12}H_{21})^{1/2}$. The corresponding eigenvalue equations give

$$\frac{q}{p} = \left(\frac{H_{21}}{H_{12}}\right)^{1/2} = \left(\frac{M_{12}^* - i\Gamma_{12}^*/2}{M_{12} - i\Gamma_{12}/2}\right)^{1/2} \tag{2.6}$$

which determines q/p up to a sign.

The linear combinations which diagonalise equation (2.3) are defined by convention:

$$|P^0_{1,2}\rangle \equiv \frac{1}{\sqrt{|p^2| + |q^2|}} \{p|P^0\rangle \pm q|\overline{P}^0\rangle\} \tag{2.7}$$

The time evolution of these basis states is now straightforward:

$$|P^0_1(t)\rangle = P_1(t)|P^0_1\rangle \qquad P_1(t) = e^{-i(m_1 - \frac{i}{2}\Gamma_1)t} \tag{2.8}$$

$$|P^0_2(t)\rangle = P_2(t)|P^0_2\rangle \qquad P_2(t) = e^{-i(m_2 - \frac{i}{2}\Gamma_2)t} \tag{2.9}$$

where

$$m_{1,2} = M_{11} \pm \mathrm{Re}\sqrt{H_{12}H_{21}} \tag{2.10}$$

$$\Gamma_{1,2} = \Gamma_{11} \mp 2\,\mathrm{Im}\sqrt{H_{12}H_{21}} \tag{2.11}$$

It is useful to define

$$\Delta m \equiv m_1 - m_2 \tag{2.12}$$

$$\Delta\Gamma \equiv \Gamma_1 - \Gamma_2 \tag{2.13}$$

which give:

$$\Delta m - \frac{i}{2}\Delta\Gamma = 2\sqrt{H_{12}H_{21}} \tag{2.14}$$

Solving for $|P^0\rangle$ and $|\overline{P}^0\rangle$ gives the time evolution of the states formed by the strong or electromagnetic interaction at $t = 0$.

$$|P^0(t)\rangle = \frac{\sqrt{|p^2| + |q^2|}}{2p} \{P_1(t)|P^0_1\rangle + P_2(t)|P^0_2\rangle\} \tag{2.15}$$

$$|\overline{P}^0(t)\rangle = \frac{\sqrt{|p^2| + |q^2|}}{2q} \{P_1(t)|P^0_1\rangle - P_2(t)|P^0_2\rangle\} \tag{2.16}$$

This can be alternatively expressed as

$$|P^0(t)\rangle = f_+(t)|P^0\rangle + \frac{q}{p} f_-(t)|\overline{P}^0\rangle \tag{2.17}$$

$$|\overline{P}^0(t)\rangle = \frac{p}{q} f_-(t)|P^0\rangle + f_+(t)|\overline{P}^0\rangle \tag{2.18}$$

where

$$f_\pm(t) = \frac{1}{2}\left(e^{-i(m_1 - \frac{i}{2}\Gamma_1)t} \pm e^{-i(m_2 - \frac{i}{2}\Gamma_2)t}\right) \tag{2.19}$$

This form is useful for studying the B^0–$\overline{B}^0$ meson system.

2.2.2 General formalism for *CP* violation

In the formalism so far we have made no assumption of *CP* conservation. The phenomenon of flavour mixing occurs both when *CP* symmetry is conserved and when it is violated. Let us now look at the possibility of *CP* violation. The *CP* transformation interchanges P^0 and $\overline{P}^0$. Noting $(CP)^2 = 1$ the *CP* transformations are

$$CP|P^0\rangle = e^{i\xi}|\overline{P}^0\rangle, \qquad CP|\overline{P}^0\rangle = e^{-i\xi}|P^0\rangle. \tag{2.20}$$

This makes explicit the freedom of choice in the phase used to define these transformations[3]. Recall the probability amplitudes for the transitions $\overline{P}^0 \to P^0$ and $P^0 \to \overline{P}^0$ are:

$$\langle P^0|\widehat{T}_w|\overline{P}^0\rangle = H_{12} = M_{12} - \frac{i}{2}\Gamma_{12} \tag{2.21}$$

$$\langle \overline{P}^0|\widehat{T}_w|P^0\rangle = H_{21} = M_{12}^* - \frac{i}{2}\Gamma_{12}^* \tag{2.22}$$

Now if *CP* symmetry is conserved then $H_{12} = e^{-2i\xi}H_{21}$, implying $M_{12} = e^{-2i\xi}M_{12}^*$ and $\Gamma_{12} = e^{-2i\xi}\Gamma_{12}^*$. Combining these two equations together, to remove the ξ dependence, we get the meaningful conditions

$$\mathrm{Im}\,(M_{12}^*\Gamma_{12}) = 0 \qquad CP \text{ conservation} \tag{2.23}$$

$$\mathrm{Im}\,(M_{12}^*\Gamma_{12}) \neq 0 \qquad CP \text{ violation} \tag{2.24}$$

or equivalently $|H_{12}| = |H_{21}|$ if *CP* is conserved.

From equation 2.6 these conditions are equivalent to:

$$\left|\frac{q}{p}\right| = \left|e^{i\xi}\right| = 1 \qquad CP \text{ conservation} \tag{2.25}$$

$$\left|\frac{q}{p}\right| \neq 1 \qquad CP \text{ violation} \tag{2.26}$$

A common phase choice is $\xi = 0$ in which case *CP* conservation implies $H_{12} = H_{21}$, $M_{12}, \Gamma_{12} \in \mathbb{R}$, and therefore $p = \pm q$. If CP symmetry is conserved, then under *CP*:

$$CP|P_1^0\rangle = +|P_1^0\rangle \tag{2.27}$$

$$CP|P_2^0\rangle = -|P_2^0\rangle \tag{2.28}$$

In general the states $|P_1^0\rangle$ and $|P_2^0\rangle$ are not orthogonal. The overlap is given by

$$\langle P_1^0|P_2^0\rangle = \frac{|p|^2 - |q|^2}{|p|^2 + |q|^2} \tag{2.29}$$

This is non zero if the mixing matrix H exhibits *CP* violation. Otherwise, if *CP* symmetry holds then the states coincide with orthogonal *CP* eigenstates.

2.3 The neutral kaon system

2.3.1 The *K* meson system

When the K mesons and the Λ baryon were first discovered strange behaviour was observed. Their production rates implied the strong interaction, but their long lifetimes indicated a weak decay. Pais proposed a solution involving a new multiplicative quantum number which was conserved in strong interactions, but was violated in weak interactions [4]. The new particles would be then be produced strongly in pairs, associated production, but would decay weakly on their own. This was refined and a version with the additive quantum number, strangeness, was formulated by Gell-Mann [5]. Together Gell-Mann and Pais classified the strangeness of all known particles and came to the conclusion that $K^0 \neq \overline{K}^0$. This was surprising at the time because charge conjugation (particle $\rightleftharpoons$ anti-particle) was associated only with electrically charged particles. Thus strangeness made the K^0 and $\overline{K}^0$ two distinct objects, whereas there was only one π^0.

Gell-Mann and Pais [6] predicted that K^0 and $\overline{K}^0$ had to mix because the weak decay allowed common intermediate states. They made the conjecture that the physical eigenstates are superpositions of K^0 and $\overline{K}^0$, referred to as K_1^0 and K_2^0 which they took to coincide with *CP* eigenstates.

$$\begin{aligned} |K_1^0\rangle &= \frac{1}{\sqrt{2}}(|K^0\rangle + |\overline{K}^0\rangle) \qquad CP = +1, \\ |K_2^0\rangle &= \frac{1}{\sqrt{2}}(|K^0\rangle - |\overline{K}^0\rangle) \qquad CP = -1. \end{aligned}$$

Consider the decays of the neutral kaons to $\pi^+\pi^-$ and $\pi^+\pi^-\pi^0$ which are *CP* eigenstates with *CP* parity $+1$ and -1 respectively (we have assumed $l = 0$). Therefore only $K_1^0 \to \pi^+\pi^-$ is permitted if *CP* is conserved. The decay $K_2^0 \to \pi^+\pi^-$ is forbidden. However, the decay $K_2^0 \to \pi^+\pi^-\pi^0$ is allowed, but is strongly suppressed due to the limited phase space available. Therefore the lifetime of the K_2^0 should be much longer than K_1^0 . The observed decays to $\pi^+\pi^-$ and $\pi^+\pi^-\pi^0$ do have very different lifetimes. K_1^0 and K_2^0, were commonly called K_S^0 (short) and K_L^0 (long). The predicted long lived K_L^0 meson was discovered by Lederman and his collaborators in 1956 [7]. The lifetimes are [8]:

$$\tau_{K_S^0} = (8.934 \pm 0.008) \times 10^{-11} s, \qquad \tau_{K_L^0} = (5.17 \pm 0.04) \times 10^{-8} s \tag{2.30}$$

2.3.2 *CP* violation in the *K* meson system

The fact that the K_S^0 and K_L^0 lifetimes are so different, $\Gamma_S \gg \Gamma_L$, is extremely useful. If one starts with a beam of neutral K mesons traversing a vacuum they will become, if we wait long enough ($t \gg \frac{\hbar}{\Gamma_s}$), a pure K_L^0 beam. It is possible to test for *CP* violation by searching

for the forbidden $K_L^0 \to \pi^+\pi^-$ transition. In 1964, it was established that a small amount (2×10^{-3}) of *CP* violation occurred in K_L^0 decays [9]. Therefore the *CP* eigenstates and the mass eigenstates are no longer equivalent, and a small amount of *CP* violation via mixing, $|q/p| \neq 1$, must be taken into account. This is parameterised by $\epsilon \in \mathbb{C}$.

$$\frac{q}{p} = \frac{1-\epsilon}{1+\epsilon} \tag{2.31}$$

The $|K_S^0\rangle$ and $|K_L^0\rangle$ now become

$$|K_S^0\rangle = \frac{|K_1^0\rangle + \epsilon|K_2^0\rangle}{\sqrt{1+|\epsilon|^2}}, \quad |K_L^0\rangle = \frac{|K_2^0\rangle + \epsilon|K_1^0\rangle}{\sqrt{1+|\epsilon|^2}} \tag{2.32}$$

Several experiments have measured this parameter more precisely and its current absolute value is $|\epsilon| = (2.280 \pm 0.013) \times 10^{-3}$ [10], and its phase is $43.49 \pm 0.08°$ [8].

$|K_S^0\rangle$ and $|K_L^0\rangle$ can also be represented in terms of the flavour basis states $|K^0\rangle$ and $|\overline{K}^0\rangle$.

$$|K_S^0\rangle = \frac{1}{\sqrt{2(1+|\epsilon|^2)}}\left\{(1+\epsilon)|K^0\rangle + (1-\epsilon)|\overline{K}^0\rangle\right\} \tag{2.33}$$

$$|K_L^0\rangle = \frac{1}{\sqrt{2(1+|\epsilon|^2)}}\left\{(1+\epsilon)|K^0\rangle - (1-\epsilon)|\overline{K}^0\rangle\right\} \tag{2.34}$$

2.4 Indirect *CP* violation

Now we can use some of the formalism developed earlier and apply it practically. We have shown that $|q/p| \neq 1$ gives clear indication of *CP* violation in the mixing matrix H. We need to be able to use some characteristic decay signature to identify $|P^0\rangle$ and $|\overline{P}^0\rangle$ such as the $\Delta S = \Delta Q$ rule for semi-leptonic decays. These provide perhaps the clearest signs of *CP* violation in the neutral kaon system.

Experimentally, decay distances are measured from which proper lifetimes can be inferred, using $x = (p/m)t$. It is therefore possible to measure the coefficient functions, $|f_\pm(t)|^2$ in equation 2.19, which give the flavour content of the decaying particles.

$$|f_\pm(t)|^2 = \frac{1}{4}\left\{e^{-\Gamma_1 t} + e^{-\Gamma_2 t} \pm 2e^{-\Gamma t}\cos(\Delta m t)\right\} \tag{2.35}$$

where $\Gamma = \frac{1}{2}(\Gamma_1 + \Gamma_2)$.

This means that oscillations will be observable provided that $2\pi/\Delta m$ is not long compared to the decay time $1/\Gamma$. Therefore the condition for observable mixing is

$$|\Delta m| \geq \Gamma \tag{2.36}$$

In the kaon system $\Delta m \approx \Gamma$ making the observation of oscillations possible.

If we have a pure K_L^0 beam then it is possible to measure *CP* violation in H by measuring the asymmetry in the semi-leptonic decays.

$$\delta_\ell \equiv \frac{\Gamma(K_L^0 \to \pi^-\ell^+\nu_\ell) - \Gamma(K_L^0 \to \pi^+\ell^-\bar{\nu}_\ell)}{\Gamma(K_L^0 \to \pi^-\ell^+\nu_\ell) + \Gamma(K_L^0 \to \pi^+\ell^-\bar{\nu}_\ell)} \tag{2.37}$$

$$= \frac{|p|^2 - |q|^2}{|p|^2 + |q|^2} \tag{2.38}$$

$$= \frac{2\mathrm{Re}(\epsilon)}{1 + |\epsilon|^2} \tag{2.39}$$

where ℓ is either an electron or muon. Note δ_e and δ_μ are equal if we assume lepton universality. If *CP* was conserved then K_L^0 would be a *CP* eigenstate which must decay with equal probability to two states which are *CP* conjugates of each other, and δ would be zero. The current experimental values are [8]:

$$\delta_e = (3.33 \pm 0.14) \times 10^{-3} \tag{2.40}$$

$$\delta_\mu = (3.04 \pm 0.25) \times 10^{-3} \tag{2.41}$$

These asymmetries are manifestations of a small amount of *CP* violation occurring in the mixing of the kaon system. It is usually called indirect *CP* violation: $|\overline{K}^0\rangle \to |K^0\rangle$ being favoured over $|K^0\rangle \to |\overline{K}^0\rangle$ transitions.

CP violation first manifested itself through the *existence* of the decay mode, $K_L^0 \to \pi\pi$. The full asymmetries in the two-pion channels have been measured. If we define

$$\eta_{+-} \equiv \frac{\langle\pi^+\pi^-|H_w|K_L^0\rangle}{\langle\pi^+\pi^-|H_w|K_S^0\rangle} \qquad \eta_{00} \equiv \frac{\langle\pi^0\pi^0|H_w|K_L^0\rangle}{\langle\pi^0\pi^0|H_w|K_S^0\rangle} \tag{2.42}$$

CP symmetry requires that $\eta_{+-} = 0$, and that $\eta_{00} = 0$. The present experimental values for the magnitudes and phases are [8]:

$$|\eta_{+-}| = (2.275 \pm 0.019) \times 10^{-3} \qquad \phi_\pm = (43.5 \pm 0.6)^\circ \tag{2.43}$$

$$|\eta_{00}| = (2.285 \pm 0.019) \times 10^{-3} \qquad \phi_{00} = (43.4 \pm 1.0)^\circ \tag{2.44}$$

2.5 Direct *CP* violation

When a neutral kaon decays to two pions they must be in a state of zero angular momentum with a symmetric wavefunction. The isospin decomposition of the two pion final states is given by applying the appropriate Clebsch-Gordan coefficients:

$$\langle\pi^0\pi^0| = \sqrt{\frac{2}{3}}\langle 2| - \sqrt{\frac{1}{3}}\langle 0|, \quad \langle\pi^+\pi^-| = \sqrt{\frac{1}{3}}\langle 2| + \sqrt{\frac{2}{3}}\langle 0|. \tag{2.45}$$

Where we have used $\langle 0|$ and $\langle 2|$ to denote the $I = 0$ and $I = 2$ two pion final states. These may be separated into the two isospin channels

$$\langle 0| = \sqrt{\frac{2}{3}}\langle\pi^+\pi^-| - \sqrt{\frac{1}{3}}\langle\pi^0\pi^0|, \quad \langle 2| = \sqrt{\frac{1}{3}}\langle\pi^+\pi^-| + \sqrt{\frac{2}{3}}\langle\pi^0\pi^0|. \tag{2.46}$$

It is experimentally observed that the two pions produced in the weak decay of the $I = 1/2$ kaon prefer to be in a $I = 0$, rather than a $I = 2$ configuration: this is known as the $|\Delta I| = 1/2$ rule. It is useful to normalise the four relevant decay amplitudes to the largest channel.

$$\epsilon_0 = \frac{\langle 0|\widehat{H}_w|K_L^0\rangle}{\langle 0|\widehat{H}_w|K_S^0\rangle}, \quad \epsilon_2 = \frac{1}{\sqrt{2}}\frac{\langle 2|\widehat{H}_w|K_L^0\rangle}{\langle 0|\widehat{H}_w|K_S^0\rangle}, \quad \omega = \frac{\langle 2|\widehat{H}_w|K_S^0\rangle}{\langle 0|\widehat{H}_w|K_S^0\rangle}. \tag{2.47}$$

Here ϵ_0 and ϵ_2 are only non-zero if *CP* is violated and ω quantifies the violation of the $|\Delta I| = 1/2$ rule. Rather than work with ϵ_2 we will introduce the parameter

$$\epsilon' = \epsilon_2 - \frac{\omega}{\sqrt{2}}\epsilon_0 \tag{2.48}$$

We can now relate these theoretical values to the experimentally measurable parameters η_{+-} and η_{00} as follows

$$\begin{aligned}
\eta_{+-} =& \frac{\sqrt{2}\langle 0|\widehat{H}_w|K_L^0\rangle + \langle 2|\widehat{H}_w|K_L^0\rangle}{\sqrt{2}\langle 0|\widehat{H}_w|K_S^0\rangle + \langle 2|\widehat{H}_w|K_S^0\rangle} = \frac{\epsilon_0 + \epsilon_2}{1 + \omega/\sqrt{2}} = \epsilon_0 + \frac{\epsilon'}{1 + \omega/\sqrt{2}} \\
\eta_{00} =& \frac{\langle 2|\widehat{H}_w|K_L^0\rangle - \langle 0|\widehat{H}_w|K_L^0\rangle/\sqrt{2}}{\langle 2|\widehat{H}_w|K_S^0\rangle - \langle 0|\widehat{H}_w|K_S^0\rangle/\sqrt{2}} = \frac{\epsilon_0 - 2\epsilon_2}{1 - \sqrt{2}\omega} = \epsilon_0 - \frac{2\epsilon'}{1 - \sqrt{2}\omega}
\end{aligned}$$

Watson's theorem [11] tells us that the decay amplitudes can be expressed as

$$\begin{aligned}
\langle 0|\widehat{H}_w|K^0\rangle =& A_0 e^{i\delta_0}, \quad \langle 2|\widehat{H}_w|K^0\rangle = A_2 e^{i\delta_2}, \\
\langle 0|\widehat{H}_w|\overline{K}^0\rangle =& A_0^* e^{i\delta_0}, \quad \langle 2|\widehat{H}_w|\overline{K}^0\rangle = A_2^* e^{i\delta_2}.
\end{aligned} \tag{2.49}$$

where δ_0 and δ_2 are the strong interaction $\pi\pi$ s-wave shifts. This gives

$$\begin{aligned}
\epsilon_0 &= \frac{(1+\epsilon)\langle 0|H_w|K^0\rangle - (1-\epsilon)\langle 0|H_w|\overline{K}^0\rangle}{(1+\epsilon)\langle 0|H_w|K^0\rangle + (1-\epsilon)\langle 0|H_w|\overline{K}^0\rangle} \\
&= \frac{\epsilon(A_0 + A_0^*) + A_0 - A_0^*}{\epsilon(A_0 - A_0^*) + A_0 + A_0^*} \\
&= \frac{\epsilon \mathrm{Re}A_0 + i\mathrm{Im}A_0}{i\epsilon\mathrm{Im}A_0 + \mathrm{Re}A_0} = \frac{\epsilon + i\frac{\mathrm{Im}A_0}{\mathrm{Re}A_0}}{1 + i\epsilon\frac{\mathrm{Im}A_0}{\mathrm{Re}A_0}}, \\
&= \epsilon
\end{aligned}$$

The last line follows from adopting the Wu-Yang phase convention where A_0 is taken to be real. ϵ is the parameter which parameterises indirect *CP* violation in mixing.

$$\begin{aligned}
\epsilon' &= \frac{\langle 2|H_w|K_L^0\rangle\langle 0|T_w|K_S^0\rangle - \langle 2|T_w|K_S^0\rangle\langle 0|H_w|K_L^0\rangle}{\sqrt{2}\langle 0|H_w|K_S^0\rangle^2} \\
&= \frac{\sqrt{2}(1-\epsilon^2)\left[\langle 0|H_w|\overline{K}^0\rangle\langle 2|H_w|K^0\rangle - \langle 0|H_w|K^0\rangle\langle 2|H_w|\overline{K}^0\rangle\right]}{\left[(1+\epsilon)\langle 0|H_w|K^0\rangle + (1-\epsilon)\langle 0|H_w|\overline{K}^0\rangle\right]^2}
\end{aligned} \tag{2.50}$$

$$= \sqrt{2}(1-\epsilon)^2 e^{i(\delta_2-\delta_0)} \left. \frac{[A_2A_0^* - A_2^*A_0]}{[A_0 + A_0^* + \epsilon(A_0 - A_0^*)]^2} \right|_{\epsilon\to 0}$$
$$= \frac{i}{\sqrt{2}} e^{i(\delta_2-\delta_0)} \frac{\mathrm{Im}(A_2A_0^*)}{(\mathrm{Re}A_0)^2} \tag{2.51}$$

Referring to equation 2.50, the numerator changes sign under a *CP* transformation so that ϵ' parameterises direct *CP* violation in the decay of the kaon to two pions. Information on the magnitude of possible direct *CP* violation can be obtained by considering the ratio η_{00}/η_{+-}.

$$\left.\begin{array}{rcl} \eta_{+-} & \simeq & \epsilon + \epsilon' \\ \eta_{00} & \simeq & \epsilon - 2\epsilon' \end{array}\right\} \Rightarrow \left|\frac{\eta_{00}}{\eta_{+-}}\right|^2 \approx 1 - 6\mathrm{Re}\left(\frac{\epsilon'}{\epsilon}\right) \tag{2.52}$$

Where we have used the fact that $|\omega| \approx 1/22$ [8] and it has therefore been neglected. Experimentally ϵ' is measured using

$$\mathrm{Re}\left(\frac{\epsilon'}{\epsilon}\right) \approx \frac{1}{6}\left[1 - \frac{\Gamma(K_L^0 \to \pi^0\pi^0)/\Gamma(K_S^0 \to \pi^0\pi^0)}{\Gamma(K_L^0 \to \pi^+\pi^-)/\Gamma(K_S^0 \to \pi^+\pi^-)}\right] \tag{2.53}$$

This double ratio is very convenient experimentally as many of the systematic errors cancel out. There are recent measurements of ϵ'/ϵ from the KTeV experiment at Fermilab [12] and from the NA48 collaboration at CERN [13]. Both measurements confirm and strengthen the NA31 measurement in 1993 [14].

$$\frac{\epsilon'}{\epsilon} = \left\{\begin{array}{ll} (28.0 \pm 4.1) \times 10^{-4} & \mathrm{KTeV} \\ (14.0 \pm 4.3) \times 10^{-4} & \mathrm{NA48} \\ (23.0 \pm 6.0) \times 10^{-4} & \mathrm{NA31} \end{array}\right. \tag{2.54}$$

A non zero value of ϵ' implies that *CP* violation is present in the weak ($\Delta S = 1$) interaction *i.e.* $\langle\pi\pi|K^0\rangle \neq \langle\pi\pi|\overline{K}^0\rangle$. This is referred to as direct *CP* violation. It is important to note that direct *CP* violation requires two different isospin channels with differing phases.

2.6 *CP* violation in the *B* meson system

2.6.1 Correlated *B* mesons and mixing

The case in which a P^0-$\overline{P}^0$ pair are created is important since the two mesons may have correlated or uncorrelated wavefunctions depending upon how they are produced. Correlated wavefunctions occur in the decay of resonances at the production thresholds: $\phi \to K^0\overline{K}^0$, $\psi(3770) \to D^0\overline{D}^0$, $\Upsilon(4S) \to B_d^0\overline{B}_d^0$, and $\Upsilon(5S) \to B_s^0\overline{B}_s^0$. Uncorrelated wavefunctions occur in the multiparticle final states produced in Z boson decays, $p\bar{p}$ collisions, and from the e^+e^- continuum. When B^0-$\overline{B}^0$ meson pairs are produced at the $\Upsilon(4S)$ they are in a coherent state and with definite C parity, $\eta_c = -1$. As the $\overline{B}^0$ meson evolves in time it oscillates back and forth into a B^0. The same thing occurs for the B^0. However, the anti-symmetry of the

wavefunction is preserved by the linearity of the evolution. Hence, if at some instant t one B meson decays and is found to be a B^0 then at *exactly that instant* the other meson is a $\overline{B}^0$ and from that instant on it evolves as a *tagged* $\overline{B}^0$ meson. This allows time dependent measurements of CP asymmetries to be measured.

The phenomenology of mixing discussed earlier can now be applied to the B meson system. Although there is no measurement of the lifetime difference of the neutral B mesons, it must arise from decay channels common to both B^0 and $\overline{B}^0$, for which the branching ratios are generally $\mathcal{O}(10^{-3})$ or less [8]. Since various channels contribute with differing signs, one expects that their sum does not exceed the individual level [15]. Therefore model independently the two neutral B mesons are expected to have negligible difference in lifetime.

$$\frac{\Delta\Gamma_{B_d}}{\Gamma_{B_d}} = \mathcal{O}(10^{-2}) \tag{2.55}$$

However, the mass difference, Δm_{B_d}, has been measured [8].

$$x_d \equiv \frac{\Delta m_{B_d}}{\Gamma_{B_d}} = 0.723 \pm 0.008 \tag{2.56}$$

Therefore we can make the assumption that $\Delta\Gamma_B \ll \Delta m_B$. This allows us to simplify equation 2.19 describing the time evolution of the physical states.

$$f_+(t) = e^{-(im+\frac{\Gamma}{2})t}\cos\left(\frac{\Delta m_B t}{2}\right) \tag{2.57}$$

$$f_-(t) = ie^{-(im+\frac{\Gamma}{2})t}\sin\left(\frac{\Delta m_B t}{2}\right) \tag{2.58}$$

2.6.2 The three types of *CP* violation in *B* decays

When the time dependence of the evolution of the B^0 is known there are three main ways that CP violation can manifest itself in B meson decays:

1. CP violation in mixing, which occurs when the two neutral mass eigenstates cannot be chosen to be CP-eigenstates (see sections 2.2.2 and 2.3.2).
2. CP violation in decay, which occurs in $B^{\pm}$ and B^0 decays, when the amplitude for a decay and its CP-conjugate process have different magnitudes.
3. CP violation in the interference between decays with and without mixing, which occurs in decays which have final states common to both B^0 and $\overline{B}^0$.

Let us now look at each of these situations in turn for the B meson system. For each of the three types of CP violation we will identify a physically meaningful parameter that is independent of arbitrary phase conventions.

2.6.3 *CP* violation in mixing

As we have covered earlier a parameter in neutral meson mixing which is independent of phase conventions and is therefore physically meaningful is:

$$\left|\frac{q}{p}\right| = \left(\frac{M_{12}^* - i\Gamma_{12}^*/2}{M_{12} - i\Gamma_{12}/2}\right)^{1/2} \neq 1 \Rightarrow CP \text{ violation} \tag{2.59}$$

This occurs when the mass eigenstates *i.e.* the physical B mesons are not CP eigenstates. This requires a relative phase between M_{12} and Γ_{12}. We have mentioned earlier how this has been measured in the K meson system. For B mesons it can be measured by looking for an asymmetry in the semi-leptonic decays of mesons initially tagged as B^0 or $\overline{B}^0$.

$$a_{SL} = \frac{\Gamma(\overline{B}^0(t) \to l^+\nu X) - \Gamma(B^0(t) \to l^-\nu X)}{\Gamma(\overline{B}^0(t) \to l^+\nu X) + \Gamma(B^0(t) \to l^-\nu X)} \tag{2.60}$$

$$= \frac{\left|\frac{p}{q}\right|^2 - \left|\frac{q}{p}\right|^2}{\left|\frac{p}{q}\right|^2 + \left|\frac{q}{p}\right|^2} \tag{2.61}$$

which follows from

$$\langle \ell^-\nu X|H|B^0(t)\rangle = (q/p)f_-(t)A^* \qquad \langle \ell^+\nu X|H|\bar{B}^0(t)\rangle = (p/q)f_-(t)A \tag{2.62}$$

The asymmetry is however expected to be small $\mathcal{O}(10^{-2})$ [16].

2.6.4 *CP* violation in decay

If A_f and $\bar{A}_{\bar{f}}$ are the decay amplitudes for $B \to f$ and $\overline{B} \to \bar{f}$ respectively. Then the parameter

$$\left|\frac{\bar{A}_{\bar{f}}}{A_f}\right| \neq 1 \Rightarrow CP \text{ violation} \tag{2.63}$$

is independent of phase convention and gives evidence for direct CP violation in decay.

This type of CP violation is the result of interference between different terms in the decay amplitude. There are two types of phases which may appear in A_f and $\bar{A}_{\bar{f}}$. Complex parameters from the Lagrangian which contribute to the amplitude will appear in complex conjugate form in the CP conjugate amplitude. This means that these phases in A_f and $\bar{A}_{\bar{f}}$ will appear with opposite signs. In the Standard model these phases come only from the weak sector in the CKM matrix. The weak phase of any single term is phase convention dependent. However, the difference of the weak phases in two different terms in A_f is convention independent. A second type of phase can occur in scattering or decay amplitudes

even when the Lagrangian is purely real. These phases appear in the amplitude with equal sign and therefore do not violate *CP*. Their origin is the possible contributions from intermediate on-shell states in the decay due to the strong interaction, and are often called "strong phase shifts." Again only the relative phase difference between two strong phase shifts has physical meaning.

Therefore the contributions to the amplitude A can be split into three parts: its magnitude A_i, a weak phase term $e^{i\phi_i}$, and a strong phase term $e^{i\delta_i}$. This type of decomposition was seen earlier in equations 2.49 where the weak phase was left implicit. If there are many processes contributing to the decay $B \to f$ then the amplitude A_f is given by

$$A_f = \sum_i A_i e^{i(\delta_i+\phi_i)} \tag{2.64}$$

and the condition for *CP* violation in decay is

$$\left|\frac{\bar{A}_{\bar{f}}}{A_f}\right| = \left|\frac{\sum_i A_i e^{i(\delta_i-\phi_i)}}{\sum_i A_i e^{i(\delta_i+\phi_i)}}\right| \neq 1 \Rightarrow CP \text{ violation} \tag{2.65}$$

This is also called direct *CP* violation. It is manifest that there must be at least two different strong and weak phases present for the same transition $B \to f$. This is the situation for example with the two different isospin channels in the kaon decays discussed earlier. Generally for a case where two such phases exist, the rates may be written as

$$|A_f|^2 = |A_1 e^{i(\delta_1+\phi_1)} + A_2 e^{i(\delta_2+\phi_2)}|^2 \tag{2.66}$$

$$|\bar{A}_{\bar{f}}|^2 = |A_1 e^{i(\delta_1-\phi_1)} + A_2 e^{i(\delta_2-\phi_2)}|^2 \tag{2.67}$$

And the asymmetry is given by

$$a_f = \frac{|A_f|^2 - |\bar{A}_{\bar{f}}|^2}{|A_f|^2 + |\bar{A}_{\bar{f}}|^2} \tag{2.68}$$

$$= \frac{-2A_1A_2\sin(\phi_1-\phi_2)\sin(\delta_1-\delta_2)}{A_1^2+A_2^2+2A_1A_2\cos(\phi_1-\phi_2)\cos(\delta_1-\delta_2)} \tag{2.69}$$

It may noted that the earlier expression for ϵ' in equation 2.51 is of this form. In particular ϵ' will vanish if the relative phase of the two isospin amplitudes is zero.

Note that any *CP* asymmetries in charged B decays must be due to direct *CP* violation because mixing cannot occur.

$$a_f = \frac{\Gamma(B^+ \to f) - \Gamma(B^- \to \bar{f})}{\Gamma(B^+ \to f) + \Gamma(B^- \to \bar{f})} \tag{2.70}$$

For example a non-zero asymmetry may come from the interference between the spectator and penguin diagrams present in $B^+ \to K\pi$ decays.

2.6.5 *CP* violation in the interference between decays with and without mixing

Now we consider decays of neutral B mesons to final CP eigenstates denoted f_{CP}. These final states are accessible to both B^0 and $\overline{B}^0$ decays. An experimentally measurable quantity which is independent of phase convention is

$$\lambda \equiv \frac{q}{p}\frac{\bar{A}_{f_{CP}}}{A_{f_{CP}}} = \eta_{f_{CP}}\frac{q}{p}\frac{\bar{A}_{\bar{f}_{CP}}}{A_{f_{CP}}} \tag{2.71}$$

where $\eta_{f_{CP}} = \pm 1$ is the CP eigenvalue of the state f_{CP}.

CP is conserved if $|q/p| = 1$ (see equation 2.59), $|\bar{A}_{\bar{f}_{CP}}/A_{f_{CP}}| = 1$ (see equation 2.63), *and* if there is no relative phase between p/q and $\bar{A}_{\bar{f}_{CP}}/A_{f_{CP}}$. That is λ must have no phase. Therefore

$$\lambda \neq \pm 1 \Rightarrow CP \text{ violation} \tag{2.72}$$

This means it is possible that even if $|q/p| = 1$, and $|\bar{A}_{\bar{f}_{CP}}/A_{f_{CP}}| = 1$ there is CP violation. This is the third classification of CP violation which we will discuss.

$$|\lambda| = 1,\ \mathrm{Im}\lambda \neq 0 \tag{2.73}$$

It is called CP violation in the interference between decays with and without mixing.

Consider the decay amplitudes of neutral B mesons of known initial flavour as they evolve with time.

$$\langle f_{CP}|H_w|B^0(t)\rangle = A_{f_{CP}}(f_+(t) + \lambda f_-(t)) \tag{2.74}$$

$$\langle f_{CP}|H_w|\overline{B}^0(t)\rangle = A_{f_{CP}}\frac{p}{q}(f_-(t) + \lambda f_+(t)) \tag{2.75}$$

These give the decay widths

$$\begin{aligned}
\Gamma\left(B^0(t) \to f_{CP}\right) &\propto \left|\langle f_{CP}|H_w|B^0(t)\rangle\right|^2 \\
&= |A_{f_{CP}}|^2\left\{e^{-\Gamma t}\cos^2\left(\frac{\Delta m_B t}{2}\right) + e^{-\Gamma t}|\lambda|^2\sin^2\left(\frac{\Delta m_B t}{2}\right)\right. \\
&+ \left. ie^{-\Gamma t}\lambda\cos\left(\frac{\Delta m_B t}{2}\right)\sin\left(\frac{\Delta m_B t}{2}\right) - ie^{-\Gamma t}\lambda^*\cos\left(\frac{\Delta m_B t}{2}\right)\sin\left(\frac{\Delta m_B t}{2}\right)\right\} \\
&= |A_{f_{CP}}|^2 e^{-\Gamma t}\left[\frac{1+|\lambda|^2}{2} + \frac{1-|\lambda|^2}{2}\cos(\Delta m_B t) - \mathrm{Im}(\lambda)\sin(\Delta m_B t)\right]
\end{aligned}$$

Similarly

$$\Gamma\left(\overline{B}^0(t) \to f_{CP}\right) \propto |A_{f_{CP}}|^2 e^{-\Gamma t}\left[\frac{1+|\lambda|^2}{2} - \frac{1-|\lambda|^2}{2}\cos\left(\Delta m_B t\right) + \mathrm{Im}(\lambda)\sin\left(\Delta m_B t\right)\right]$$

Experimentally it is useful to take advantage of cancellations and measure the ratio of the difference and sum of the two decay widths. This gives the asymmetry

$$\begin{aligned} a_{f_{CP}}(t) &= \frac{\Gamma(B^0(t) \to f_{CP}) - \Gamma(\overline{B}^0(t) \to f_{CP})}{\Gamma(B^0(t) \to f_{CP}) + \Gamma(\overline{B}^0(t) \to f_{CP})} \\ &= \frac{(1 - |\lambda|^2)\cos(\Delta M t) - 2\mathrm{Im}(\lambda)\sin(\Delta M t)}{1 + |\lambda|^2} \end{aligned} \tag{2.76}$$

This is non-zero if any of the three types of *CP* violation are present. However in the absence of direct *CP* violation and *CP* violation in mixing, $|\lambda| = 1$, this equation becomes

$$a_{f_{CP}}(t) = -\mathrm{Im}(\lambda)\sin(\Delta M_B t) \tag{2.77}$$

2.7 *CP* violation in the Standard Model

The mechanism of producing *CP* violation in the Standard Model was introduced in 1973 [17]. In the Standard Model fermions appear in three families. The interactions that the fermions undergo can be categorised into two types: gauge interactions where two fermions couple to a gauge boson, and Yukawa interactions, where two fermions couple to a scalar. In the Standard Model there are twelve gauge bosons, related to the gauge symmetry

$$G_{SM} = SU(3)_C \times SU(2)_L \times U(1)_Y \tag{2.78}$$

and a single Higgs scalar, related to the spontaneous symmetry breaking

$$G_{SM} \to SU(3)_C \times U(1)_{EM} \tag{2.79}$$

In the Standard Model the interactions of the $SU(2)_L$ gauge bosons W^a_μ with the quarks in the interaction basis are described by:

$$-\mathcal{L}_W = \frac{g}{2}\overline{Q^I_{L_i}}\gamma^\mu \tau^a Q^I_{L_i} W^a_\mu \tag{2.80}$$

The index I means interaction eigenstates. L means they are lefthanded doublets and the index $i = 1, 2, 3\ldots$ is the generation index. Note the coupling strength g of the $SU(2)_L$ gauge bosons W^a_μ does not depend on the generation index. The combination of the 4×4 Dirac matrix γ^μ with the two spin 1/2 quark fields gives a four vector. When this is contracted with the vector, spin 1 gauge boson, field it gives a Lorentz scalar. The τ^a are 2×2 matrices operating in $SU(2)_L$ space which combine the two quark doublets and W^a triplet into an $SU(2)$ singlet.

The Yukawa interactions have a complicated form involving 3×3 complex matrices and couplings between fermions from different generations. To give mass to the quarks and transform to the mass basis, we have to invoke spontaneous symmetry breaking. In the Standard Model this comes from symmetry breaking due to the vacuum expectation value of the neutral component of the Higgs doublet, $\phi_v = \binom{0}{v/\sqrt{2}}$. The important point is that after

symmetry breaking the mass matrices are not in general diagonal. Therefore they must be diagonalised by biunitary transformations. We can find unitary matrices V_{F_L} and V_{F_R} so that

$$V_{F_L} M_f V_{F_R}^{\dagger} = M_f^{\text{diag}} \tag{2.81}$$

The charged current interactions in the mass basis become

$$-\mathcal{L}_{W_\pm} = \frac{g}{\sqrt{2}} \overline{u_{L_i}} \gamma^\mu (V_{uL} V_{dL}^{\dagger})_{ij} d_{L_j} W_\mu^+ + \text{h.c.} \tag{2.82}$$

where $W^\pm$ are the observed charged gauge bosons.

$$\begin{aligned} V_{CKM} &\equiv V_{uL} V_{dL}^{\dagger} \\ &= \begin{pmatrix} V_{ud} & V_{us} & V_{ub} \\ V_{cd} & V_{cs} & V_{cb} \\ V_{td} & V_{ts} & V_{tb} \end{pmatrix} \end{aligned} \tag{2.83}$$

V_{CKM} is a 3×3 unitary matrix which is the mixing matrix for quark flavours [17, 18].

The CKM matrix is complex and has three dimensions and therefore has in general eighteen free parameters. Unitarity of the CKM matrix provides nine constraints. The nine remaining free parameters can be written as three Euler angles, which is the number of independent rotations in three dimensions, and six parameters which are pure phases.

The quark fields can be rephased in the following manner.

$$\begin{aligned} \begin{pmatrix} u'_L \\ c'_L \\ t'_L \end{pmatrix} &= \begin{pmatrix} e^{i\phi_u} & 0 & 0 \\ 0 & e^{i\phi_c} & 0 \\ 0 & 0 & e^{i\phi_t} \end{pmatrix} \begin{pmatrix} u_L \\ c_L \\ t_L \end{pmatrix} \\ \begin{pmatrix} d'_L \\ s'_L \\ b'_L \end{pmatrix} &= \begin{pmatrix} e^{i\phi_d} & 0 & 0 \\ 0 & e^{i\phi_s} & 0 \\ 0 & 0 & e^{i\phi_b} \end{pmatrix} \begin{pmatrix} d_L \\ s_L \\ b_L \end{pmatrix} \end{aligned} \tag{2.84}$$

The only result of this transformation is that V_{CKM} becomes

$$V'_{CKM} = \begin{pmatrix} e^{i(\phi_u - \phi_d)} V_{ud} & e^{i(\phi_u - \phi_s)} V_{us} & e^{i(\phi_u - \phi_b)} V_{ub} \\ e^{i(\phi_c - \phi_d)} V_{cd} & e^{i(\phi_c - \phi_s)} V_{cs} & e^{i(\phi_c - \phi_b)} V_{cb} \\ e^{i(\phi_t - \phi_d)} V_{td} & e^{i(\phi_t - \phi_s)} V_{ts} & e^{i(\phi_t - \phi_b)} V_{tb} \end{pmatrix}. \tag{2.85}$$

Since only relative phases are observable the transformations in equations 2.84 enable five of the six phases in the CKM matrix to be removed. However, the last phase cannot be rotated away. This phase, δ, is the source of *CP* violation in the Standard Model [17].

2.8 The CKM matrix

In general there are 36 different possible parameterisations of the CKM matrix involving three Euler angles and one phase. The first parameterisation was put forward was by Kobayashi and Maskawa [17] in 1973. In 1984 Chau and Keung introduced a different parameterisation which was advocated by the Particle Data Group:

$$\begin{aligned} V &= \begin{pmatrix} 1 & 0 & 0 \\ 0 & c_{23} & s_{23} \\ 0 & -s_{23} & c_{23} \end{pmatrix} \begin{pmatrix} c_{13} & 0 & s_{13}e^{-i\delta_{13}} \\ 0 & 1 & 0 \\ -s_{13}e^{i\delta_{13}} & 0 & c_{13} \end{pmatrix} \begin{pmatrix} c_{12} & s_{12} & 0 \\ -s_{12} & c_{12} & 0 \\ 0 & 0 & 1 \end{pmatrix} \\ &= \begin{pmatrix} c_{12}c_{13} & s_{12}c_{13} & s_{13}e^{-i\delta} \\ -s_{12}c_{23} - c_{12}s_{23}s_{13}e^{-i\delta} & c_{12}c_{23} - s_{12}s_{23}s_{13}e^{-i\delta} & s_{23}c_{13} \\ s_{12}c_{23} - c_{12}c_{23}s_{13}e^{-i\delta} & -c_{12}s_{23} - s_{12}c_{23}s_{13}e^{-i\delta} & c_{23}c_{13} \end{pmatrix} \end{aligned} \tag{2.86}$$

where, c_{ij} and s_{ij} are shorthand for $\cos\theta_{ij}$ and $\sin\theta_{ij}$ which are the three Euler rotation angles θ_{12}, θ_{13}, and θ_{23} (θ_{12} is the Cabibbo angle) and δ is the phase that is the source of *CP* violation.

To have *CP* violation coming from the CKM matrix requires a number of conditions. None of the rotation angles, θ_{ij}, must be 0 or 2π and δ must not be 0 or π. This gives eight necessary conditions on the angles and phase for *CP* violation. This is not enough to ensure *CP* violation. If two quarks which are either both up-type or both down-type have equal mass then one Euler angle and the phase could be removed from the CKM matrix. Therefore there are 14 necessary conditions to have *CP* violation in the Standard Model. However, these can all be grouped together into a single variable. This was first shown by Jarlskog [19].

$$J = \left|\mathrm{Im}(V_{ij}V_{kl}V_{il}^{*}V_{kj}^{*})\right| \tag{2.87}$$

where i and k label any two different up-type quarks while j and l label any two different down-type quarks. This must be non-zero for *CP* violation to occur. In the Chau and Keung parameterisation J is

$$J = \left|s_{13}s_{12}c_{13}^{2}s_{13}c_{23}s_{23}\sin\delta\right| \tag{2.88}$$

In 1983 the bottom quark was found to decay predominantly to the charm quark, $|V_{cb}| \gg |V_{ub}|$. Wolfenstein noticed that $|V_{cb}| \approx |V_{us}|^2$ and introduced a popular parameterisation of V where unitarity only holds approximately [20]. $\lambda = \sin\theta_{12} \approx 0.22$ serves as an expansion operator. We get

$$V = \begin{pmatrix} 1-\lambda^2/2 & \lambda & A\lambda^3(\rho - i\eta) \\ -\lambda & 1-\lambda^2/2 & A\lambda^2 \\ A\lambda^3(1-\rho-i\eta) & -A\lambda^2 & 1 \end{pmatrix} + \mathcal{O}(\lambda^4). \tag{2.89}$$

2.9 Current experimental status of testing the Standard Model

The quark mixing parameters can only be determined directly from processes involving the weak interaction and could be affected by new physics. There are three ways in which to determine the CKM parameters:

1. Direct measurements: Standard Model tree level processes
2. Unitarity: relations between the CKM elements from $V_{CKM}^{\dagger}V_{CKM} = 1$
3. Indirect measurements: Standard Model loop processes.

Seven of the nine CKM elements can be measured by Standard Model tree level processes, $|V_{td}|$ and $|V_{ts}|$ have not yet been directly measured. All of the experimental data in this section comes from [8].

Three different methods can be used to measure $|V_{ud}|$. The most accurate value comes from nuclear beta decays. The current value is:

$$|V_{ud}| = 0.9740 \pm 0.0010 \tag{2.90}$$

The measurement of $|V_{us}|$ comes from semi-leptonic kaon and hyperon decays which give:

$$|V_{us}| = 0.2196 \pm 0.0023 \tag{2.91}$$

The determinations of $|V_{cd}|$ and $|V_{cs}|$ are not very accurate and have large theoretical uncertainties. $|V_{cd}|$ is measured from the deep inelastic neutrino excitation of charm.

$$|V_{cd}| = 0.224 \pm 0.016 \tag{2.92}$$

$|V_{cs}|$ is obtained from the semi-leptonic decays of charm mesons.

$$|V_{cs}| = 1.04 \pm 0.16 \tag{2.93}$$

From inclusive and exclusive semi-leptonic B meson decays to charm $|V_{cb}|$ can be obtained.

$$|V_{cb}| = 0.0395 \pm 0.0017 \tag{2.94}$$

Observing the endpoint of the lepton-energy spectrum in semi-leptonic B decays gives:

$$\frac{|V_{ub}|}{|V_{cb}|} = 0.08 \pm 0.02 \tag{2.95}$$

Lastly, the decay $t \to b\ell^{+}\nu_{\ell}$ gives:

$$\frac{|V_{tb}|^2}{(|V_{td}|^2 + |V_{ts}|^2 + |V_{tb}|^2)} = 0.99 \pm 0.29 \tag{2.96}$$

The current experimental status of the CKM matrix from direct measurements and unitarity considerations, as discussed next, is summarised as

$$|V| = \begin{pmatrix} 0.9745 - 0.9760 & 0.217 - 0.224 & 0.0018 - 0.0045 \\ 0.217 - 0.224 & 0.9737 - 0.9753 & 0.036 - 0.042 \\ 0.004 - 0.013 & 0.035 - 0.042 & 0.9991 - 0.9994 \end{pmatrix} \tag{2.97}$$

To get further information on the matrix elements we use unitarity. There are six independent orthogonality relations

$$\begin{array}{llll} 1) & V_{cd}V_{ud}^* & +V_{cs}V_{us}^* & +V_{cb}V_{ub}^* = 0 \\ 2) & V_{cd}V_{td}^* & +V_{cs}V_{ts}^* & +V_{cb}V_{tb}^* = 0 \\ 3) & V_{ud}V_{td}^* & +V_{us}V_{ts}^* & +V_{ub}V_{tb}^* = 0 \\ 4) & V_{us}^*V_{ud} & +V_{cs}^*V_{cd} & +V_{ts}^*V_{td} = 0 \\ 5) & V_{ub}^*V_{us} & +V_{cb}^*V_{cs} & +V_{tb}^*V_{ts} = 0 \\ 6) & V_{ub}^*V_{ud} & +V_{cb}^*V_{cd} & +V_{tb}^*V_{td} = 0 \end{array}$$

Each of these relations requires the sum of three complex numbers to vanish and can be geometrically represented as triangles in an Argand diagram. All six triangles have the same area given by $J/2$ which quantifies the *CP* violation in the Standard Model. By examining the values in 2.97 it is clear that 1,2,4, and 5 all describe very flat triangles the areas of which are hard to measure. Using equations 3 and 6 more information on *CP* violation can be extracted. The equation which is normally employed to study unitarity in the B_d^0 system is

$$V_{ub}^*V_{ud} + V_{cb}^*V_{cd} + V_{tb}^*V_{td} = 0. \tag{2.98}$$

The corresponding triangle is shown in figure 2-1 where in figure 2-1(b) we divide through

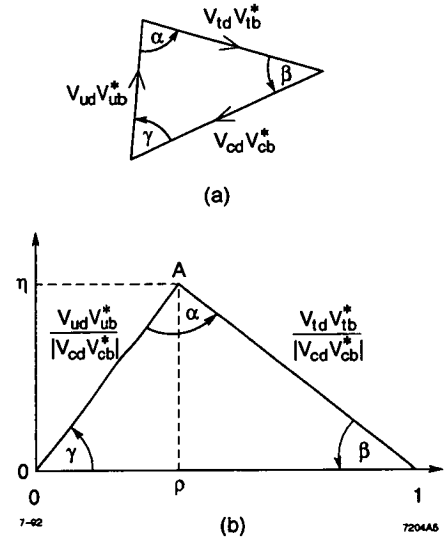

Figure 2-1. *The unitarity triangle before and after rescaling*

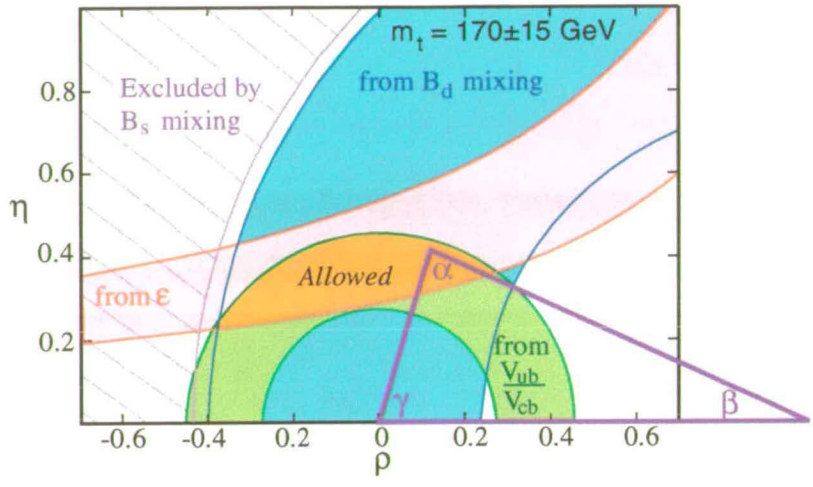

Figure 2-2. *The current experimental bounds on the unitarity triangle*

by $|V_{cd}V_{cb}^*|$ and choose a phase convention where $V_{cd}V_{cb}^*$ is real. This leaves the two vertices of the rescaled triangle fixed at $(0,0)$ and $(1,0)$. Elegantly the coordinates of the remaining vertex are the Wolfenstein parameters (ρ,η).

The three angles of the unitarity triangle α, β, and γ are given by

$$\alpha = \arg\left(-\frac{V_{td}V_{tb}^*}{V_{ud}V_{ub}^*}\right), \quad \beta = \arg\left(-\frac{V_{cd}V_{cb}^*}{V_{td}V_{tb}^*}\right), \quad \gamma = \arg\left(-\frac{V_{ud}V_{ub}^*}{V_{cd}V_{cb}^*}\right).$$

Another unitarity condition is $|V_{ub}|^2 + |V_{cb}|^2 + |V_{tb}|^2 = 1$. Using this and the fact that the measured values of $|V_{ub}|$ and $|V_{cb}|$ are very small implies that, to a good approximation.

$$|V_{tb}| = 1 \tag{2.99}$$

The unitarity relation number (6), together with $|V_{ub}/V_{cb}| \leq 0.10$ and $|V_{cd}/V_{ud}| = 0.22$, gives [15]:

$$|V_{td}V_{tb}^*| \approx 0.0085 \pm 0.0045 \tag{2.100}$$

There are four parameters: λ, A, ρ, and η in the Wolfenstein parameterisation. $\lambda = |V_{us}| = 0.2196 \pm 0.0023$ and $A = |V_{cb}|/|V_{us}|^2 = 0.819 \pm 0.035$ are well determined but ρ and η are not well determined. Therefore it is useful to plot the experimental constraints on these parameters in the $\rho - \eta$ plane. These constraints are shown in figure 2-2.

The value of $|V_{ub}|/|V_{cb}|$, equation 2.95, implies that

$$0.27 < \sqrt{\rho^2 + \eta^2} < 0.45 \tag{2.101}$$

The measured value of $\Delta m_B \propto |V_{td}|^2$ gives the constraint.

$$0.79 < \sqrt{(1-\rho)^2 + \eta^2} < 1.18 \tag{2.102}$$

The constraint on ρ and η from the measured value of ϵ can be written as

$$0.36 < \eta(1.29 - \rho) < 0.53 \tag{2.103}$$

This constraint is represented by the area between two rectangular hyperbolae in the $\rho - \eta$ plane with the focus at $(1.29, 0)$. For more information on this please see [21].

2.10 Measurements of the angles in the unitarity triangle

We will discuss some of the channels which may be used to measure the angles of the unitarity triangle. For more comprehensive information see the recently published *BABAR* physics book [22]. There are many different ways of measuring the angles of the unitarity triangle and we will include an example for each angle here.

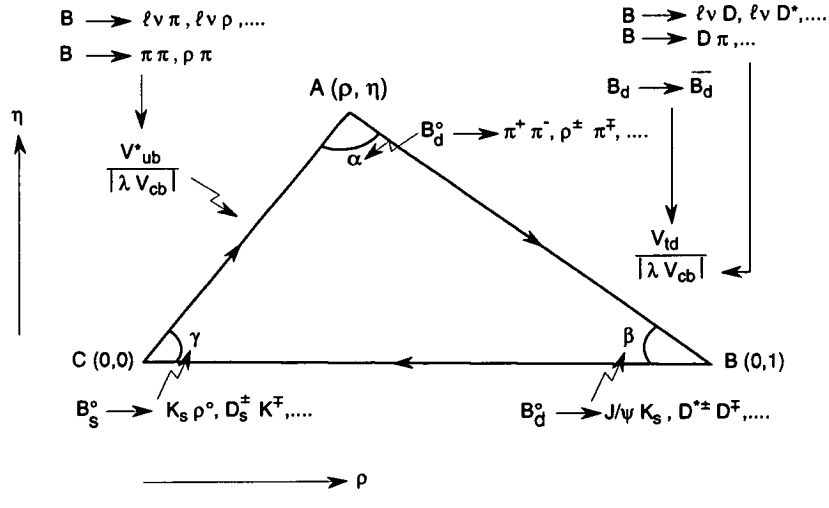

Figure 2-3. *The unitarity triangle and the relevant decay channels*

The main channel for *BABAR* to measure the angle β is:

$$B_d^0 \to J/\psi K_S^0 \tag{2.104}$$

This decay is colour suppressed and the tree level contributions are expected to dominate. In this channel K^0 mixing must also be taken into account:

$$\lambda = \eta_{fCP} \left(\frac{q}{p}\right) \left(\frac{\bar{A}}{A}\right) \left(\frac{q}{p}\right)_K \tag{2.105}$$

$$\lambda_{B_d \to J/\psi K_S^0} = -\left(\frac{V_{tb}^* V_{td}}{V_{tb} V_{td}^*}\right)\left(\frac{V_{cs}^* V_{cb}}{V_{cs} V_{cb}^*}\right)\left(\frac{V_{cd}^* V_{cs}}{V_{cd} V_{cs}^*}\right) \tag{2.106}$$

which gives in this case

$$\mathrm{Im}(\lambda) = \sin(2\beta). \tag{2.107}$$

To measure the angle α the decay $B_d^0 \to \pi^+\pi^-$ can be used. Here we will consider only tree level diagrams for the decay. However, there are contributions to this channel from loop level penguin diagrams.

$$\begin{aligned} \lambda_{B_d^0 \to \pi^+\pi^-} &= \frac{V_{td} V_{tb}^*}{V_{td}^* V_{tb}} \frac{V_{ub} V_{ud}^*}{V_{ub}^* V_{ud}} \\ \Rightarrow \mathrm{Im}(\lambda) &= \sin(2(\pi - \beta - \gamma)) \\ &= \sin(2\alpha). \end{aligned} \tag{2.108}$$

For completeness to measure the angle γ, $B_s^0 \to \rho K_S^0$ decays can be used. Again K^0 mixing must be taken into account.

$$\begin{aligned} \lambda_{B_s^0 \to \rho K_S^0} &= \frac{V_{ts} V_{tb}^*}{V_{ts}^* V_{tb}} \frac{V_{ub} V_{ud}^*}{V_{ub}^* V_{ud}} \frac{V_{cs}^* V_{cd}}{V_{cs} V_{cd}^*} \\ &= \frac{V_{cb}^* V_{ud}^* V_{ub} V_{cd}}{V_{ud} V_{cb}^* V_{cd} V_{ub}^*} \\ &\Rightarrow \mathrm{Im}(\lambda) = -\sin(2\gamma) \end{aligned} \tag{2.109}$$

Where we have used $V_{tb} \simeq V_{cs} \simeq 1$, $V_{ts} \simeq V_{cb}$, and assumed $V_{cb} \in \mathbb{R}$.

2.11 *CP* violation beyond the Standard Model

CP violation is not a well tested part of the Standard Model and there are other models which can also accommodate *CP* violation. Features unique to the Standard Model are that *CP* symmetry is broken explicitly and the sole source of this *CP* violation is from the one phase δ appearing in the quark mixing matrix which leads to *CP* asymmetries of order one. Therefore *CP* cannot be said to be an approximate symmetry of the Standard Model weak interaction. If neutrinos have mass this will lead to lepton mixing as in the quark sector, providing a possible new source of *CP* violation. New models which incorporate *CP* violation may have quite different features. First of all *CP* symmetry may be broken softly, that is spontaneously broken. There may also be more than one phase leading to *CP* violation and these phases may all be very small leading to *CP* being held as an approximate symmetry. The *CP* violation in the Standard Model comes from the quark sector. If there is new physics present then *CP* violation may come from elsewhere *e.g.* an extended Higgs sector. Possible signatures of new physics beyond the Standard Model are summarised in table 2.11 where the features of the Standard Model are included for comparison.

Table 2-1. *Properties of CP violation in the Standard Model versus New Physics*

Standard Model	New Physics
Explicitly broken	Spontaneously broken
Single source δ_{KM}	Many sources (> 1 phases)
Quark sector $\frac{g}{\sqrt{2}} V_{ij} \bar{u}_i d_j W^{\pm}$	New lepton, gauge or scalar sectors
CP is not a symmetry	CP approximate symmetry

There are many new sources of *CP* violation possible other than the Standard Model. It is likely that they exist since we are unable to explain the current baryon asymmetry in the Universe using the Standard Model. If you believe in new physics then it is very difficult not to believe in new *CP* violation. In addition the Standard Model predicts large asymmetries in the B meson system and these are *testable*. It has been observed in neutral K meson decays and has been extensively looked at for this system. However it has only been measured in this system. New physics could show in two different scales.

1. $\Lambda_{NP} \gg \Lambda_{EW}$. This scale could be Grand Unified Theory (GUT) scale. If this is true then the B factories will simply produce precision measurements of CKM parameters.
2. $\Lambda_{NP} \sim \Lambda_{EW}$. Then there would be large deviations from standard model and *BABAR* could provide detailed information on new physics.

2.12 Chapter summary

In this chapter we have covered the general formalism for neutral mixing and *CP* violation. We have covered the kaon sector in detail as this is the only sector where *CP* violation has manifested itself to date and it provides much of the motivation for building a B factory to look at *CP* violation in the B meson system. We then categorised the types of *CP* violation into three types with particular emphasis on the B meson system. We then looked at the Standard Model mechanism for providing *CP* violation. We then discussed how the Standard Model can be constrained through testing the CKM matrix. We have shown how this can be done in many ways from direct measurements of the CKM parameters to testing unitarity. Lastly, we have discussed the features of *CP* violation that might characterise new physics.

CP symmetry is a fundamental property of nature and is therefore very interesting to study. If new physics manifests itself in this area it could help understand the evolution of the Universe. It could also help explain the three generations of fermions within the framework of the Standard Model and the relation of this to quark mixing. There are many relevant measurements which can constrain the theory and where new physics may show up.

3

The BaBar Detector and PEP-II

3.1 Introduction

The *BABAR* detector and PEP-II B factory must meet certain requirements to make a measurement of CP violation in the B meson system possible. Firstly, the branching ratios for B decays to CP eigenstates are very small and therefore the PEP-II machine must provide a very high integrated luminosity. In addition to give a sufficient separation between the two B meson decay vertices requires asymmetric collisions producing a Lorentz boost of the $\Upsilon(4S)$. The main detector requirements are precision vertexing, tracking, particle identification, and calorimetry. This chapter will cover the design and performance of the PEP-II B factory and the *BABAR* detector.

3.2 The PEP-II B factory

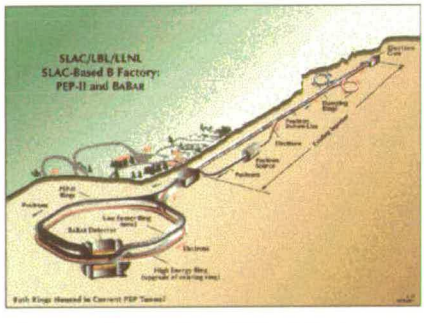

Figure 3-1. *The PEP-II B factory*

Figure 3-2. *Arc section of PEP-II*

The PEP-II B factory [23] is an asymmetric e^+e^- collider which has a design luminosity of $3.0 \times 10^{33}\,\mathrm{cm}^{-2}\mathrm{s}^{-1}$ and a centre-of-mass energy, $\sqrt{s}$ = 10.58 GeV. This corresponds to the $\Upsilon(4S)$ resonance which lies just above the production threshold for B_d mesons and below that for B^* and B_s mesons. The cross-sections for $\Upsilon(4S)$ production and continuum $q\bar{q}$, are 1.1 nb and 2.5 nb respectively. The branching ratio of the $\Upsilon(4S)$ to $B\overline{B}$ meson pairs is close to 100% providing around 3×10^7 B meson pairs each year at design luminosity. The small mass difference between the Υ(4S) resonance and the two B mesons means that in the Υ(4S) rest frame the B mesons are almost at rest and travel only a short distance before decaying making their lifetimes hard to measure. To overcome this an asymmetric machine was built. This uses

Table 3-1. *Primary PEP-II parameters*

Parameter	Units	Low energy ring	High energy ring
Energy	GeV	3.1	9.0
Circumference	m	2199.32	2199.32
Beam Current	A	2.14	0.99
Number of bunches		1658	1658
Particles per bunch		5.91×10^{10}	2.73×10^{10}
Bunch length	cm	1.0	1.0
Bunch separation	ns	4.2	4.2
RF frequency	MHz	476	476
RF voltage	MV	5.9	18.5
Beta function, β_x^*	cm	37.5	50.0
Beta function, β_y^*	cm	1.5	2.0
Tune shift, $\xi_{x,y}$		0.03	0.03
x tune		24.57	36.57
y tune		23.64	34.64
Emittance, ε_x	nm.rad	64.0	48.0
Emittance, ε_y	nm.rad	2.6	1.9
IP spot size, x	μm	155	155
IP spot size, y	μm	6.2	6.2
Synch. rad. loss	MeV/turn	0.77	3.57
Filling time	min	3	3
Injection rate	Hz	60	60

colliding beams of unequal energy to Lorentz boost the $\Upsilon(4S)$ in the direction of the beam axis. The beam energies chosen are 9 GeV electrons on 3.1 GeV positrons($(\beta\gamma = 0.56)$. This results in the B mesons having appreciable velocities and measurable decay lengths ($\sim$250 μm). After the original suggestion [24] for an asymmetric collider design further studies [25, 26, 27] showed that an asymmetry ratio of 3:1 would be optimal. The main PEP-II parameters are given in table 3-1.

3.2.1 The injection system

The SLC linac is the main injector for PEP-II. Low emittance damped electron and positron beams are extracted at their respective beam energies allowing for on-energy injection. The injection takes place in the vertical plane to avoid parasitic beam crossings at the interaction point, produced by synchrotron oscillations of off-momentum particles. Due to losses in the rings it is necessary for injection to occur every 1–2 hours to increase the beam currents. This type of injection is called top-off. The time taken for top-off (80%→100%) is approximately 1 minute, and the complete fill time if the beams are lost is 3 minutes. The injection system is shown in figure 3-3. The linac runs at 120 Hz by using two "60-pps time-slots" equally spaced

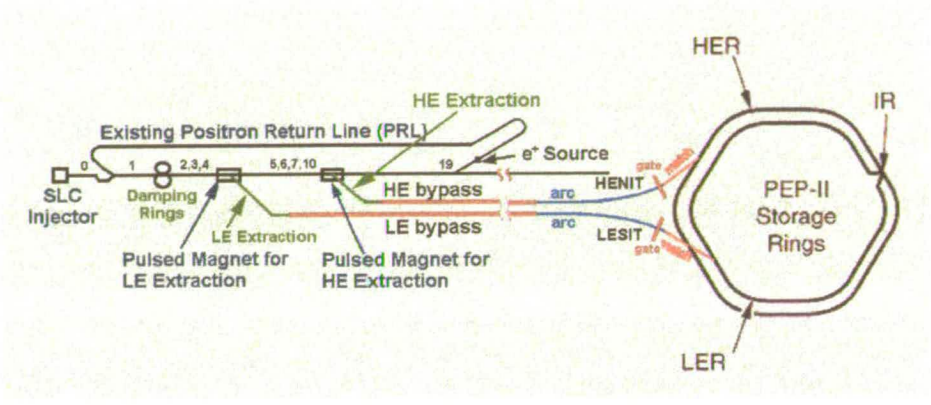

Figure 3-3. *The injection system for PEP-II.*

in time. Each 60-pps time slot is a set of pulses synchronized with the 60 Hz AC power line. In the first time-slot a single positron bunch and an electron bunch, are ejected from south and north damping rings respectively. They are accelerated, the positrons are separated off at 2.5–4 GeV for injection into the low energy ring, and the following "scavenger" electron bunch continues acceleration to high energy (approx. 30 GeV). This collides with a beryllium target creating a new positron bunch, which returns on a dedicated line and is stored in the south damping ring. Meanwhile the electron gun creates an electron bunch and stores it in the north damping ring. On the second time slot this electron bunch is ejected from the damping ring, accelerated, and separated off at 7-12 GeV for injection into the high energy ring. The electron gun provides another electron bunch (scavenger) for the next time slot completing the cycle which repeats until injection is complete. The intensity per pulse is between 10^8 and 4×10^{10} particles. The momentum resolution, 0.7% (FWHM), of the injected particles and the location of injection (large β_y^*) both provide good acceptance of the particles into the circulating beams.

3.2.2 The interaction region

The interaction region of PEP-II is extremely complex. A plan view of the beamline components is shown in figure 3-4. The LER and HER beams are brought together first vertically, then horizontally, collided head-on, and returned over a distance of about 120 m. The Q1/Q2 quadrupoles form the low energy beam focusing doublet, and Q4/Q5 quadrupoles form the high energy beam focusing doublet. The beam separation requires a strong dipole field near the IP which is produced by the B1 magnets. In addition the *BABAR* solenoidal field plays a rôle in this as the beam axis is not aligned with the detector axis.

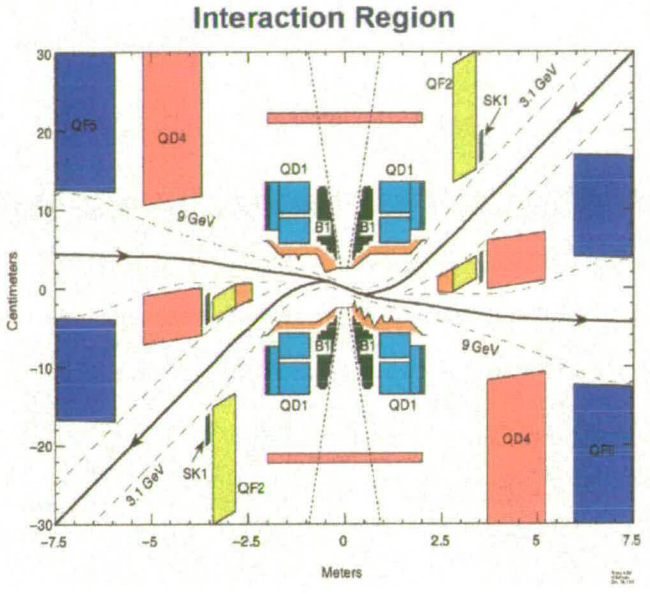

Figure 3-4. *The interaction region of PEP-II.*

3.2.3 Machine backgrounds

The high beam currents at PEP-II are an order of magnitude greater than previous machines and consequently produce large backgrounds. However, to avoid impacting detector performance and physics measurements it is desirable to have backgrounds which are not significantly larger than other machines, *e.g.* CESR [28]. The machine background comes from two main sources: synchrotron radiation and lost particles. The lost particle backgrounds are produced by beam gas interactions. The main impact of the backgrounds on the detector performance is the increase of occupancy in the various sub detectors, particularly the vertex detector, and the radiation damage to which the calorimeter is most sensitive.

The synchrotron radiation background comes in two types: *fan* radiation due to a dipole or offset quadrupole magnet and *quadrupole* radiation due to on axis quadrupole or sextupole. The dominant source of synchrotron radiation at PEP-II is produced by fan radiation near the interaction point from the B1 dipole bending magnets and the Q1 focusing quadrupoles. A copper mask, shown in figure 3-4 helps reduce the occupancy and radiation levels in *BABAR*.

The dominant background at PEP-II is from lost particle background. This is due to the particle falling outside the maximum momentum range of the storage rings and hitting the beam pipe producing electromagnetic showers. This is usually caused by bremsstrahlung interactions with the beam gas molecules and sometimes by coulomb interactions. The lost particles can originate many metres away from the interaction point and collimators are installed upstream from the detector in both directions to help reduce this. The pressure in the straight sections near the interaction region must be as low as possible. The nominal

background levels assume a pressure of 10 nTorr for the high energy ring at 0.5 A and 1 nTorr for the low energy ring at 1.5 A.

3.2.4 Current PEP-II performance (December 1999)

PEP-II first concentrated on the energy scan of the $\Upsilon(4S)$ resonance, increasing the luminosity, and colliding at the peak. The Particle Data Book gives 10580 ± 3.5 MeV for the mass and PEP-II got 10585 ± 4 MeV. Then PEP-II settled into a luminosity integration mode for BaBar. A peak luminosity of $1.4 \times 10^{33}\mathrm{cm}^{-2}\mathrm{s}^{-1}$ was achieved on November 7, 1999. The record luminosity of $1.43 \times 10^{33}\mathrm{cm}^{-2}\mathrm{s}^{-1}$ was achieved on November 10 where 830 bunches were collided, with 908 mA of positrons and 642 mA of electrons. The beam spot sizes were about 6.5 and 200 microns vertically and horizontally. The beam-beam tune shifts are about 0.035 horizontally and 0.02 vertically.

3.3 The BaBar detector

The *BABAR* detector consists of a silicon vertex detector, a drift chamber, a particle identification system, a Caesium Iodide (CsI) electromagnetic calorimeter, and a superconducting solenoidal magnet (1.5 T) with flux return instrumented for muon identification.

To function optimally and to achieve the physics aims the detector requires:

1. Maximum possible acceptance in the centre-of-mass system. This requires an asymmetric detector design.
2. Excellent vertex resolution. The B mesons travel almost parallel to the beam axis. To measure their decay time difference accurately, stresses the z-component of vertex resolution.
3. Accurate particle tracking over the range 60 MeV $< p_t <$ 4 GeV.
4. Particle identification of e, μ, π, K and p over a wide kinematical range. In particular π-K discrimination at high momenta (2-4 GeV).
5. Detection of photons and π^0's over a wide energy range, 20 MeV $< E <$ 4 GeV.

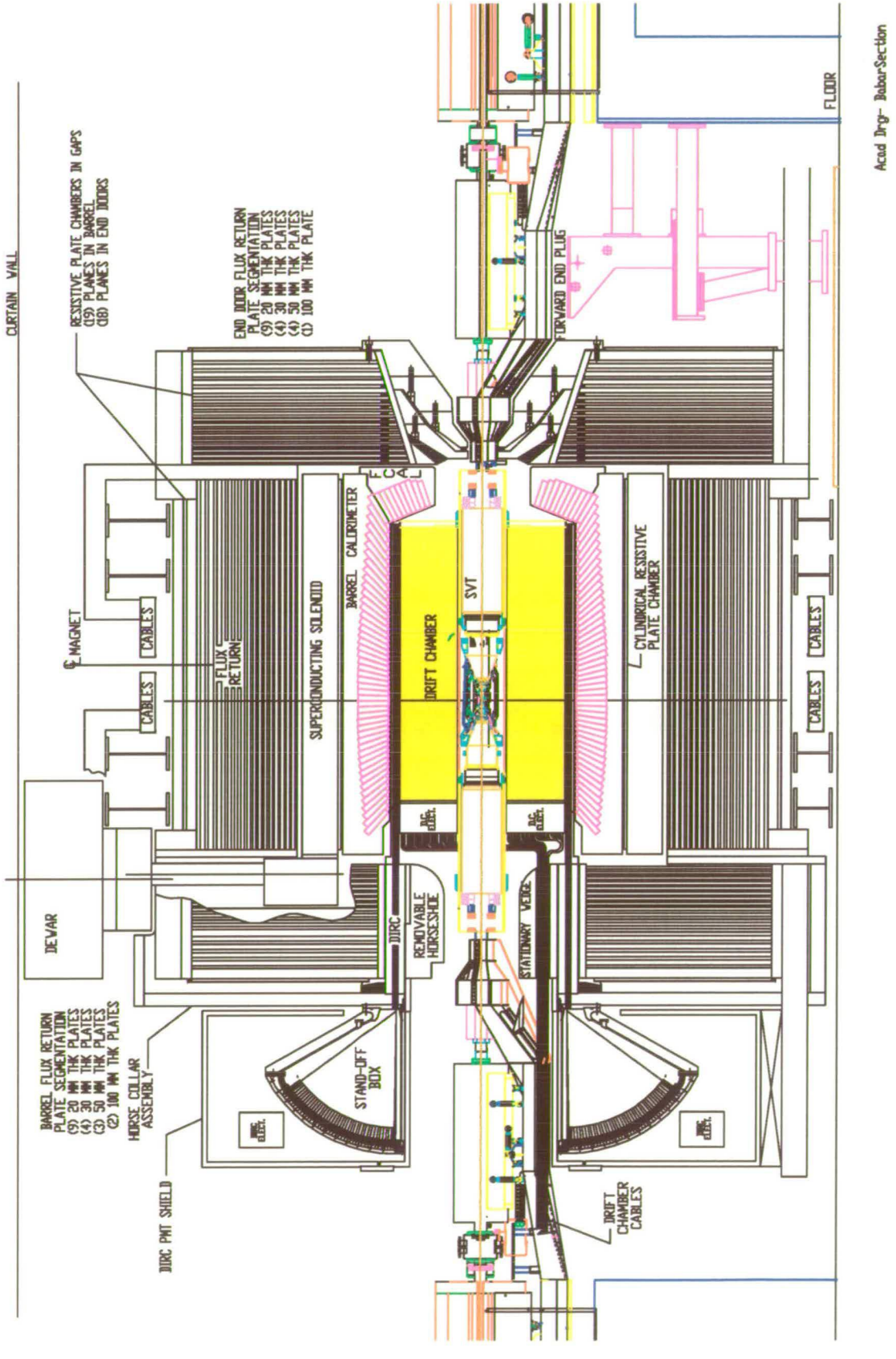

Figure 3-5. *The BABAR detector.*

3.3.1 The silicon vertex tracker

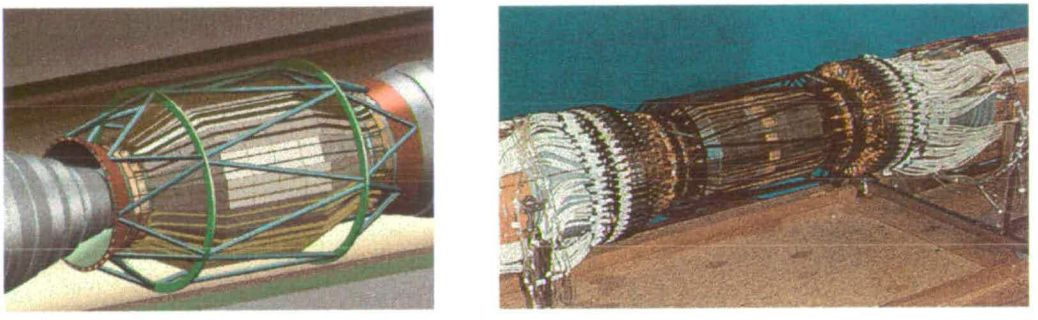

Figure 3-6. *The BABAR silicon vertex tracker*

3.3.1.1 Physics requirements

The measurement of time-dependent CP violation in B^0 decays requires precise measurement of the two B meson decay vertices. From the two different decay lengths the time difference between the two decays can be calculated. This is the main task of the BABAR silicon vertex detector. It is required to provide track impact parameter information and the initial θ and ϕ track angles. In addition, for particles with $p_t < 100\,\mathrm{MeV/c}$, which do not reach the drift chamber, it must provide complete tracking information.

The single vertex resolution required by BABAR to perform precise CP violation measurements, is of order $80\,\mu\mathrm{m}$ [29]. The silicon vertex tracker has a resolution of $\sigma_z \approx 40\,\mu\mathrm{m}$ on the CP-eigenstate B vertex and a resolution of 60–$80\,\mu\mathrm{m}$ on the tagging vertex [30]. The beam pipe is a double-walled, water-cooled, beryllium structure giving 1.06% radiation lengths (X_0) of material. Multiple scattering in the beam pipe, and in the silicon itself, limits the maximum achievable track parameter resolutions for the different layers. The best angular information for a track and its impact parameter resolution is given by the precision of the measurements closest to the interaction point. Therefore the intrinsic point resolution of the inner layers, given in table 3-2, had to be minimised to such a level that multiple scattering becomes the dominant effect [31]. To allow for the best track alignment with the drift chamber, and to accurately track low momentum particles, outer layer measurements are also required.

The detector must cover as much solid angle as possible. The maximum acceptance of the silicon vertex tracker is limited by constraints on the polar angle coverage due to the close proximity of the PEP-II beam optics (lower limit of 17.2° in both directions) and by necessary mechanical supports, electronics and cabling. To maximise the coverage in the forward direction various beam-line components were placed in the backward direction. The silicon vertex tracker covers the polar angle between 20.1° to 150.2°. Lastly, the silicon vertex tracker must present as little material as possible in front of the drift chamber in order not to degrade its performance.

3.3.1.2 The silicon vertex tracker design

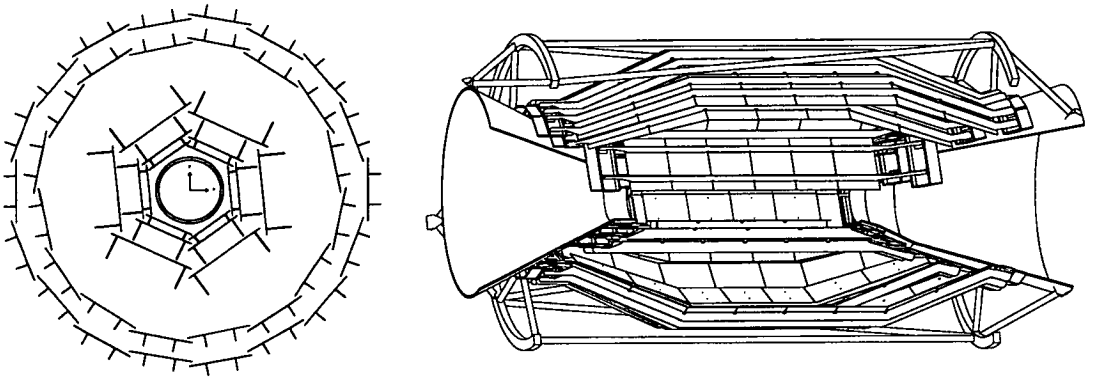

Figure 3-7. *Cross sectional view in $r\phi$ plane and 3d cutaway view of the BABAR silicon vertex tracker*

The silicon vertex tracker (fig: 3-6) consists of five concentric layers of silicon micro-strip detectors. The inner three layers are sub-divided in ϕ into 6 detector modules (fig: 3-7). In addition, they are displaced slightly in ϕ to allow a pin-wheel type arrangement to ensure overlap between the detectors. The outer two layers are sub-divided into 16 and 18 modules. These modules are of two types, "a" and "b", each being situated at different radii to again ensure good overlap between detectors. The properties of each layer are listed in table 3-2. The outer two layers have an arch-type structure whereas the inner layers have a barrel-type structure. The arch-type structure reduces the amount of silicon required for maximum solid angle coverage and reduces large track incidence angles (reduction in multiple scattering). The silicon detectors are double-sided with 90°stereo. The z-coordinate is measured by strips orientated perpendicular to the beam direction, located on the inner-side of the silicon, while the ϕ-coordinate is measured by strips parallel to the beam direction, on the outer side.

Table 3-2. *Description of the layers of the silicon vertex tracker.*

Layer	1	2	3	4a	4b	5a	5b
Radius (mm)	32	40	54	124	127	140	144
Modules/layer	6	6	6	8	8	9	9
Wafers/module	4	4	6	7	7	8	8
Readout Pitch (μm)							
ϕ	50	55	55	82–100		82–100	
z	100	100	100	210		210	
Intrinsic resolution (μm)							
ϕ	10	10	10	10–12		10–12	
z	12	12	12	25		25	

To give support and alignment to the PEP-II beam optics it is necessary to have a "beam support tube" at a radius of 20 cm, consisting of $0.7\%X_0$ of material. The silicon vertex

tracker is positioned within the annular volume between the beam pipe and the beam support tube. The diameter of the beam support tube prevents the drift chamber from coming close to the beam line. Hence the necessity for the silicon vertex tracker to perform low momentum tracking. Access to the silicon vertex tracker requires removal of the beam support tube which requires a long shutdown period. *CP* violation studies require a high total integrated luminosity, therefore every aspect of the silicon vertex tracker was designed to be as reliable as possible.

3.3.1.3 The electronic readout

The silicon covers an area of $0.94m^2$ with 340 silicon detectors, giving a total of about 150K readout channels and 500K wire bonds. The strips are AC coupled with polysilicon bias resistors. The bias voltage applied to the strips is +20V (max 60V). Each readout chip, called the ATOM chip [32, 33, 34] contains 128 parallel analog channels. The signal from each strip undergoes linear amplification and shaping. Next the "time over threshold" (TOT) is measured, where the threshold value used depends on the background conditions. The TOT is related logarithmically to the charge deposited on the strips. This compresses the dynamic range, reducing the number of bits required for storage. The TOT is then digitally recorded, inserted into a 12 μs trigger latency buffer, and readout by the data acquisition if a level 1 accept is received. Twisted pair cables then carry the signals to multiplexer modules on the detector platform. These convert the signals and transmit them, via fibre optic cables, to five SVT readout modules (ROMS).

3.3.2 The drift chamber

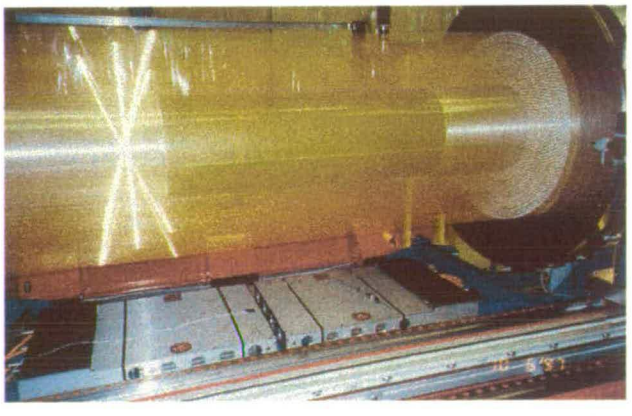

Figure 3-8. *The BABAR drift chamber (during stringing).*

3.3.2.1 Physics requirements

The drift chamber is a key component of the *BABAR* detector. Exclusive reconstruction of the *CP* decays of B mesons requires accurate track information and this must be reconstructed efficiently. The track information must correlate well with the tracks in the silicon vertex tracker and also provide accurate track information to the DIRC and electromagnetic calorimeter. The *BABAR* drift chamber has been designed to produce the momentum and spatial resolutions that are necessary to do this. The design goals are a spatial resolution of 140 μm and a momentum resolution $\sigma_t/p_t = 0.3\%$ ($p_t > 1$ GeV). In the forward part of the detector it is the only PID system and in the barrel it complements the DIRC, using dE/dx information for low momentum tracks (< 700 MeV). The dE/dx resolution (40 measurements) for a track perpendicular to the wire axis is 7%. The drift chamber must provide maximum solid angle coverage. The design acceptance extends down to the PEP-II beam components (17.2°). The drift chamber is one of the main inputs to the level 1 trigger system. Lastly, it must also present the minimum amount of material possible in front of the other sub-systems, in order not to degrade their performance. To meet these requirements a small-cell, low-mass, drift chamber with a helium-based gas was necessary. Reviews of the drift chamber can be found in [35, 36].

3.3.2.2 The drift chamber design

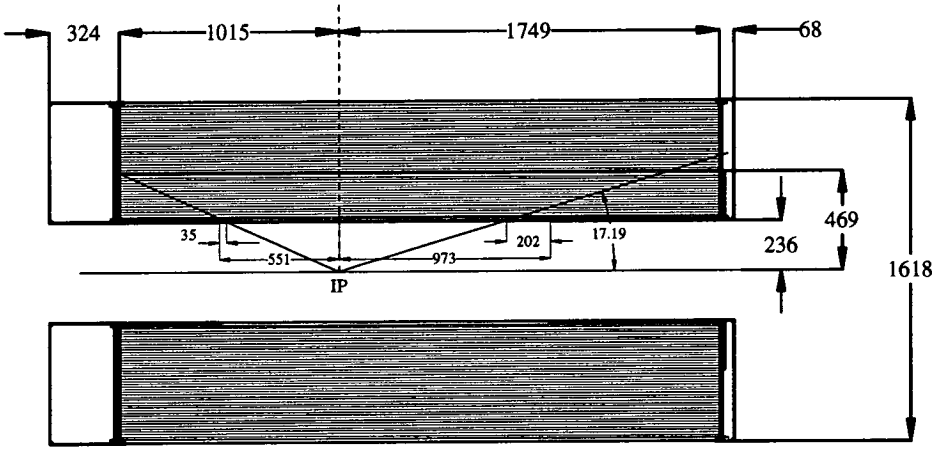

Figure 3-9. *The BABAR drift chamber (z-projection).*

A drawing of the *BABAR* drift chamber (z-projection) is shown in figure 3-9 and a photo of the drift chamber during stringing is shown in figure 3-8. The mechanical design consists of a cylinder 276 cm long. The inner radius is 23.6cm and is constructed from 1mm beryllium ($0.28\%X_0$). The outer radius is 80.9 cm and is made from 2 layers of segmented 2×1.5 mm^2 carbon-fibre skins on a Nomex core ($1.5\%X_0$). To provide RF shielding the skins are covered by a thin aluminium foil.

The flat endplates are made from aluminium. The backward endplate is 24 mm thick, and the preamplifier and digitiser electronics are located here. The forward endplate has a step in thickness: the inner section is 24mm thick, but the outer section is 12mm, the reason being that the outer section is directly in front of the endcap calorimeter, and needs to be as thin as possible.

The wires are strung between the end-plates. The sense wires (1960V) are 20 μm gold-plated tungsten-rhenium and the field shaping wires are 120 μm and 80 μm gold-plated aluminium. The field-shaping wires situated at the superlayer boundaries are at 340V and the other field wires are at ground. The gas mixture is a helium-isobutane (4:1) mix chosen to give the necessary low density, and short drift time. Studies showed this mixture produced the best dE/dx and spatial resolution. Figure 3-12 shows the spatial resolution versus the drift distance. In figure 3-11 the dE/dx versus momentum Bethe-Bloch curves are shown. For tracks at 90° the gas and wires are collectively 0.3% X_0 of material, out of a total of 2.08%X_0 for the complete chamber.

The cell structure in the drift chamber comprises 7104 hexagonal cells which are approximately 1.2 × 1.8cm^2 in dimension. Figure 3-10 shows the 50 ns isochrones for a typical cell, in a 1.5 T magnetic field. The drift cells are arranged into 10 superlayers which each contain 4 layers. Table 3-3 lists the details of each superlayer, and the cell layout is shown in figure 3-10. The stereo superlayers (U,V) vary in angle from 40 mrad to 70 mrad going outwards, relative to the axial layers (A).

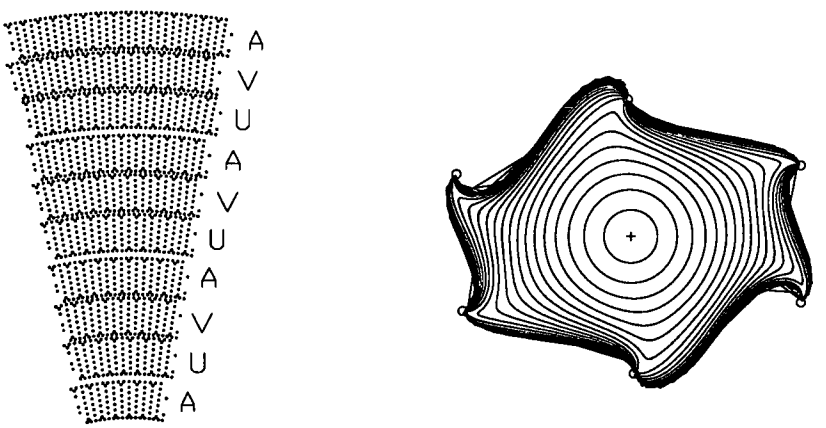

Figure 3-10. *Cross sectional view ($r\phi$ plane) of the BABAR drift chamber cell layout, and a typical drift cell showing 50* ns *isochrones (1.5 T)*

3.3.2.3 The electronic readout

The electronics must perform two tasks. The leading edge of the signal produced by the charge deposit on the sense wire must be measured to provide the drift-time measurement

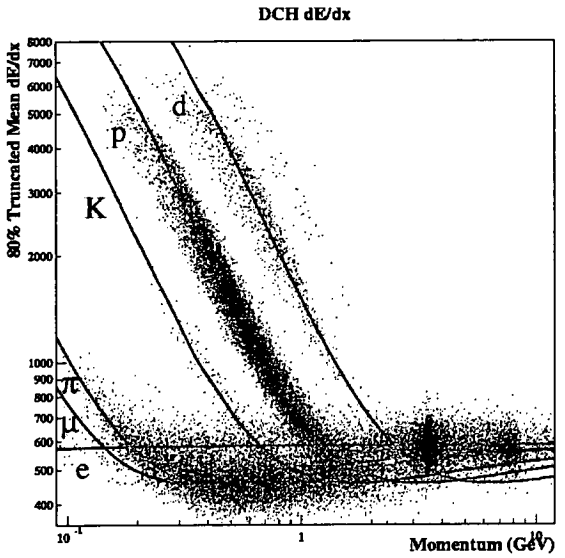

Figure 3-11. *dE/dx vs momentum using Bethe-Bloch parameterisation from the drift chamber. This shows the 3σ K/π separation up to around 700* MeV*. The proton and deuteron particles are mostly from beam gas events. There are also two high momenta patches which are from Bhabha events.*

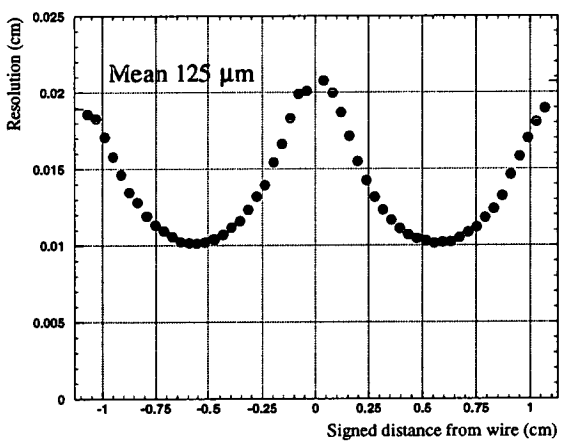

Figure 3-12. *The single hit resolution as a function of distance from wire. The average resolution is 125 μm to be compared to the 140 μm design value.*

for spatial resolution. The other task is that the charge deposited on the signal wire must be summed for the dE/dx measurement. The degradation to the chamber's intrinsic performance due to the electronics must be less than 10%. For full details of the electronic readout and also results from the cosmic ray commissioning, see [37, 38, 39].

Table 3-3. *Description of the drift chamber superlayers.*

Superlayer	Stereo Angle (U,V or A)	Number of cells per layer
1	A	96
2	U	112
3	V	128
4	A	144
5	U	176
6	V	192
7	A	208
8	U	224
9	V	240
10	A	256

The electronics for amplification, digitisation and the trigger interface are located behind the rear endplate. The cell arrangement has a 16-fold azimuthal symmetry. For each 1/16 wedge the electronics are arranged radially segmenting the superlayers (1–4, 5–7 and 8-10). The electronics are housed in wedge-shaped aluminium boxes called Front End Assemblies (FEAs). The edges of the boxes are mounted to radial support bars which also carry the water cooling.

The channels from the signals on the sense wires are split into groups of 4, each going to an Amplifier/Digitiser board. Each ADB contains two 4-channel amplifier chips (DCAC), and one 8-channel ELEFANT (ELEctronics For Amplitude aNd Timing) chip. For each signal there are two outputs from the DCAC chip. One is a shaped analog signal for the dE/dx measurement, and the other is a discriminator pulse for the drift time measurement. The ELEFANT chip digitises the analog pulse using a Flash ADC and the timing of the discriminator pulse using a TDC. The sample clock is 14.875 MHz which provides a 1 ns precision on the discrimination. The digital data are then input to a 12.9 μs latency buffer, and if a level 1 accept is received this is dumped into a multi-event buffer (4 levels) with an attached trigger flag, event counter and hit flag. The hit flag allows sparsification. The data are then readout on 2 bit 30 MHz lines to data I/O modules which convert the data onto 1 Giga-bit fibre links for transportation to the ROMs.

3.3.3 The detection of internally reflected Čerenkov light (DIRC)

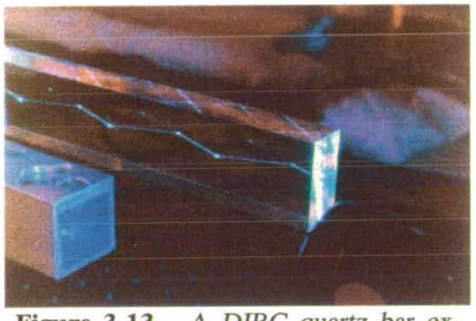

Figure 3-13. *A DIRC quartz bar exhibiting total internal reflection*

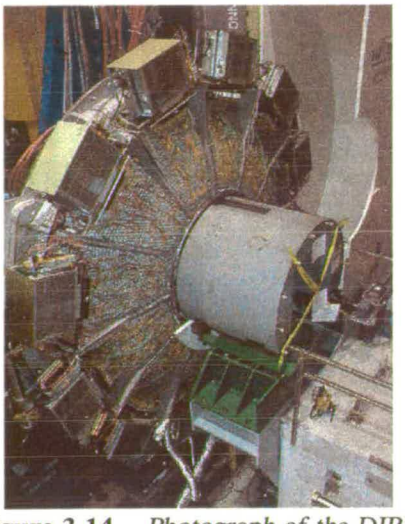

Figure 3-14. *Photograph of the DIRC stand-off box*

3.3.3.1 Physics requirements

Particle identification is very important for CP violation physics. To efficiently tag the B meson flavour, thus identifying it as a B^0 or a $\overline{B}^0$, requires the identification of kaons with p_t up to 2 GeV. In addition, for many rare B decays it is vital to be able to differentiate between decay modes which contain a kaon, and ones which contain a pion. As an example the important decay mode $B^0 \to \pi^+\pi^-$ which allows information on the angle α to be extracted must be distinguished from the mode $B^0 \to K^+\pi^-$. Another interesting example is the decay $B^0 \to \rho\gamma$ which can provide information on $|V_{td}|$. This mode must be distinguished from the more favoured $B^0 \to K^*\gamma$ channel.

The BABAR drift chamber can only provide K/π discrimination up to 700 MeV using dE/dx information, after which the Bethe-Bloch curves merge (see figure 3-11). Due to the Lorentz boost particles from a two body B decay can have a maximum momentum of 4 GeV in the forward direction. Therefore K/π separation is necessary for the region from 0.7 GeV to 4 GeV. The instrumented flux return (IFR) becomes less efficient at muon identification for muons with p_t less than 750 MeV. Therefore the particle identification system must complement the IFR in this region. Lastly, the DIRC can also be used to identify high momenta protons.

At PEP-II the beams collide every 4.2 ns with large backgrounds, giving a fast trigger rate. Therefore the system must be fast and able to remain efficient with high backgrounds. Outside the particle ID system is the electromagnetic calorimeter which is capable of an excellent energy resolution and must be able to detect soft photons coming from π^0 decays. Therefore

the DIRC system must have excellent uniformity in the radiation length it presents, have high dimensional constraints, and be as close as possible to the calorimeter.

3.3.3.2 The DIRC design

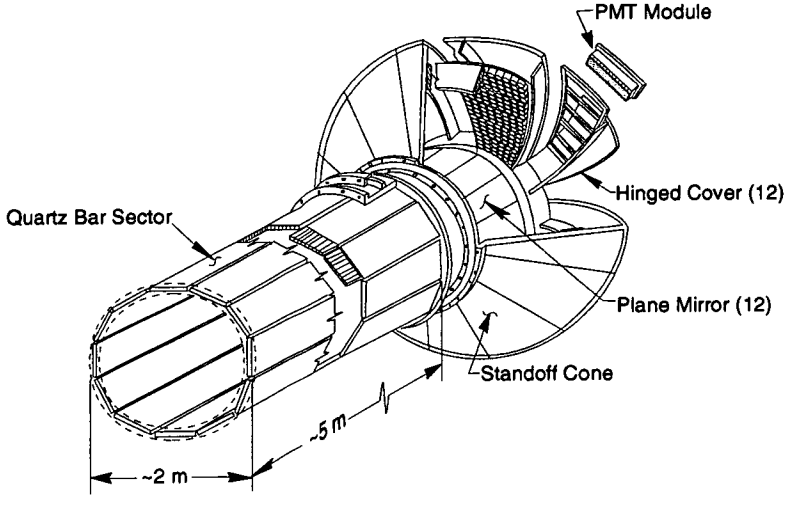

Figure 3-15. *3d schematic of the DIRC*

The DIRC (Detection of Internally Reflected Čerenkov radiation) is different from conventional Čerenkov ring imaging devices because it relies on the photons trapped by total internal reflection. This is normally a background in conventional ring imaging Čerenkov (RICH) detectors. For a radiator the DIRC uses quartz bars which are arranged in a barrel type configuration which is dodecagonal in cross-section (see figure 3-15). Each of the twelve sides, is made up of twelve quartz bars which are fitted 75 μm apart. Each quartz bar is rectangular in cross-section, 17 mm thick, 35 mm wide, and 4.9 m long. The length of the bars is achieved by gluing together four shorter bars of length 1225 mm. The bars were manufactured with extremely stringent tolerances [40, 41]. They must be flat and parallel to within 25 μm, have an excellent edge sharpness with edge radii less than 5 μm, and the polished surfaces must have an optical finish of better than 5 Å (rms). Quartz was chosen for its high refractive index ($n_1 = 1.474$), long radiation length (X_0 = 11.7 cm) , long absorption length, and low chromatic dispersion. The volume surrounding the bars is filled with nitrogen gas having a low refractive index ($n_3 \approx 1$).

As a particle traverses the bar at a velocity $\beta \geqslant \frac{1}{n_1}$, it radiates a Čerenkov cone of light at the angle $\theta_c = \frac{1}{\beta n}$. Due to the high refractive index of the bar some of the Čerenkov photons undergo total internal reflection successively ($\approx$ 100 times) down the bar towards the backward end. Any forward going photons are reflected back by a mirror at the forward end. The angle θ_c is preserved throughout. When the light cone reaches the end of the bar it then expands for 1.17 m in a large expansion medium of high quality purified water

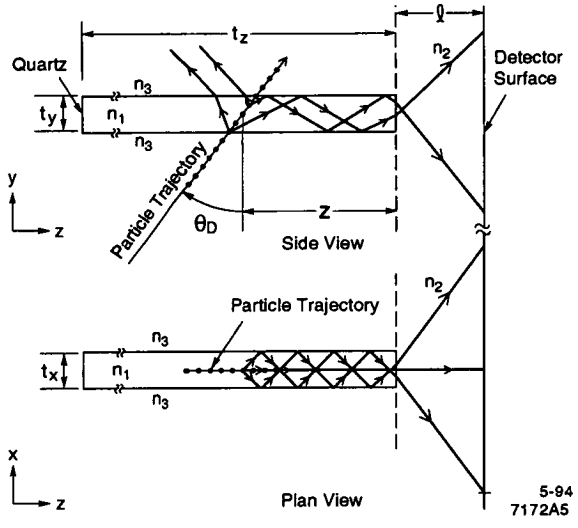

Figure 3-16. *The principle of the DIRC. The Čerenkov angle is preserved by total internal reflection as the Čerenkov light propagates along the quartz bar*

($n_2 \sim 1.43$) producing a Čerenkov ring image. The image is read out by a close-packed array of photomultiplier tubes arranged on a toroidal surface. To reduce the instrumentation area required there is a trapezoidal quartz wedge glued onto the end of each bar which folds one half of the Čerenkov ring image onto the other half, and reflects photons with large exit angles back onto the instrumented surface. In front of the PMTs are hexagonal concentrators to increase the total effective surface area to around 90%. From the radius of the Čerenkov ring θ_c is calculated. This determines the particle velocity and with momentum information the mass of the particle can be calculated. The resolution on the measurement of θ_c must be less than 2 mrad, since the K/π separation is 6.5 mrad at 4 GeV. The polar angle coverage (centre-of-mass frame) of the DIRC is 87% and the azimuthal coverage is 93%. For more details see [42, 43]

3.3.3.3 The electronic readout

The readout consists of 10752 fast photomultiplier tubes (PMTs) with 2.82 cm photocathodes. The PMTs are spread across such a large area that they are at most hit by one photon per event. Therefore only timing information, and not an amplitude measurement, is required to characterise a PMT hit. The timing resolution of the PMTs is 1.5 ns. They are operated at a gain of 1.7×10^7 which corresponds to a high voltage between 900V and 1400V. The output is input into 168 DIRC Front-end Boards (DFBs), each containing one time-to-digital convertor (TDC) [44] and two 8-channel custom analog chips. The analog chips perform the necessary discrimination to time the PMT pulses. The TDCs digitize the time information with 500 ps binning and place the data into a buffer to be readout when a level 1 accept signal is received from the *BABAR* DAQ system. There are 12 DIRC front-end crates each having one crate

controller (DCC) which serialises the data onto a 1.2 Gbits/s fibre optic Glink to be sent to readout modules in the electronics house. For more information see [45, 46]

3.3.4 The electromagnetic calorimeter

3.3.4.1 Physics requirements

The branching ratios for the exclusive B decays which are CP eigenstates are small. Therefore *BABAR* must be able to reconstruct neutral particles with high efficiency and good resolution. Generic B decays have a mean photon multiplicity of 5.5, and at the $\Upsilon(4S)$ resonance 50% of the photons have an energy below 200 MeV. Rare B decays contain photons with much higher energy *e.g.* $B^0 \to K^*\gamma$. This means that the electromagnetic calorimeter must have an excellent energy resolution over the energy range 20 MeV to 4 GeV. Many CP eigenstates have a π^0 as one of their final decay products. To be able to reconstruct the π^0's requires efficient photon detection, particularly at the lowest energies. The calorimeter must also be able to identify and measure electrons and positrons. This is important for tagging and to achieve sufficient e/μ and e/π discrimination.

The *BABAR* electromagnetic calorimeter is constructed from 6580 CsI (Tl) crystals held in place with a thin carbon fibre matrix. CsI (Tl) crystals were used successfully in the CLEO [47], and Crystal Barrel [48] calorimeters. The *BABAR* calorimeter design energy and angular resolutions are:

$$\frac{\sigma_E}{E} = \frac{1\%}{\sqrt[4]{E}} \oplus 1.2\% \qquad \sigma_{\theta,\phi} = \frac{3\text{mr}}{\sqrt[2]{E}} \oplus 2\text{mr} \tag{3.1}$$

The constant term in the energy resolution is due to shower leakage at the front and back of the crystals, non-uniformity in the crystals and the individual crystal calibration coefficients.

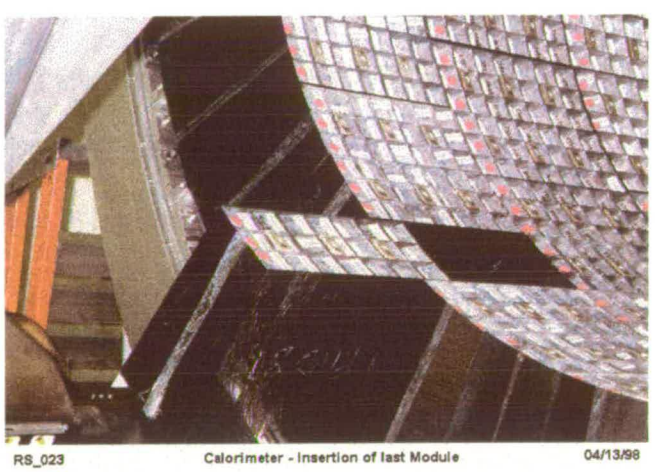

Figure 3-17. *Photograph of the BABAR electromagnetic calorimeter*

This energy resolution does not include electronics noise, or beam background. The angular resolution is calculated from the transverse crystal size and the mean distance to the interaction point. The minimum detectable energy for photons is expected to be 10-20 MeV based on the CLEO experiment. However, this will depend on the beam background.

3.3.4.2 The design of the electromagnetic calorimeter

Table 3-4. *The CsI(Tl) crystal properties*

Property	CsI(Tl)
Radiation Length	1.85 cm
Molière Radius	3.8 cm
Peak Emission	565 nm
Density	4.53 g/cm^3
Time Constant	940 ns
Light Yield	40-50k photons / MeV
Refractive index (peak emission)	1.79

There are two parts to the *BABAR* calorimeter—the barrel and the forward endcap. The barrel calorimeter is situated radially between the DIRC and the magnet cryostat. There is no backward endcap as it is not necessary due to the asymmetric nature of the PEP-II collisions. The polar angle coverage is $-0.775 \leqslant \cos\theta \leqslant 0.962$ (lab) and $-0.916 \leqslant \cos\theta \leqslant 0.895$ (centre-of-mass). The calorimeter is positioned off-centre and extends 2.3 m forwards and -1.56 m backwards.

The barrel calorimeter consists of 5760 crystals. The inner radius is 91.9 cm and the outer radius is 135.6 cm. It is subdivided in θ into 48 rings (see figure 3-18). Each ring is subdivided in ϕ into 120 identical crystals. The crystal lengths vary from 29.76 cm ($16.1X_0$) at the backward end to 32.55 cm ($17.6X_0$) at the forward end taking into account the effect of the boost on the photon energy spectrum. The calorimeter is mechanically constructed from 280 modules, each containing 7x3 crystals in θ and ϕ respectively. The exception to this is the backward ring of modules where there are only six crystals in θ. In each module the crystals are supported by a 300 μm thick carbon fibre "honeycomb" structure The modules are supported from the rear by an aluminium strong back which is attached to an aluminium support cylinder. The material in front of the calorimeter consists of two cylinders made from aluminium (1 mm thick) which are separated by foam. This provides a double RF shielding and a gas-seal. In addition there is material due to a liquid radioactive source calibration system which is equivalent to an additional 3 mm of aluminium. The barrel weighs 23.5 metric tonnes.

The endcap consists of 820 crystals and weighs 3.2 metric tonnes. It is supported from the barrel support cylinder ensuring good alignment between the two systems. The gap between the barrel and endcap is $\approx$ 2mm. The endcap is made up of 8 rings of crystals in θ. There is an

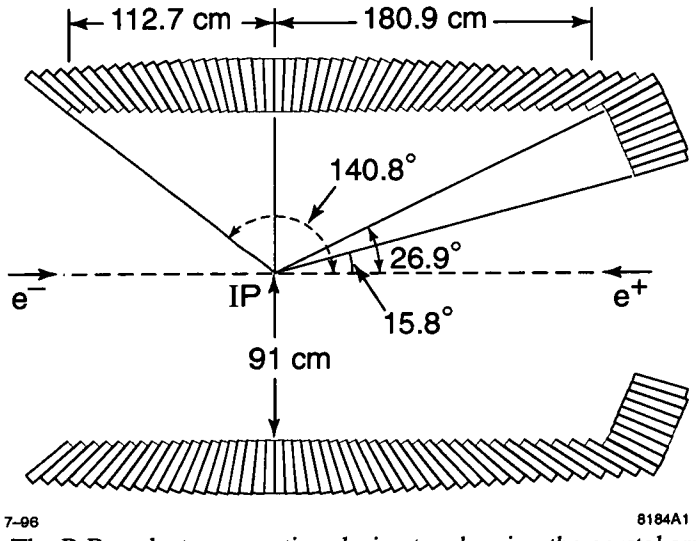

Figure 3-18. *The BABAR electromagnetic calorimeter showing the crystal arrangement in θ and its angular coverage.*

additional inner ring which contains lead shielding, but has been designed so it could be filled with CsI crystals. This would further increase the forward angular coverage down to 250mr. The three θ rings which are closest to the barrel each have 120 crystals in ϕ matching the barrel. The next three rings have 100 crystals and the last two rings have 80 crystals. All of the crystals are 32.55 cm long except for the inner ring which is one radiation length shorter due to spatial restrictions. The endcap is broken up into 20 modules in ϕ, each containing 41 crystals.

The properties of CsI(Tl) crystal are listed in table 3-4. For details of their photo-electron yield see [49]. The crystals are wrapped in two layers of 150 μm Tyvek 1056D and one layer of 30 μm aluminium foil. The Tyvek provides diffuse reflection and the aluminium RF shielding. The wrappings and carbon fibre produce a 1.25 mm gap between crystals. The gaps in θ are non-projective to reduce the number of photons which could traverse the gaps. Due to the identical shape of the crystals in ϕ the gaps here are projective. The calculated loss due to photons passing through these gaps is 2.5%.

3.3.4.3 The electronic readout

More information on the calorimeter electronics can be found in [50, 51, 52]. The crystals are readout by two Hamamatsu S2744-08 large area (10×20 mm^2) diodes which are glued to the rear of the crystals. The capacitance of the diodes is approximately 80 pF. For details of the photo-diode readout see [53]. Each pair of diodes is connected via a 3 cm flat cable to custom charge sensitive BiCMOS preamplifiers with gain 1 and 32 output drivers (fully differential). They have short shaping times of 0.25 μs (integration) and 0.8 μs (differentiation). The

output from each preamplifier is a 13-bit "fan-out" (ribbon) cable which goes to the Custom Auto Range Encoding integrated circuit (CARE chip). The CARE chip splits the gain into 1,4,32,256 ranges and autoselects the appropriate range. This allows the system to reach 18 bits of dynamic range. The output is then digitized by a 10-bit ADC. The CARE chips and ADCs are contained on 6 layer boards (ADBs) which are mounted on the detector. The data then go to a detector mounted Input/Output board (IOB). This encodes the data onto high speed (1.2 Gbits/s) fibre-optic Glinks. In the electronics house the data are collected in the calorimeter read-out modules (ROMs). A photograph is shown in figure 3-19. The ROMs consist of a 9U VME card which contains a commercial power pc chip. The mode of operation for the calorimeter is different from the other sub detectors. The data are collected by untriggered personality cards (UPCs) which receive a continuous stream of data coming from the calorimeter. This allows the calorimeter to achieve good signal-to-noise ratio (S/N) in the presence of beam backgrounds. The sampled data are digitally filtered using a large sample of data taken before and after each event. These digitally sampled data are also used to provide trigger "tower" sums for the level 1 electromagnetic trigger (EMT).

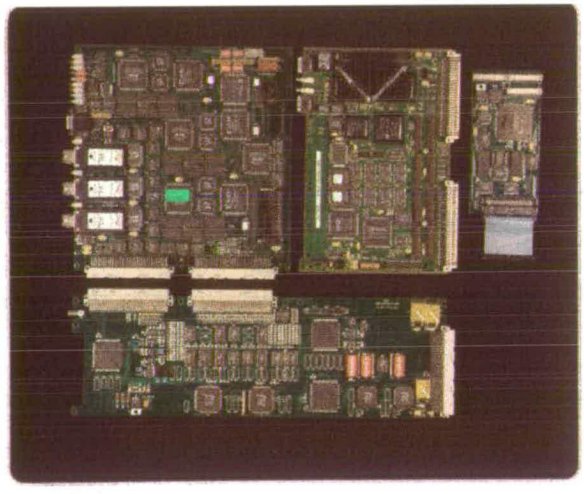

Figure 3-19. *Calorimeter readout module*

3.3.5 The instrumented flux return

3.3.5.1 Physics requirements

The main aim of the *BABAR* instrumented flux return (IFR) is the identification of muons. This is particularly important for tagging purposes. The majority of muons originating from a B decay come from semi-leptonic decays of B mesons directly, or indirectly from cascade D mesons. The muon momentum spectrum is peaked at about 1.2 GeV for muons from direct

$b \to \mu$ decays and for indirect cascade $b \to c \to \mu$ decays it is lower. The direct semi-leptonic decays are vital to be able to measure $|V_{cb}|$. The IFR is designed to detect muons down to 500 MeV. This results in a B tagging efficiency of around 9% [54].

The second objective of the IFR is the detection of neutral hadrons, in particular K_L^0 mesons from the CP eigenstate $B \to J/\psi K_L^0$ which may be used to calculate $\sin 2\beta$. Approximately 55% of these events will start to interact in the electromagnetic calorimeter before reaching the IFR which increases the detection efficiency and angular resolution. About one third of the K_L^0 mesons will not interact until they reach the IFR and there must be at least four layers hit in the IFR in this case to give a reasonable efficiency [22].

3.3.5.2 The design of the IFR

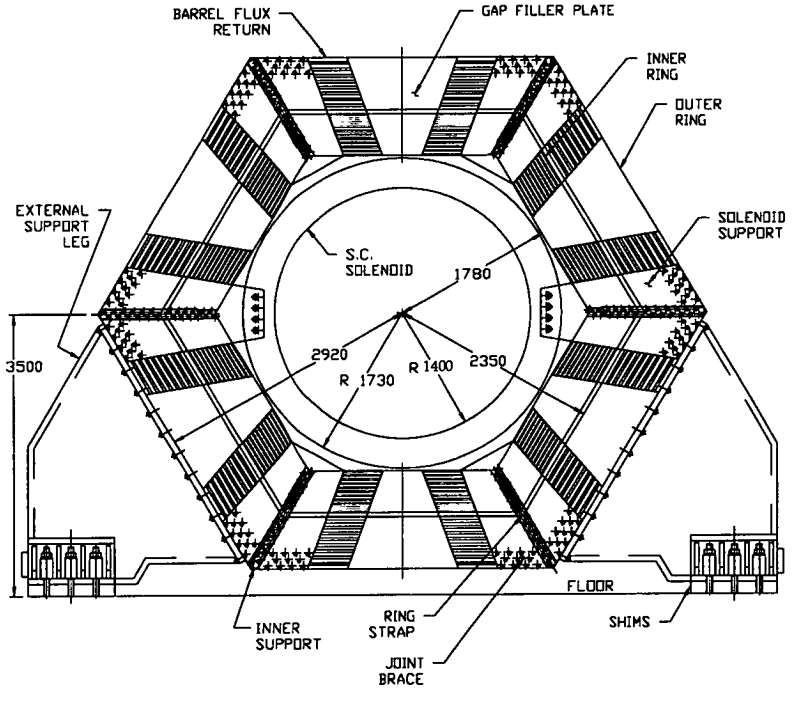

Figure 3-20. *Cross-sectional xy plane view of the IFR and magnet*

The *BABAR* iron flux return is segmented and instrumented with resistive plate chambers (RPCs). It has three main parts—the central barrel section and two end-caps. The segmentation of the iron is graded with increasing thickness radially from the interaction point. Detailed studies [54] have shown that low momentum muon identification and K_L^0 detection occurs with finer segmentation with special emphasis on the first absorption length. The graded iron segmentation of the IFR has been optimised to provide the best efficiency whilst not increasing excessively the number of layers.

The IFR barrel is 3.75 m long and the inner and outer radii are 1.78 m and 3.01 m respectively. The iron segmentation is made up of 18 plates with a total iron thickness of 65 cm. The inner nine plates are 2 cm thick, followed by four plates 3 cm thick, three 5 cm thick and the two outermost ones are 10 cm thick. The plate separation is 3.2 cm except for the inner nine plates which have 3.5 cm separation. There are 21 active layers. Surrounding the electromagnetic calorimeter is a double layered cylindrical resistive plate chamber (RPC), one set of planar RPCs between the solenoidal coil and the iron, 17 layers in the gaps and one last layer out with the iron structure. A cross-sectional view is shown in figure 3-20. The barrel is hexagonal in cross-section and is split into six sectants. Each gap in each sectant contains three planar RPCs, 125 cm × 181-320 cm, which are joined along their long edges (perpendicular to the beam axis). The cylindrical RPC has a radius of 147 cm and is constructed from two layers which each have four quarter cylinder modules. The module dimensions are $115 \times 190\,\mathrm{cm}^2$.

The endcaps are also hexagonal in cross-section and are split vertically to allow opening the "magnetic doors" for access to the inner detectors. The total iron thickness is 60 cm. The iron has the same segmentation as the barrel except that the outer two iron plates are 5 cm and 10 cm thick. There are 18 layers of RPCs starting from behind the innermost iron plate. There are 6 modules in each layer making a total of 216 modules for both endcaps.

The polar angle coverage of the IFR is from 300 mr in the forward direction to 400 mr in the backward direction (laboratory).

3.3.5.3 The electronic readout

The *BABAR* resistive plate chambers [55] have a 2 mm gas gap which is held at atmospheric pressure. The gas mixture chosen is a comparable quantity of argon and Freon 134A ($C_2H_2F_4$) mixed with a few percent of isobutane (C_4H_{10}). This choice enables the chambers to work in streamer mode, but without any risk of inflammability. The gas is enclosed between two bakelite plates, 2 mm thick, which are high resistivity (10^{11}-$10^{12}\,\Omega\,\mathrm{cm}$). The outer sides of the bakelite plates have a coating of graphite which is used to apply the high voltage potential (8 kV) across the gas gap. The external induction electrodes are made from aluminium strips glued on a plastic support and insulated from the graphite coated bakelite sheets using a 300 μm PVC film. The RPCs are double sided with readout strips arranged with 90° stereo on either side. On the outside of the RPCs is a grounded 40 μm thick aluminium plane which is insulated from the iron by a laminated layer of mylar. Detailed information on the principle of operation, and performance of resistive plate chambers is given in [56, 57, 58]

The RPC readout strips in the barrel have a 38.5 mm pitch in the z-direction and a ϕ pitch varying between 19.7 mm and 33.5 mm. The endcaps have a horizontal pitch of 28.4 mm and a vertical pitch of 38 mm. The strips are readout by Front End Cards (FEC) which each serving 16 channels. The FECs discriminate the data selecting the active channels which are passed to a time-to-digital convertor which has 1 ns resolution. This is done by fixed threshold electronics due to the large signal (~300 mV) produced by the RPCs. When a level one accept takes place the data is placed into a parallel-in/serial-out shift register and is transmitted to

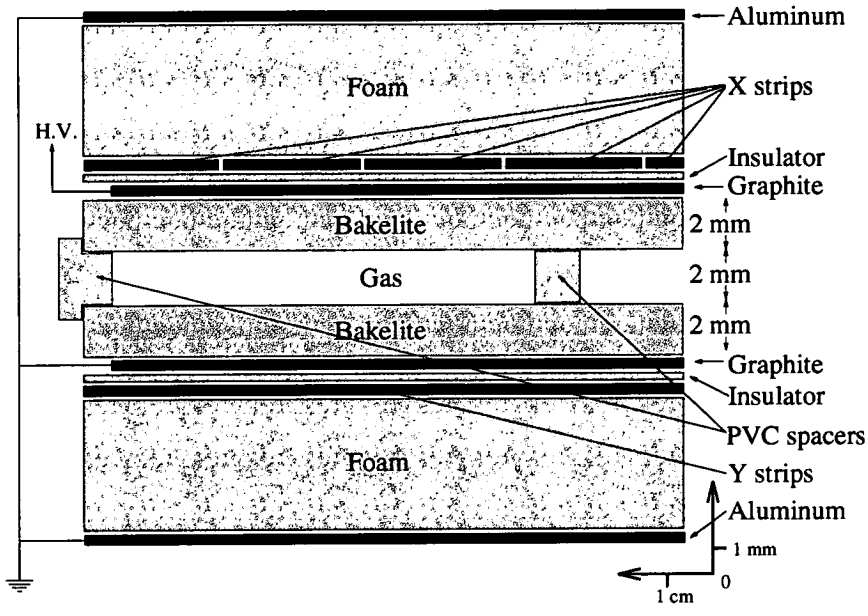

Figure 3-21. *Cross sectional view of the RPC type used in BABAR's instrumented flux return.*

a first-in/first-out (FIFO) board, called IFB. Each IFB collects the data from 64 FECs. The front end readout takes place within 2.2 μs. The data are then transmitted to the BABAR DAQ system via 1.2 Gbits/s fibre optic Glinks to the Read out Modules (ROMs). The FECs are located within the detector, but the IFBs can be accessed without opening the endcaps. For more details see [59]

There is also an IFR trigger which is used to select events that have at least one muon candidate. This can be used for calibration purposes *e.g.* selecting cosmic muon events or selecting $e^+e^- \to \mu^+\mu^-$ data samples. It can also be used to select useful data in the event of high machine backgrounds. Some of the FECs continuously send real-time information about the activity of their channels to a Partial-Or board which calculates an OR of the data. There are eighteen Partial-Or modules in total. The output is then passed to a Majority Logic board which generates a Master-Or of each layer and produces trigger objects. More details on the IFR trigger may be found in [60].

3.3.6 The superconducting magnet

The BABAR superconducting solenoid produces a central magnetic field of 1.5 T. The field uniformity is $\pm 2\%$ within the tracking volume ($r < 80\,\text{cm}, -1.17\,\text{m} < z < 1.91\,\text{m}$). The superconducting windings consist of 20 Rutherford NbTi/Cu wires which are embedded in a pure aluminium matrix, using a coextrusion process. The windings are cooled to an operating temperature of 4.5 K by liquid helium. They are directly wound inside an aluminium support

cylinder and impregnated with epoxy. To meet the requirements for field uniformity the current density has to be higher at the ends than in the central region. Therefore there are two different winding types—thinner windings at the ends (3.6 mm) and thicker ones in the central region (6.2 mm). In total there are 315 turns in the central region and 210 turns in each of the end regions. The superconducting solenoid is surrounded by a cryostat consisting of a tubular vacuum vessel containing the cold mass and thermal shielding held at 80 K. The solenoid is located outside the calorimeter, between the inner cylindrical RPC and the IFR see figure 3-20. The operating current is 6830 A and the peak field at the windings is 2.5 T. For more details see [61].

3.3.7 The trigger

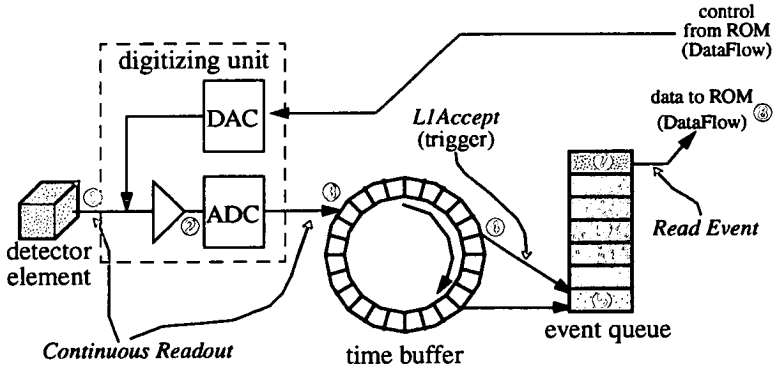

Figure 3-22. *The role of the trigger in data flow*

The main design requirement for the trigger is that it must have excellent efficiency for selecting B physics events. For details of the efficiency requirements see the trigger system requirements document [62]. In addition, the event time (t_0) is reconstructed in the trigger because *BABAR* has a high beam crossing rate (238 MHz), with no detector fast enough to signal an e^+e^- annihilation.

The *BABAR* trigger has a multi-level architecture which is common to high luminosity experiments, *e.g.* CLEO [47]. There are two separate levels—a level 1 decision which is executed in hardware and a level 3 decision which is implemented in software after the event assembly. The level 1 trigger selects events at a maximum sustained rate of 2 kHz based on a set of primitives constructed from the drift chamber, calorimeter, and instrumented flux return. The level 3 trigger uses the online event processing system (OEP) to select events for data storage at a rate of 100 Hz. In addition to selecting physics events the level 3 categorises events for calibration (*e.g.* Bhabha events). The structure of the dataflow and the trigger decisions, is shown in figure 3-23.

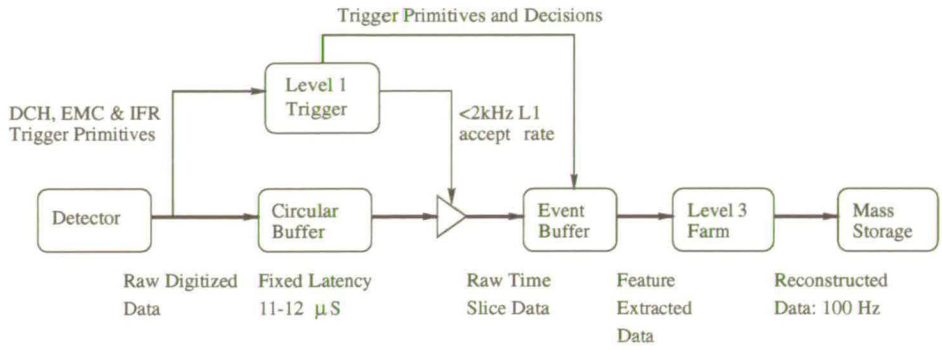

Figure 3-23. *The BABAR trigger structure and data-flow*

The level 1 trigger is made up of a drift chamber trigger, an electromagnetic trigger, and an instrumented flux return trigger, each providing input primitives into a global trigger which makes the final level 1 decision. The elementary trigger objects are described in [63]. They are long tracks (p_t 180 MeV), short tracks (p_t > 120 MeV), and calorimeter trigger tower sums. The calorimeter towers are made from splitting the calorimeter into 40 ϕ strips, which are further divided into 7 θ segments. The individual crystal energies in each tower are added to give tower sums. The level 3 trigger algorithms consist of vertex cuts, timing cuts and track matching between the silicon vertex tracker and drift chamber. Bhabha events and two photon events are pre-scaled to flatten their angular distributions and to filter the total rate down to a sufficient level. For more details see [64].

3.4 Chapter summary

The BABAR detector is specially designed to measure CP violation in the B meson system. This has required new developments in detector and accelerator design. We have discussed the PEP-II storage ring, for which the most important design considerations are the asymmetry and the design luminosity of $3 \times 10^{33}\text{cm}^{-2}\text{s}^{-1}$. Due to the high luminosity there may be large backgrounds in the detector. We have covered each sub detector highlighting in particular the physics motivations which have driven their subsequent design, and the operation of their full electronic readout. In the next chapter we will discuss in more detail the electromagnetic calorimeter.

4

Calibration and monitoring

4.1 Introduction

The calibration and monitoring of the *BABAR* electromagnetic calorimeter is a key component of its operation. In this chapter we will describe the general philosophy and motivation. Then we will cover briefly the various factors which may change the response of the calorimeter. Then the various different calibration methods and technologies used by *BABAR* will be described. In later chapters the research and design of the fibre-optic light pulser system will be discussed in detail and data from this system will be shown. For more details of the calibration and monitoring of the *BABAR* electromagnetic calorimeter see [65].

4.2 Motivation for calibration and monitoring

The *BABAR* electromagnetic calorimeter has demanding performance goals. To meet the physics requirements and maximise its potential the calorimeter must provide an excellent energy resolution and be able to reconstruct neutral particles efficiently. This is particularly important in the low energy range to obtain good π^0 reconstruction efficiency. It is essential that the energy scale of the calorimeter is calibrated precisely and that the system is continuously monitored for any variations in response. The target energy resolution as specified in the *BABAR* Technical Design Report [66] is shown in figure 4-1. A beam test [67] and shower calculations using Monte Carlo have shown that the CsI(Tl) calorimeter is capable of attaining an energy resolution of around 1.5% at 1 GeV and around 3% at 20 MeV. To achieve this desired resolution for low energy photons requires that individual crystals having energy deposits down to 0.5 MeV be included in the shower sum calculations.

4.3 Radiation damage and CsI(Tl) scintillation light

CsI crystal doped with thallium is an inorganic scintillator. The mechanism for the scintillation depends on the energy states available which are determined by the structure of the crystal lattice. The CsI crystal has well defined valence and conduction bands and thallium is introduced as an impurity which modifies the energy levels. This increases the light yield for a given electromagnetic shower and it also changes the wavelength of the scintillation light.

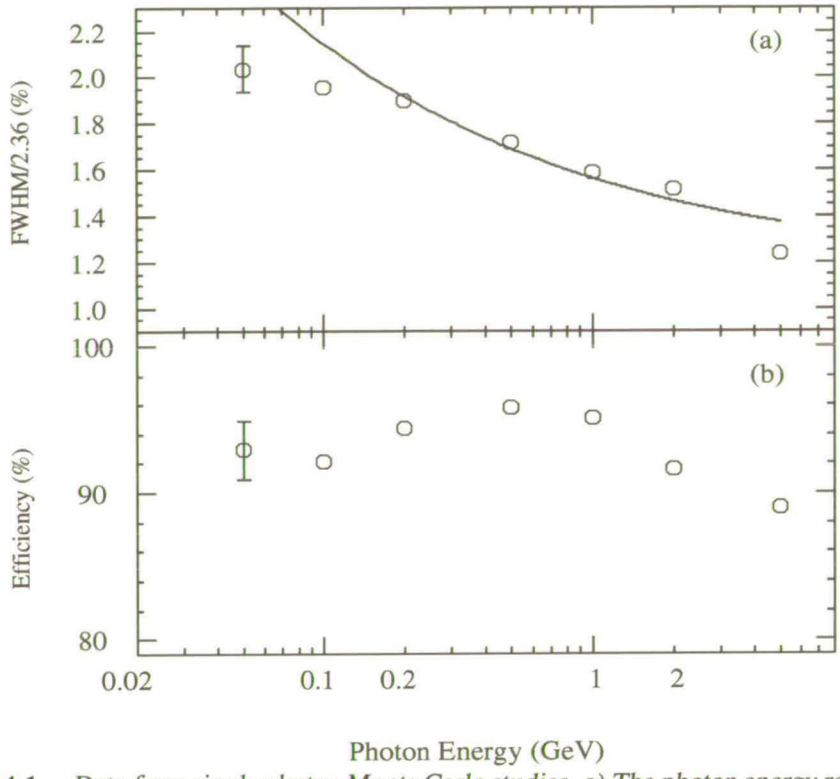

Figure 4-1. *Data from single photon Monte Carlo studies. a) The photon energy resolution of the calorimeter and (b) detection efficiency, as functions of energy, at 90°. The solid line shows the target energy resolution*

All crystals suffer from radiation damage which causes changes in the crystal response. This is not believed to affect the scintillation mechanism [68, 69]. The radiation damage results in the formation of colour centres in the crystal which introduce absorption bands. These are produced when radiation causes a atoms to be displaced from their lattice position. Therefore radiation damage results in a loss of light output. This is more severe at the front face of the crystals and results in non-uniform light output from electromagnetic showers.

4.4 Changes in the calorimeter response

There are a number of factors which can change the response of the calorimeter. Ionising radiation from the high luminosity PEP-II beams is unavoidable. The main source of this is due to lost beam particles which produce electromagnetic showers. This results in a gradual degradation of the light output from the crystals. This may lead to changes in the uniformity of light collection in the crystals. These effects have to be understood and corrected for if electromagnetic showers are to be reconstructed with the best energy resolution. It is important for the radiation damage to be continually monitored and studied closely. The

radiation dose to the crystals can be substantially increased by periods of machine tuning, injection losses and unexpected beam dumps. The light loss due to radiation damage is known to be from decreased absorption length, not a decrease in scintillation light from the crystals. Apart from radiation damage there are several other effects that can change the response of the calorimeter:

- Temperature variations in the calorimeter (these are controlled to less than 1°C).
- Surface changes in the CsI(Tl) crystals or their wrappings.
- Optical and physical changes in the crystal-diode glue joint.
- Variations in the electronic readout chain due to:
  - dead channels
  - electronics noise
  - feature extraction (see below).
  - accuracy of the electronic calibration

The analogue energy pulse coming from the calorimeter channels is converted by the ADBs to a digitised waveform. Feature extraction is the means by which the energy of the pulse is extracted from this digital waveform. The may involve either a relatively straightforward polynomial peak finding algorithm, or a full weighted digital filter algorithm where the energy of the pulse is then taken from the filtered waveform. For more information see [70].

4.5 Calibration methods

There are two main hardware systems for the *BABAR* calibration and monitoring: a radioactive source calibration system (6.1 MeV photons) and a fibre-optic light pulser monitoring system. There are also various physics processes which produce well defined energy deposits in the calorimeter which can be predicted accurately from other detector and simulation information. These processes are π^0 decays, Bhabha and radiative Bhabha events, $e^+e^- \to \gamma\gamma$ events, and minimum-ionising particles such as muons from $e^+e^- \to \mu^+\mu^-$ events or cosmic rays.

4.5.1 Radioactive source calibration

The source calibration uses a radioactive fluid. It is distributed in a set of thin tubes which are situated directly in front of the CsI(Tl) crystals. The fluid is fluorinert which contains fluorine atoms. These are activated by a neutron source, producing ^{16}N isotopes. These isotopes decay producing 6.1 MeV photons which deposit their energy in the front face of every barrel and endcap crystal. This provides an absolute calibration point which precisely sets the the

initial scale of each crystal. Subsequent calibrations are then carried out to monitor long term changes in the crystals. The source calibration at 6.1 MeV requires that there is no beam passing through the detector. To avoid significant loss of integrated luminosity it is likely that these calibrations can only be performed once per week.

4.5.2 The light pulser system

The light pulser system uses optical fibres to inject light from a xenon flash lamp into the rear of each crystal. The spectra of this light is matched to the emission frequency of the CsI(Tl) scintillation light. This does not allow the absolute energy scale for each crystal to be set, but it does allow monitoring of relative change in the response of the calorimeter between subsequent light pulser runs. This is very useful to continually check the calorimeter for any changes in response including the effects of radiation damage. It also provides a quick diagnostic check of the functionality of the readout electronics. The light pulser runs are very fast, and can be taken with or without beams. This means that light pulser runs have a low impact on the total integrated luminosity.

4.6 Calibration versus monitoring

The objective of the *calibration* is to establish the direct relation between incident photon energy and the response of the calorimeter. To achieve this, the relationship between the energy deposited in individual crystals, and the digitised signal that is sent to the data acquisition system, must be known precisely. This is known as the *single crystal calibration.* The relationship between the photon's energy and the sum of the energy depositions in individual crystals, is dependent on the shower-clustering algorithm used, and changes for different incident angles and energies. This is known as the *shower energy calibration.* It is also very important to be able to monitor quickly the short term changes in the response of individual crystal channels. This can be used to indicate problems and to diagnose them. This is known as *monitoring*. Calibration is usually thought of as being functionally distinct from monitoring. However, any system or process which can be used to measure calibration changes is also performing a monitoring function, and can be used to identify channels which are not functioning properly and to flag unusual behaviour.

4.6.1 Calibration

The single crystal response depends on a number of different factors, all of which may undergo temporal variations. These factors and the effects which may cause variations in them are shown in table 4-1.

Table 4-1. *Factors which change the response of the calorimeter*

Factors changing the calorimeter response	Effects which can change these factors
Scintillation properties of CsI(Tl)	Chemical composition
Absorption properties of CsI(Tl)	Radiation damage
Light collection uniformity	Radiation damage, wrapping
Optical coupling to photodiodes	Changes in glue joints
Response of preamplifier/digitisation chain	Dead channels, electronic noise

The calibration process has three parts, or more accurately applies corrections in three different places:

1. The ADC values in the data acquisition system before feature extraction. These values are obtained from an electronic calibration.
2. Individual crystal energy depositions. The single crystal calibration is obtained initially using 6.1 MeV photons from the source calibration. A second set of crystal constants are obtained from Bhabha events. These two processes provide low and high energy calibrations spanning the range of interest.
3. Photon energies measured from cluster-sums. The shower energy calibration depends on a number of geometrical factors.

There are a number of geometric factors which affect the response of the calorimeter. There is non-sensitive material in the calorimeter which absorbs energy which will be missing from the shower sum. There is energy loss between the crystals which is especially true at high polar angles due to the staggering of the crystals. There is also energy loss from the rear of the crystals occurring for high energy photons which is energy and position dependent. There must also be additional corrections for the varying amount of material in front of the calorimeter. The lost energy corrections are determined by Monte Carlo simulation, and analysis of data.

4.6.2 Monitoring

The most important goal of monitoring is diagnostics. The functionality of the crystal readout chain must be continually tested and this trouble-shooting must occur with or without beams. The diagnostic tools are necessary throughout the lifetime of the experiment, but are crucial during the start-up phase to debug problems. It is useful if the monitoring can indicate if the origin of a given problem is optical or electrical. A second goal is to track gradual changes in the response of the crystals to record deterioration and possible degradation in the calorimeter performance.

The monitoring should be ongoing during normal running conditions. If any discontinuity is observed additional diagnostic monitoring runs can be taken. The light pulser system which

uses a xenon light source distributing the light to individual crystal channels performs this function and was used throughout the construction and startup phases to diagnose and debug problems. It can be used to check if the channel is taking data, to indicate possible causes, and the actions required to rectify them *e.g.* is it an entire readout-module failing or is it due to an isolated channel which is noisy? The radioactive source calibration system can be used to provide additional short-term diagnostic monitoring, as well as providing long term monitoring of gradual changes.

4.7 The electronic calibration

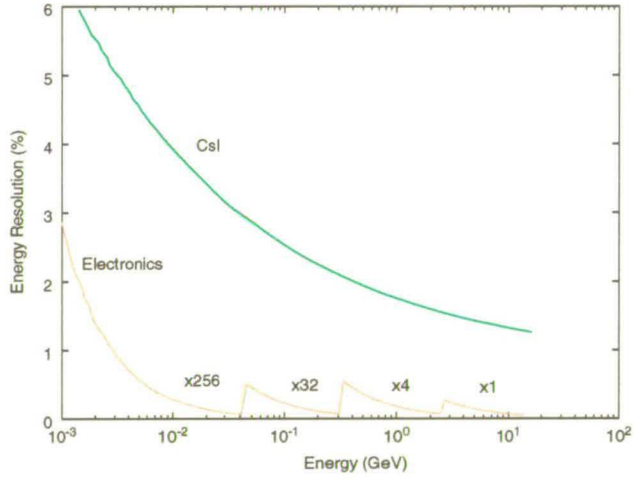

Figure 4-2. *The digitisation resolution of the calorimeter for the various gain stages of the CARE chip*

The design goal of the electronics calibration is to linearise the response of the front-end electronics to better than 0.1% in each of the four ADC ranges. The electronic calibrations are performed while beams are off and occur approximately every two months. In addition to deriving the electronic calibration, the functionality of the front-end system is tested. The intrinsic resolution of the electronics for the various gain stages of the CARE chip is shown in figure 4-2.

The electronic calibration is performed by a charge injection system. This is built into the preamplifier chip ASIC. The magnitude of the charge to be injected is set using a DAC on the I/O board. The charge is deposited on either of two calibration capacitors which feed into the input stage of the preamplifier. This occurs when a calibration strobe is received from the fast control system. This is then processed by the various gain stages in the preamplifier and

CARE chip, and the signal is digitised by the sampling ADC on the CARE chip. Comparing the magnitude of the input charge and the ADC sample peak allows the response function to be mapped out. The corrections required to linearise the electronics response are then calculated.

The corrections are applied to the calorimeter readout prior to the digital filtering stage. For every ADC channel the corrected value, multiplied by an overall energy scale factor derived from the source and Bhabha calibrations, is stored in a lookup table (LUT) holding 16-bit integers. This is then used as the input to the feature extraction and trigger energy sums.

4.8 Radioactive source calibration

For detailed information on the design and goals of the radioactive source system see [65, 71]. The main objectives are to determine the single-crystal calibration constants, and to monitor the changes in light collection due to crystal radiation damage or to degradation in the optical couplings, surfaces or wrappings.

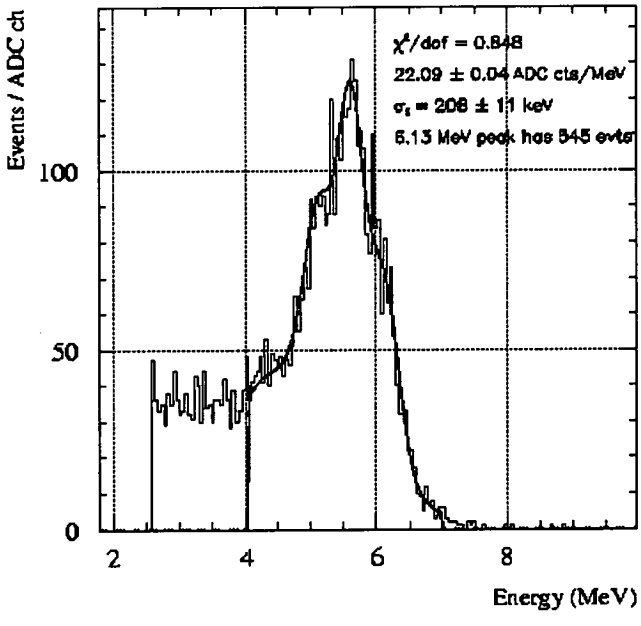

Figure 4-3. *Radioactive source peak*

The fundamental feature of the source calibration is that it provides an absolutely known and stable photon energy deposit in each and every crystal. This in turn provides a readily determined low-energy point on the photon response curve. The source allows diagnostics on the entire readout chain from the scintillation light through to the digitisation. It also allows for a measurement of noise directly in units of energy.

The radioactive fluid used for the source calibration is fluorinert (mostly C_8F_{18}). The fluorine atoms are activated by a neutron source which is a (d,t) tube. The activation occurs through the $^{19}F(n,\alpha)^{16}N$ reaction, producing ^{16}N isotopes. The ^{16}N nuclei have a β-decay to an excited state of ^{16}O with a half-life of 7 seconds. There is then a transition from the excited state to the ground state of ^{16}O with the emission of a 6.13 MeV gamma. Three peaks are observed corresponding to the full energy, a single escape peak, and a double escape peak. They are separated by the electron mass (511 keV). A fit is made to a combination of these, shown in figure 4-3.

The effective data rate in each crystal is around 5 Hz. This depends on the activation strength and the efficiency of the data acquisition. A digital filtering algorithm is used to reduce the electronic noise level. For the nominal noise 150 keV, a precision of 0.25% can be attained in less than 15 minutes. However reduced light yield due to radiation damage or a diode failure raises the noise level significantly.

Source calibrations must be performed with the beams off due to the low energy of the photons and the low intensity. The source calibration runs take place once per week.

4.9 The light pulser calibration

The main objective of the light pulser system is to monitor continuously relative crystal responses to a precision of better than 0.5%, and to provide a convenient and flexible diagnostic tool for the complete readout chain from light collection through to data acquisition. The equivalent energy produced in each crystal is large enough that calibration runs can be taken when there is beam through the detector. The light pulser runs are very fast and efficient. They can take place during the short periods after beam top-up when the drift chamber high voltage is being ramped up. This results in little, if any, reduction in data taking time. This is very important as the total integrated luminosity is vital to measure *CP* violation. The system can provide rapid feedback on problems and is used frequently to debug electronics problems and to check the calorimeter after the repairs have been carried out. The light pulser system is designed to be stable over times of order one week. The data taken from light pulser runs can be used to interpolate between primary calibrations if this accuracy is required.

More details of the design of the light pulser system will be covered in the next chapter. Briefly, the system consists of two xenon flash lamps which produce light for the barrel and endcap. This light is spectrally filtered and attenuated to the correct wavelength band and brightness. It is sent to the rear face of each crystal via a series of fibre optics. This light passes down through the crystal and reflects off the sides and front face. The calorimeter is then triggered at the correct time and this information is read out. The time and wavelength spectrum of the light pulses is matched to that of the CsI(Tl) scintillation light. The attenuation of the pulses can be changed allowing the brightness of the light to be adjusted over a series of points covering the full dynamic range. The light from the light pulser is itself continually monitored on a pulse-by-pulse basis by a reference system. We will come back to the details of this later.

The following performance goals were set in December 1996:

- Relative response of the crystals within a single module accurate to 0.1% on a pulse-to-pulse basis.
- Module-to-module differences accurate to 0.3% on a pulse-to-pulse basis.
- Absolute response, using the reference system, accurate to 1% over the period of one week.
- Linearity of response, using a set of neutral density filters accurate to better than 1% during a linearity run.

These numbers were based on the experience of the L3 experiment which used a similar light pulser system.

4.10 Bhabha calibration

Another method to obtain precise single-crystal calibration constants is to use Bhabha scattering events. At design luminosity it takes around one day to accumulate enough data to attain 0.25% per crystal. This method of calibration has been used very effectively by the CLEO collaboration and provides their primary source of calibration information. The Bhabha events provide both a single crystal calibration and a shower energy calibration for high energy electrons. The shower energy calibration for high energy photons differs from that for electrons by about 1%. This is obtained from $e^+e^- \rightarrow \gamma\gamma$, and radiative Bhabha events.

The kinematics of Bhabha scattering events are well defined. If there is any initial or final state radiation it alters the topology of the event and the event is characterised by the level 3 trigger as a radiative Bhabha (see next section). The electrons and positrons which are produced have an energy varying between 3 GeV at the rear of the calorimeter to 9 GeV in the most forward region of the endcap. These are the maximum energy showers which are produced in the calorimeter from e^+e^- annihilation at the $\Upsilon(4S)$. The Bhabha events are detected by looking for e^+e^- coincidences. For the case where the positron hits one of the seven most backward rings of the calorimeter, the corresponding electron is lost down the beam pipe, and only the positron can be reconstructed. Lastly, the most forward and backward crystal rings are difficult to calibrate using Bhabha events because calibration of these rings must be done based on energy-sharing with the next ring in.

The cross-section for Bhabha scattering events is strongly peaked in the forward and backward directions, see figures 4-4 and 4-5. This results in a limited rate in the central part of the barrel. At design luminosity the minimum rate of particles in the central region is about 30 particles per crystal per hour ($\theta = 60°$). It takes around 200 particles per crystal to achieve a statistical precision of 0.25% on the calibration constant. Therefore it is expected that every crystal

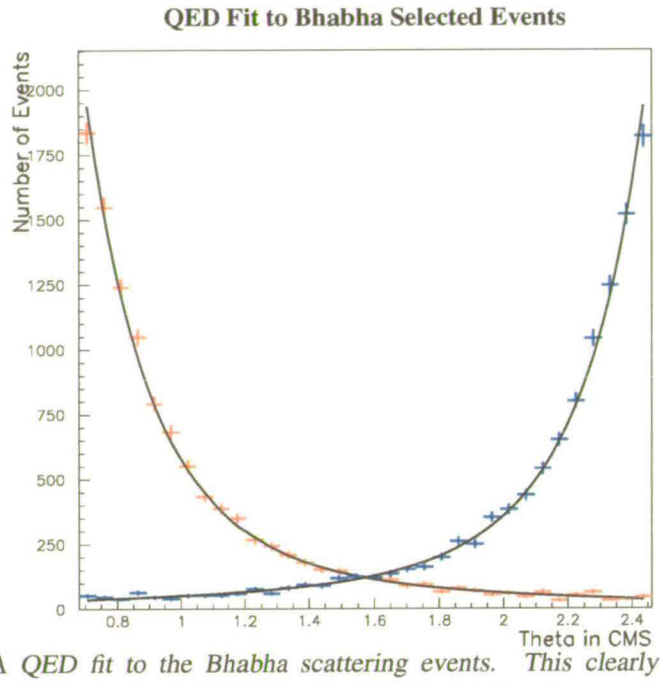

Figure 4-4. *A QED fit to the Bhabha scattering events. This clearly shows that the distribution is strongly peaked in the forward and backward direction*

could be calibrated to this precision in about eight hours. A Bhabha accept and reject will be switched on in the level 3 trigger. The Bhabha accept will let through a 5 Hz rate of Bhabha events which are prescaled in such a way to flatten the event yield as a function of theta.

The high energy showers from Bhabha events can spread over 25 crystals or more. To obtain single-crystal constants from this the difference between the measured and expected shower energy must be minimised. The shape of the measured energy distribution is not Gaussian. It has a low energy tail due to three factors: the radiative Bhabha background, bremsstrahlung photons, and shower leakage. This means that the peak position needs to be adjusted. This is done using Monte-Carlo calculations. This occurs as a function of polar and azimuth angle, and all the Bhabha peaks must be correlated to the expected electron/positron energy at a particular scattering angle. Lastly, the beam axis is not quite parallel to the *BABAR* axis. This introduces a 1% variation in the Bhabha energy in a theta ring as a function of phi.

The most important limitation of the Bhabha calibration is that the maximum accuracy depends on a full understanding of the lost-energy correction. The unfolding procedure for the shower is intricate. It was expected that Bhabha events would take a while to reach a useful degree of accuracy.

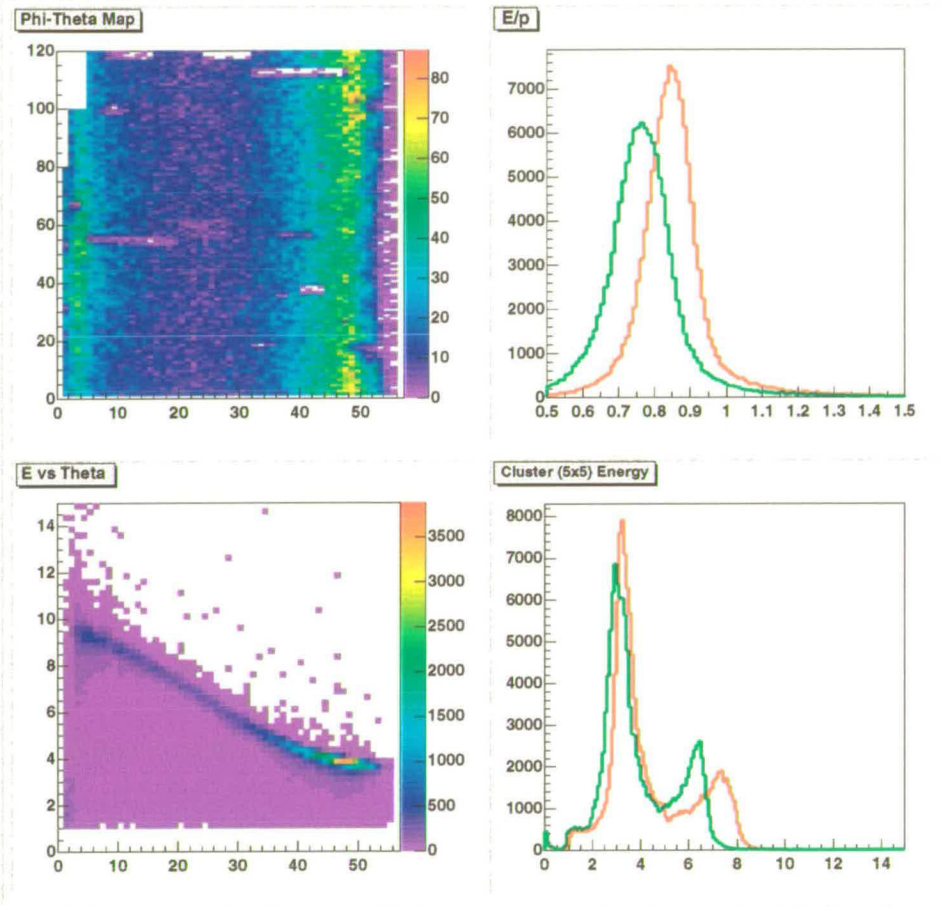

Figure 4-5. *Energy distribution of Bhabha scattering. The plots on the left show the energy distribution vs. theta-phi and the energy distribution vs. theta. The top right plot shows the E/p ratio. The green curves show the data before the Bhabha calibration constants were applied and the red curve is the data after the calibration constant were applied.*

4.11 Radiative Bhabha calibration

Radiative Bhabha events can be used to get shower energy calibrations for both photons and electrons over the energy range from a few hundred MeV to a few GeV. The photons that are produced in the radiative Bhabha events cover the whole kinematically allowed energy range and the entire polar angle.

To perform the photon energy calibration the electron and positron momenta are measured in the tracking detectors. The photon direction is measured from the position of the calorimeter cluster. Using a kinematic fit it is possible to predict the radiative photon energy, and to remove background. Due to the large backgrounds for lower photon energies the energy

resolution worsens. From experience with the CLEO detector it is expected that there will be a low-energy threshold for calibration with this process between 300 and 500 MeV.

The cross-section for radiative Bhabha events is much smaller than the cross-section for non-radiative Bhabha events since many of the radiated photons are lost down the beam pipe or remain too close to the electron or photon that they originated from. The radiative Bhabha calibration is difficult and to get the best calibration geometric effects such as variation in crystal length and stagger need to be considered. It takes around one week of data taking to accumulate enough statistics to calibrate the energy response of a crystal ring to 0.25%.

4.12 Neutral pion decays

Around half of the photons produced in B decays have an energy below 200 MeV. Therefore it is very important for the calorimeter to be efficient and well calibrated at low energies. The design requirement is the ability to measure with high efficiency and resolution photons down to 20 MeV. The majority of the low energy photons originate from neutral pion decays ($\pi^0 \rightarrow \gamma\gamma$). Around 18% of all the π^0's produced in generic B decays produce one photon with an energy between 20 and 50 MeV, and 55% have one photon between 20 and 100 MeV. The reconstruction efficiency of exclusive B decays depends on the ability of BABAR to measure π^0's with a good mass resolution.

This abundance of π^0's can be used to check the photon energy response by applying the π^0 mass constraint on pairs of well-separated photon showers:

$$m^2 = 2E_1E_2(1 - cos\theta) \tag{4.1}$$

where for every pair E_1 and E_2 are the true photon energies and θ is the angle between the photons.

This can be applied throughout almost the entire energy range from 20 MeV up to near 1 GeV. At the higher energies there is overlap with the radiative Bhabha calibration method. Conveniently this is also the point where the error on the angular separation of the two photons from the π^0 decay is no longer negligible. Eventually the two photon clusters merge for π^0's greater than 2 GeV.

The main difficulty with the calibration using neutral pions is that at low energies the backgrounds are very high. There are three sources of low energy π^0 background:

1. Combinatorial—two real photons from different π^0's.
2. "Neutral" clusters due to hadronic interactions in the calorimeter.
3. Beam related backgrounds.

The dominant background below 20 MeV is beam related. From the CLEO and Crystal Barrel experiments it is expected that it will not be possible to extract single-crystal information on

a time scale short enough to be useful. However, it should be possible to calibrate individual crystal rings. The neutral pion calibration is helped considerably by the source calibration as it provides a very precise anchor point at 6.1 MeV. The energy region calibrated by the π^0's lies midway between the source calibration and Bhabha calibration on a ln E scale. The Bhabha calibration is also useful for a fixed point at the upper end of the energy scale.

A similar π^0-based technique was used by CLEO to get a global shower energy correction for the "good barrel" part of their calorimeter. The accuracy that they achieved was 0.5% at 100 MeV and 1% at 25 MeV [47]. Crystal Barrel used π^0's to derive single crystal calibration constants to 0.5% precision, but this is averaged over the entire photon energy spectrum. They used around one million all-neutral events, each containing around three π^0's to calibrate 1380 crystals.

4.13 Minimum ionising particles

The QED process $e^+e^- \rightarrow \mu^+\mu^-$ produces high momenta muons which can be used for calibration purposes. In addition, in the cosmic ray commissioning data there is an abundance of high momenta muons. These high momenta muons only leave ionisation energy in the crystals. This produces a Landau energy distribution which has a well-defined peak near 200 MeV. This is used to provide a single crystal calibration peak. This is complementary to other calibration techniques and is interesting because the energy-deposition mechanism is different from other physics events. Therefore it provides another means to check out the calorimeter. This was used particularly in the early stages of the calibration. The minimum ionising particle (MIP) calibration is carried out in two separate ways, with and without tracks [72]. The calibration with tracks uses the information coming from the drift chamber, that is the track direction and momentum. For the hypothesis of a minimum ionising particle the track parameters are extrapolated into the calorimeter to predict the expected energy deposited in the crystals.

The calibration without tracks selects two calorimetric depositions back-to-back and calibrates the deposited energy in the calorimeter by comparing it to an average value derived from Monte-Carlo study. This calibration method gives a better performance and smaller systematic error with respect to the previous method. Using the back-to-back symmetry, it is possible to apply a strict selection and reduce more the contributions from the electronic noise.

The goal of the calibration is to compute the scaling factor that needs to be applied to the single crystal deposited energy in order to measure the predicted energy. There are several sources of systematic error: the fact that all the particles are not necessarily minimum-ionising, track extrapolation errors, knowledge of dE/dx in CsI(Tl), knowledge of materials in the calorimeter *etc.* An improvement from about 15% to 13% in the energy resolution crystal-by-crystal was achieved in this way.

4.14 Current status of the BaBar calibration

The first sets of calibration constants were obtained by using the abundance of minimum ionising muons from the cosmic ray commissioning run. Both of the methods of doing this calibration, with and without tracks, were used. As mentioned previously the method without tracks led to less systematic error and priority was given to the constants obtained using this method. However, for many of the crystals there was not sufficient data. The statistics were good for the top and bottom of the barrel calorimeter, but not so good for the sides of the barrel and the endcap. For the crystals where the muon calibration was not possible calibration constants were obtained from crystal quality control (QC) measurements of the light yield. This corresponded to approximately one third of the crystals.

The MIP calibration constants and QC corrections were used until the first set of Bhabha constants were measured which gave better accuracy. These were applied on the 6th August. At this point the calorimeter crystal energy threshold was reduced from 5 MeV to 2.5 MeV and new linearity measurements were made. For some crystals the MIP/QC constants were kept due to Bhabha constants not being obtained from them yet.

The Bhabha calibration was carried out in several ways. One method used the expected energy from Monte Carlo in the crystal which the electron enters *i.e.*. the crystal with the highest energy. They are not based on energy sharing between rings. This yields constants for all the crystals except for the innermost ring of the endcap where there is more dead material and no direct flight to the crystals. The other approaches used neighbouring crystal methods which required well defined e^+e^- coincidences. These methods therefore do not obtain constants for the seven most backward rings of the barrel calorimeter and the innermost four rings of the endcap.

The range over which calibration is possible also depends on the acceptance of the L3 trigger. As yet there is no L3 accept for radiative Bhabhas—only an offline filter. Most radiative Bhabha events are getting through on the physics lines, but it is planned to introduce a dedicated L3 radiative Bhabha accept line in the near future. No calibration has yet been done with radiative Bhabha events. From first indications it is likely to require at least one month of data with stable conditions between each calibration. To calibrate individual rings is estimated to take several months data.

In October, single crystal constants for all crystals were obtained from the radioactive source calibration. These were added to the front end look up tables. The source calibration needs to get the noise level in the calorimeter down to 300 keV. Therefore it has to use its own special version of digital filtering. Due to the large beam related backgrounds in the calorimeter a digital filter has not been necessary so far and a simple peak fitting method has be applied to the e^+e^- collision data. This means that the noise level observed during data taking is different from that of the radioactive source. Currently, the incoherent noise in the calorimeter is 180 keV, with some coherent noise surviving digital filtering increasing the overall noise to 300 keV. These numbers are for a radioactive source calibration only.

The π^0 calibration has so far only been applied to photons above 100 MeV. The π^0 calibration is a function of E and theta, but it is not done at the level of individual theta rings (yet). The shower energy calibration at low energy mostly corrects for material in front of and between the crystals. This is a rather smooth function of theta.

Light pulser runs have been used throughout the summer to debug problems and were taken regularly during each calorimeter expert shift. Initially this was three runs per shift and then later this was cut down to one run per day. The light pulser runs are usually taken with beam off as there appears to be noise induced in the reference system when the beams are on. The light pulser has not been used to interpolate between calibrations yet because the stability was not good enough to achieve this and this level of accuracy in the calorimeter was not needed.

Single crystal constants were also applied in the Online Prompt Reconstruction. This allowed data that was taken before the constants were obtained but which had not been reconstructed to be processed with the correct calibration in place.

Prior to the October 1999 shutdown there were large non-linearities in the last two CARE ranges which were not properly accounted for in the online gain corrections. These non-linearities have been significantly reduced during the shutdown but require more work to remove completely. There is now a 1 MeV cut on each single crystal implemented online. This contrasts with the TDR cut of 0.5 MeV and is mitigated by the noise problems described above. Prior to the October shutdown the digicut was at 2.5 MeV. The effect is to truncate the edge of the shower causing an effective leakage. It causes a degradation of energy resolution and systematic offset of the energy scale particularly at low energies. For example the π^0 mass is shifted from 135 MeV to 120 MeV with a 5 MeV digicut. It is corrected for in the shower energy calibrations.

Currently there is an overall scale factor of 10% between the source calibration constants and the constants obtained from the Bhabha calibration. These two calibration points fix the upper and lower ends of the full energy scale. The difference in the low energy and high energy intercrystal calibration is larger than expected. This difference is calibrated out but may be indicative of residual problems in either the source, bhabha, or electronics calibrations that will degrade performance.

4.15 Chapter summary

The calibration has been changing constantly and work has been ongoing throughout the summer. What we have considered so far are the main design considerations of the calibration and monitoring. I have also tried to give a quick snapshot of the current situation and the developments over the summer. In the next chapter I will discuss in detail the design of the light pulser calibration system. In the chapter following this I will present initial data analysis from the system. Finally in the last chapter I will tie this together and show some initial physics results from the calorimeter which demonstrate the status and accuracy of the current calibration.

5

The design of the light pulser system

5.1 Introduction

The light pulser system monitors changes in the response of the *BABAR* calorimeter. Its main task is to check for short term changes in the response of the crystals to an accuracy of better than 0.1%. It provides a useful and flexible diagnostic tool for the entire readout chain of the calorimeter from light collection through to data acquisition. The system is designed to have a stability of 0.5% over a period of around one week. Any changes which occur in the response of the calorimeter over a longer time scale are calibrated using the liquid source system and the other calibration methods mentioned in the previous chapter. However, the light pulser can also monitor long term changes in the calorimeter response to an accuracy of 1% using a reference system which cross-calibrates the intensity of the light pulses against a radioactive source.

This chapter describes the design of the light pulser system starting with an overview and then turning to look at the endcap light pulser system specifically. The differences between the barrel and endcap light pulser system will be discussed. The reasons for the various design choices will be given as much as possible. In the next chapter data analysis from the light pulser system will be presented to demonstrate the performance of the system to date.

5.2 Overview of system

The overall design of the light pulser system is shown in figure 5-1. There are two high stability xenon flash lamps. One of the lamps supplies the barrel and the other supplies the endcap. The light produced from the xenon lamps is spectrally filtered to match the emission spectrum of CsI scintillation light. It is then attenuated by two neutral density filters to allow the correct equivalent energy in the calorimeter crystals to be selected. The light fills a light mixer which uniformly illuminates a bundle of 400 μm multi-mode fibres. These fibres deliver the light to individual calorimeter modules. At each module there is a module mixer which uses the light from a 400 μm fibre to illuminate a close-packed bundle of 200 μm fibres. Each of the 200 μm fibres then transports light to individual CsI crystals. The light is injected into the rear face of each crystal and then diffusely reflects within the crystal. This effectively imitates the scintillation light that is produced in a crystal by the energy deposition of an electromagnetic shower. The light is then readout using the full *BABAR* calorimeter electronic readout chain from the photodiodes right through to the data acquistion. The light pulser

system produces a high enough equivalent energy in the calorimeter to allow it to be run with beam backgrounds in the detector.

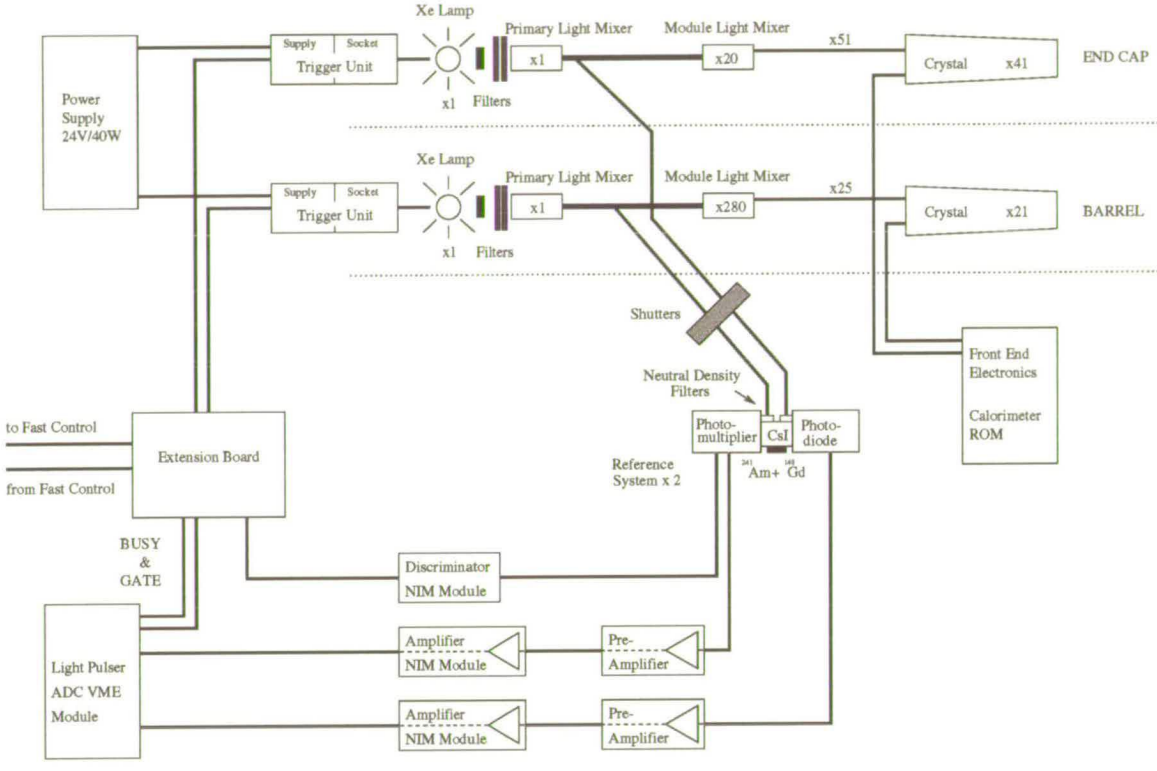

Figure 5-1. *Overview of the light pulser system*

A reference system is required to take out any pulse-to-pulse instabilities in the intensity of the light emitted. This is done by routing fibres from the barrel and endcap primary mixer systems to a reference system. The reference system itself is cross-calibrated against a mixed alpha source. Both the alpha source and the reference fibres are attached to a small CsI crystal. This crystal is readout by a photomultiplier tube and a photodiode. The reference system data from both source events and light pulses is collected in the multi-event buffer of a peak sensing ADC. The source events are accumulated continuously in the buffer and readout using a 1 Hz software trigger.

The readout of light pulser system events is triggered from a signal which is derived from the photomultiplier tube in the reference system. This is more accurate than using the input signal to the lamp trigger power supply because there is a time jitter of 200 ns in the lamp response with respect to the trigger. The lamps are triggered at a frequency of 14.2 Hz which comes from dividing the *BABAR* clock.

5.3 The light source

5.3.1 Design requirements

When considering which light source was to be used by the BABAR light pulser system there were three deciding factors which were to be taken into account. Firstly, the lamps should be as stable as possible. The reference system coupled to the primary light mixers will take out pulse-to-pulse instabilities, but it is still highly desirable that the lamps are stable on short-term and long-term time scales. The second factor taken into account was the intensity of the light that is produced. There are a large number of crystals in the BABAR calorimeter and the intensity of the light delivered to each crystal must have an equivalent energy of around 10 GeV. The third factor was the timing distribution of the pulses. This must be similar to that of a CsI scintillation pulse. If the pulse timing is significantly different then it would require a different digital filtering with a different set of weights and depth of sample in the calorimeter readout modules.

The lamp chosen in the final design is manufactured by Hamamatsu type L4633. Xenon flash lamps produce a high-intensity spectrum which covers a broad range of light from the ultraviolet to infrared range. We use spectral filters to select the correct wavelength range corresponding to the emission spectrum of CsI scintillation light. The Hamamatsu lamps are manufactured primarily for photometric applications and feature a high stability of less than 1% between flashes. The pulse rise time is fast (400 ns) and the timing distribution matches well that of a CsI pulse. The lamps can be driven at a trigger rate of up to 100 Hz and their lifetime is guaranteed to be greater than 10^9 pulses. Other lamps were studied [73], but were not suitable because of lack of stability, intensity, or the correct timing distribution.

5.3.2 Timing distribution

As mentioned previously the timing distribution of the xenon light pulse must be close to that of a CsI scintillation pulse so that the same digital filtering can be used for light pulser events, as for physics events. The timing parameters for a typical CsI scintillation pulse are given in table 5-1 and compared to those measured for various types of xenon flash lamps.

Table 5-1. *Comparison of the timing distribution for different lamps*

Light Source	Rise Time / ns	Fall Time / μs	Pulse length / μs	E_{flash} / J
CsI	50	2.5	2.6	—
L4633 (Hamamatsu)	400	2.0	2.8	0.15
PX-1 (WPI)	900	3.0	5.0	0.25
FXE5U (Oriel)	800	5.0	6.4	1.00
CGS 0703 (EG&G)	7000	25.0	38.0	0.54

The rise time of the CsI scintillation pulse is very fast and only the Hamamatsu lamp comes close to matching this. The other lamps have rise times which are too long. The CsI pulse has a longer fall time however and most of the lamps do match this fairly well. These measurements are neglecting the 250 ns shaping time of the *BABAR* calorimeter preamplifiers which result in the CsI scintillation pulse having a rise time of 0.9 μs and a fall time of 7 μs. This also affects the lamp pulses and the Hamamatsu L4633 lamp has a rise time of 1 μs and fall time of 8 μs when the preamps are considered. This is clearly a good match allowing the same digital filtering to be used. Given these qualities the L4633 lamp was chosen over the other lamps.

5.3.3 Hamamatsu flash lamps

Each lamp (figure 5-2) contains an anode, cathode, trigger probe, and sparker housed in a cylindrical glass bulb filled with high-purity xenon gas at a pressure of several thousand pascals. The L4633 lamp has the additional feature of having a built in rear reflector. Borosilicate glass was chosed as the window material as UV wavelengths are not required.

The trigger probes are the electrodes which are used for a preliminary discharge. They stabilize and control the main xenon discharge. Each electrode is needle-shaped to concentrate the electric field at the tip. The number of trigger electrodes required to control the discharge depends on the arc size. If the arc size is 1.5 mm only one trigger probe is required.

The anode and cathode are high performance barium impregnated electrodes which feature high electron emissivity, low operating temperature and high resistance to ion impact. They are conical in shape to gather the electric field at the tip and again to stabilize the discharge. Thus they are very similar in shape to the trigger probes, but are much larger in diameter.

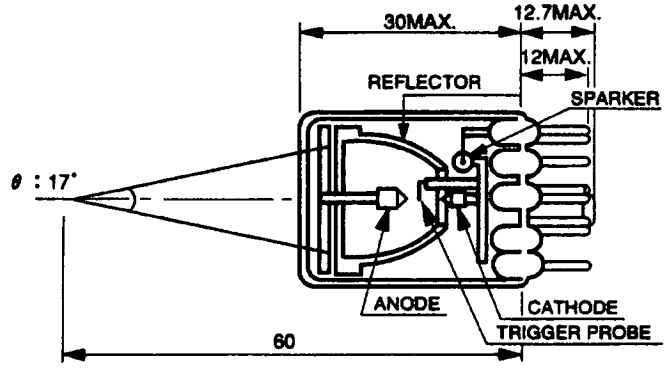

Figure 5-2. *Drawing of the Hamamatsu L4633 lamp*

The function of the sparker electrode is to ensure stabilization of the xenon discharge. When a trigger voltage is applied, the sparker begins to discharge and UV light is emitted. This UV light induces each cathode to emit photoelectrons, which then ionize the xenon gas.

To produce the xenon discharge the high voltage of 700-1000 Vdc is applied across the 1.5 mm gap between the anode and cathode. When a trigger is received the charge on the trigger capacitor is released and is fed to the trigger transformer which generates the high voltage pulse. This pulse is sent to the sparker, trigger probe and anode. First the sparker discharges then there is the discharge between the cathode and trigger probe. This preliminary discharge stabilizes and controls the main discharge. It causes the main discharge arc to occur along the path of the preliminary discharge.

5.3.4 Different models of the Hamamatsu lamp

Three different Hamamatsu lamps were considered as possible light sources. Their different characteristics are outlined below:

L2437 This lamp was used very successfully by the light pulser system which was designed and built for the L3 experiment [74]. The source of light from this lamp is direct as it has no rear reflector. Therefore only the forward component of light would be fed into the light mixer and the rest would be lost. The discharge arc is produced using one trigger electrode. The arc size is 1.5 mm and it is perpendicular to the optical axis.

L2189 This lamp was used by the Crystal Barrel experiment [48]. The source of light from this lamp is also direct and it does not have a rear reflector. The discharge arc is parallel to the optical axis. The discharge is triggered by 5 electrodes over an arc length of 8 mm. The larger arc results in a greater intensity, but a much slower timing distribution.

L4633 This is the lamp which was chosen in the final design. It has a built in rear reflector resulting in more efficient use of the light that is produced. The light emitted backwards and to the sides is redirected to reinforce the forward going component. The arc size is 1.5 mm and the discharge is triggered by one electrode. The arc is parallel to the optical axis. The full specifications of the lamp are given in table 5.3.4.

5.3.5 Stability and intensity

The absolute intensity of the discharge can be unstable due to two things. The trigger electronics must be carefully designed so that the charging resistor in the trigger circuit is large enough so that when the trigger signal is received the trigger capacitor is fully charged therefore avoiding any fluctuation of the input charge that is given to the trigger transformer.

There is an inherent pulse-to-pulse instability in the lamps which cannot be avoided. The total amount of light varies in time due to fluctuations in the basic plasma properties that are involved in the xenon gas discharge. This is due to the geometry of the high voltage

Table 5-2. *Specifications of the Hamamatsu L4633 xenon flash lamp*

Parameter	Specification value
Arc Size / mm	1.5
Bulb Shape	Converging
Window material	Borosilicate-1
Spectral Distribution / nm	240 – 2000
Supply voltage / V_{dc}	700 – 1000
Trigger voltage / kV	5 – 7
Max. average continuous power / W	15
Max. average energy per pulse / J	0.15
Maximum repetition frequency / Hz	100
Time jitter / ns	200
Lifetime / pulses	10^9

discharge. The path and length of the arc will vary slightly on a pulse-to-pulse basis. The intensity of light given out is inversely proportional to the size of the discharge arc. However, this instability can be greatly reduced by the use of a primary mixer system which we will discuss later.

Table 5-3. *The intensity and stability of the Hamamatsu lamps*

Lamp	Mean / ADC units	Sigma
L2437	155	0.90%
L2189	510	0.25%
L4633	680	0.40%

Measurements taken from the three different types of Hamamatsu lamps are given in table 5-3. The instability of the L2437 lamp is most likely due to the fact that the arc is perpendicular to the optical axis. The lamp has a small arc size and no rear reflector and therefore has the lowest mean intensity of the three lamps. The second lamp has a large arc size 8 mm and produces four times as much light. It is also reasonably stable on a pulse-to-pulse to basis, although the arc is particularly big. It is likely that this is due to the fact that there are the five trigger electrodes controlling the arc geometry. In addition, the arc and optical axis are collinear. Therefore changes in the path of the arc will have a lesser effect on the intensity of light that is emitted in the forward direction. The third lamp had the highest intensity of all. This is due to the rear reflector. It has a better stability than the L2437 lamp. This is again helped by the fact that the arc is parallel to the optical axis, but not completely because the sideways and rear components of the light are also used. The anode actually blocks the most forward component of the light.

5.4 Spectral filters

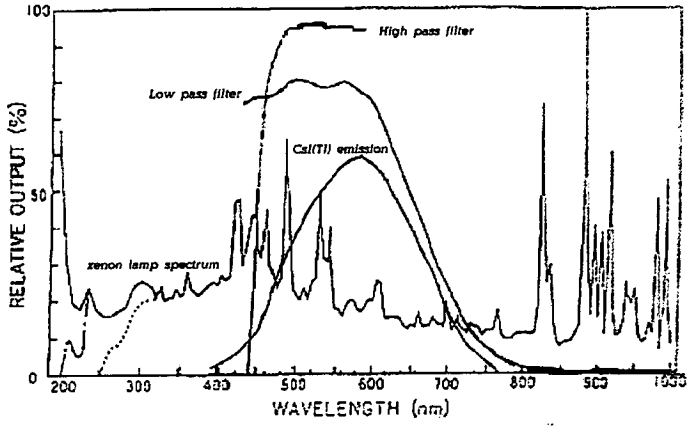

Figure 5-3. *The spectra of xenon light along with that of CsI(Tl) scintillation light with the low and high pass filter cut-off points superimposed*

The wavelength of the xenon light must be carefully filtered to match that of the CsI scintillation light. This is particularly important because the light pulser is monitoring the light transmission properties of the CsI crystal and these may change with wavelength. Two spectral filters are used. The high pass filter removes wavelengths below 400 nm (Oriel - 455FG03). The low pass filter (Oriel - 775FW82) removes wavelengths above 750 nm. Figure 5-3 shows the typical spectrum of Cs(Tl) scintillation light superimposed on the specifications given by Hamamatsu and Oriel. Figure 5-4 show results for the measured spectra with and without filters using a computer controlled spectrometer. It is clear that the filters select the correct wavelength band of the xenon light. From this plot it was also clear that the low pass filter is not as crucial as the high pass filter, though still desirable.

5.5 Neutral density filters

Table 5-4. *The filter wheel settings verus the respective attenuations*

Setting (wheel 1)	A	B	C	D	E
Filter Attenuation / $OD_{nominal}$	Empty	2.00	0.05	0.80	3.00
Setting (wheel 2)	1	2	3	4	5
Filter Attenuation/ $OD_{nominal}$	Empty	0.60	0.40	0.20	1.00

The light pulser system has a dynamical range of equivalent energies from 1 MeV to 10 GeV. This is achieved by using different neutral density glass filters manufactured by Newport (FS-3) to attenuate the light. These are housed on two separate filter wheels which can

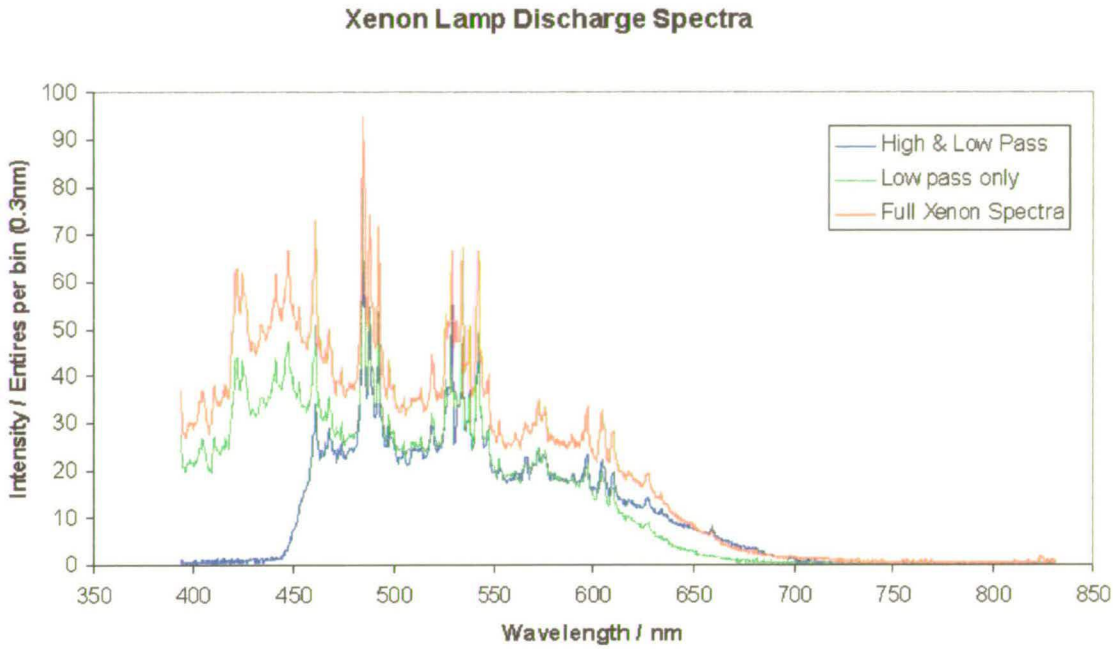

Figure 5-4. *Measured spectra of the xenon light demonstrating the effect of the filters*

be rotated to select the desired light intensity. There are five settings of each filter wheel corresponding to four filters and one blank slot which allows the full intensity of the lamp to be transmitted. Therefore there are 25 possible settings to cover the required energy range uniformly. Table 5-4 shows the various filter wheel settings and the filter specifications given by Newport. The attenuation specifications given are in terms of the optical density at a wavelength of 650 nm. Optical density (OD) is related to transmission (T) and attenuation (A) by equation 5.1

$$\mathrm{OD} = -\log_{10}(\mathrm{T}) = \log_{10}(\mathrm{A}) \tag{5.1}$$

Studies of the neutral density filters were undertaken [73, 75] and the filter attenuations were measured for the xenon light with the spectral filters in place. Table 5-5 shows all of the 25 filter wheel settings and the combined attenuation given by the filters. The equivalent energy is also given assuming that the highest energy is 10 GeV.

5.6 The primary mixer

The objective of the primary mixers is to take the filtered light from the lamps and mix up all the optical modes taking out any geometrical distributions in the light intensity coming from the lamps. This is essential to allow the light to be injected uniformly into the primary fibres. They are one of the most important parts of the light pulser system because if they do not mix

Table 5-5. *The attenuation and equivalent energy for each of the combined filter wheel settings assuming a maximum energy of 10 GeV*

Combination	$OD_{measured}$	Energy / MeV	Combination	$OD_{measured}$	Energy / MeV
A1	0.00	10000	D2	1.43	375
C1	0.03	9300	D5	1.70	200
A4	0.22	6000	B1	1.75	178
C4	0.25	5600	B4	1.97	107
A3	0.40	4000	B3	2.15	71
C3	0.43	3700	E1	2.32	48
A2	0.60	2500	B2	2.35	45
C2	0.63	2300	E4	2.54	29
D1	0.83	1500	B5	2.62	24
A5	0.87	1300	E3	2.72	19
C5	0.90	1200	E2	2.92	12
D4	1.05	891	E5	3.19	6.5
D3	1.23	589			

the light sufficiently then the reference system will not work. This is because the reference system fibres can only sample a small region of the mixer surface. If this is not uniform on a pulse to pulse basis or a long term basis then the reference system will be unable to correct for pulse-to-pulse changes in intensity or for long term drifts in the system.

The position of the diffuser is important. It can either be placed between the lamp and filters, or between the filters and the mixer bar. The most effective position of the diffuser disk was found to be immediately in front of the mixer bar which also takes out any nonuniformities in the transmission of the filters which could be allowed for, but would require that each of the filter wheel positions be exactly reproducible. Since the light is scattered to wide angles by the diffuser it is desirable for the diffusers to be as close as possible to the mixer bar. The best results for uniformity and good intensity at the output end of the mixer bars was obtained by roughening the entrance end of the plexiglass mixer bar. This resulted in good diffuse scattering of the light whilst maximising the quantity of scattered light reaching the mixer bar.

The first part of the manufacture of the primary mixer bars was the choice of material. Materials which are readily available and exibit the best transmission in the wavelength range of CsI scintillation light are glass, quartz, and transparent plastics. Plexiglass, also known as perspex, was found to give the best intensity and is easily machinable.

The cross section of the mixer bars depends largely on the geometry of primary fibre bundles which will be discussed in the next section. The bars were chosen to have a square cross-section 30 mm × 30 mm for both the barrel and the endcap. Mixer bars with circular cross-sections were found to have a poor uniformity in the intensity profile at the output end of the bar. Mixer bars of square cross-section have less symmetry and feature better mixing. The

mixers bars are 300 mm long. The length of the mixer bar determines the homogeneity of the intensity profile of the end of the mixer bar. The total intensity will also decrease with length due to losses in the reflections and transmission.

5.7 Input to the primary fibres

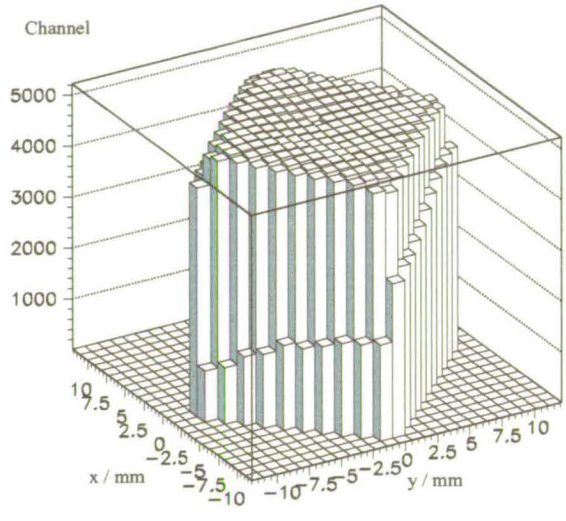

Figure 5-5. *The light intensity profile across the output end of a* 15 × 15 mm *mixer bar.*

The primary mixer bars produce a large area uniform light source which is coupled into the primary fibres which transport the light to the barrel and endcap modules. The primary bundles for the barrel light pulser system are substantially different to those in the endcap system. The endcap system will be discussed from here on. The differences specific to the barrel light pulser system will be discussed in section 5.11.

An important feature of multimode fibres is the variety of different angles of light which may be coupled into the fibres. To maximise their light transmission all of the modes in the fibre should be filled with light. The primary mixer bar should output light through a variety of angles. However, it was found that the light was more intense in the direction parallel to the mixer bar [75]. Therefore to ensure that the primary fibre optics were filled properly, microlenses were used to couple the light into the primary fibres.

5.7.1 The graded index microlenses

Microlenses are essentially short segments of large diameter graded index optical fibre. Conventional fibre optics rely upon having a step refractive index where the fibre core is

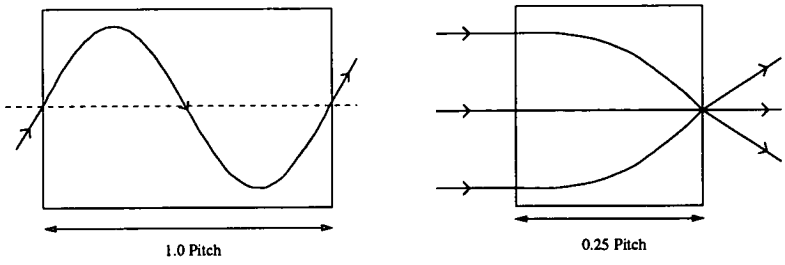

Figure 5-6. *The principle of the microlens*

at a higher refractive index than the cladding. Graded index fibre optics however do not have a separate core and cladding. Instead they have a refractive index that varies radially. This results in an optical ray following a sinusoidal path down the fibre rather than discrete total internal reflections, see figure 5-6. An interesting feature of these fibres is, if they are cut at specific lengths, they act as minature lenses. If an optical ray completes one sinusoidal oscillation within the lens it is said to have a pitch of 1.0. For our case lenses with a pitch of 0.25 allow a collimated light source to be focused. This is ideal for input into a fibre optic. Each lens is coated in an anti-reflection coating (MgF_2) to maximise its transmission. The type of lens which was chosen was plano-plano meaning that the lens is terminated perpendicularly at both ends.

Table 5-6. *Properties of the microlenses (Newport type LGI630-3)*

Property	Specification value
Pitch	0.25
Numerical Aperture	0.46
Diameter / mm	1.8
Length / mm	4.63
Clear Aperture / %	70

5.7.2 The primary bundle design

There are 25 primary fibres required for the endcap light pulser system. This is one fibre for each calorimeter module, two spare fibres, and three fibres for the reference system. The fibre and microlenses are mounted within a glass fibre composite block shown in figure 5-7. This has a square cross-section, 15 × 15 mm, to exactly match the light mixer bar (the bar cross-section was later increased to 30 × 30 mm). The microlenses are glued into the block in a 5 × 5 square array. Each of the primary fibres is stripped, glued, and polished into separate brass ferrules shown in figure 5-8. For the microlenses to function properly it is vital that the polished input surface of the primary fibre is positioned correctly so that it coincides with the focal point of the microlens. The ferrules allow the fibres to be centred and aligned properly.

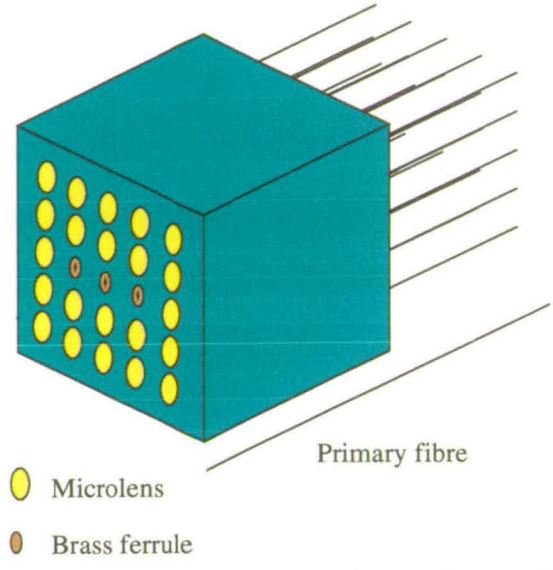

Figure 5-7. *The arrangement of microlenses and fibre holding ferrules in the primary fibre bundle*

In addition each ferrule is polished so that the fibre end is exactly flat and perpendicular where is comes into contact with the lens. The ferrules have a shoulder to prevent them from being pushed too far in which could damage the lens and its glue joint. The protective jacket of the fibre is glued directly into the back of the ferrule to ensure that is it always fully protected. The three fibres which are used for the reference system are not equipped with microlenses for consistency with the barrel light pulser system which does not have microlenses.

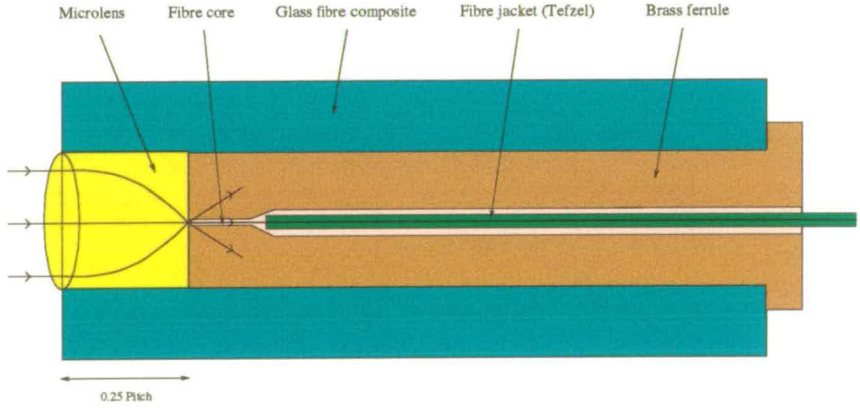

Figure 5-8. *The coupling of the primary fibres to the microlenses*

5.8 The primary fibres and their routing

The primary fibres must have good uniformity in the wavelength range 400-800 nm, be radiation hard, plenum rated, and have a small bending radius. The fibres chosen were TECS fibres (FT-400-EMT) which are manufactured by 3M. The specifications of the fibres are given in table 5-7

Parameter	Specification
Core diameter / μm	400±8
Cladding diameter / μm	430^{+05}_{-15}
Jacket diameter / μm	730±30
Numerical aperture	0.39
Bending radius (short term) / mm	20
Bending radius (long term) / mm	27
Acceptance angle	46°
Operating temperature	-65 to 125°C

Table 5-7. *The primary fibre specifications*

The fibres are enclosed in an additional protective jacket making them around 2mm thick. Where the fibres reach the outside of the primary mixer housing they are grouped into two sub-bundles of 11 fibres which are surrounded by a reinforced flexible plastic conduit which is plenum rated. At this point there is a strain relief shown in figure 5-9 which is firmly clamped at the point where the conduits exit the lamp and mixer housing. The three reference fibres are separate from the bundle here and routed to the reference systems.

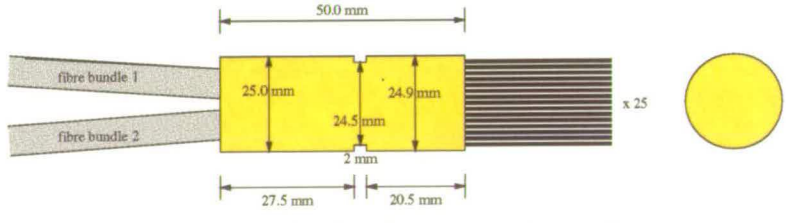

Figure 5-9. *Strain relief for the primary fibres*

The two sub bundles are then routed along the cable tray lying below the light pulser rack. One goes over the magnet, then down and forward to the entrance slot to the endcap at 8 o'clock. The other fibres go down and forward to the four o'clock position. As shown in figure 5-10 each conduit goes to a break out point where there is a second strain relief which is similar to the first, but with smaller diameter. Each of the primary fibres is then routed around the inner cone of the endcap to its entrance position to the module mixers.

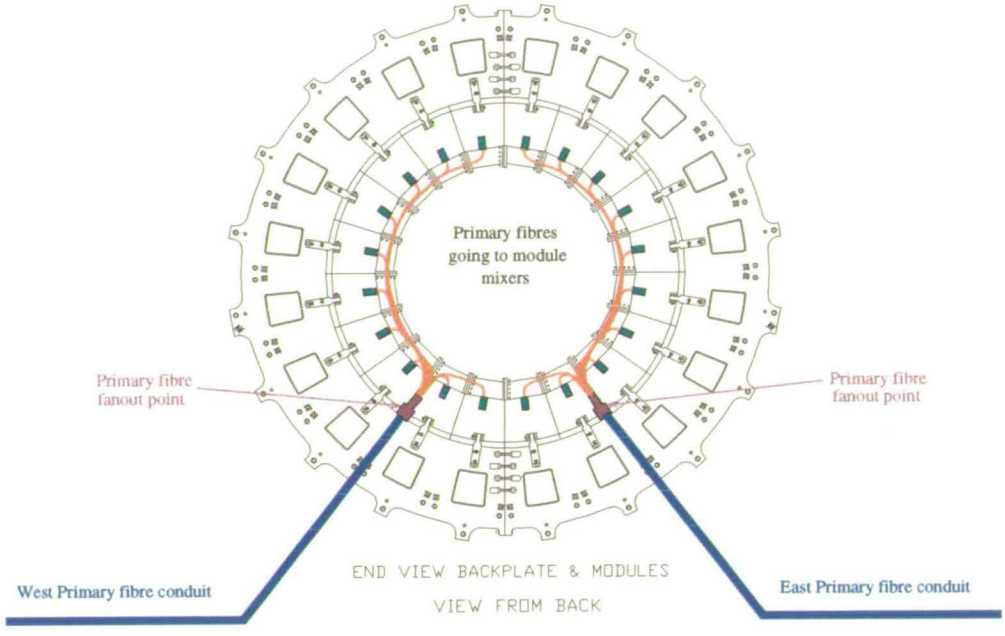

Figure 5-10. *The routing for the endcap primary fibres*

5.8.1 The module mixer

The module mixers distribute the light, as uniformly as possible, from each primary fibre into a bundle of module fibres. The module fibres transport the light to the individual crystals. The input side of the mixer consists of the 400 μm primary fibre which is glued and polished into an SMA 905 connector. The output side consists of the 51 modules fibres close-packed in a bundle which also fits inside a specially drilled SMA interconnect. The light from the primary fibre is coupled to the bundle of fibres via a 4 mm airgap. The airgap is large enough to allow the bundle to be uniformly illuminated, but small enough to avoid introducing a large attenuation. The microlenses play an important rôle in this because they allow the light modes of the primary fibres to be correctly filled at the input end thus ensuring that the maximum possible numerical aperture of the primary fibre is used at the output end. The module mixer is embedded within the aluminium flange of the end cap module. These flanges make up the inner edge of the endcap and they give mechanical and thermal stability to the optical coupling.

5.9 The module fibres and their routing

The module fibres are 200 μm hard clad silica fibres. They are manufactured by CeramOptec (type HUV 200T). The 51 fibres are grouped into two sub bundles which run up either side

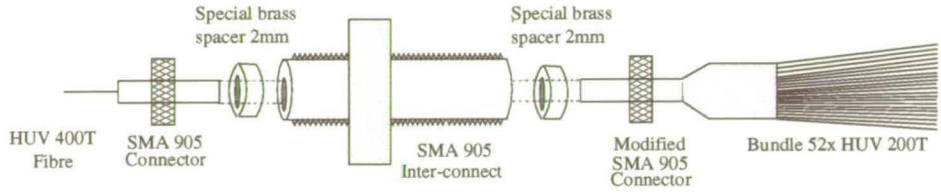

Figure 5-11. *The module light mixer*

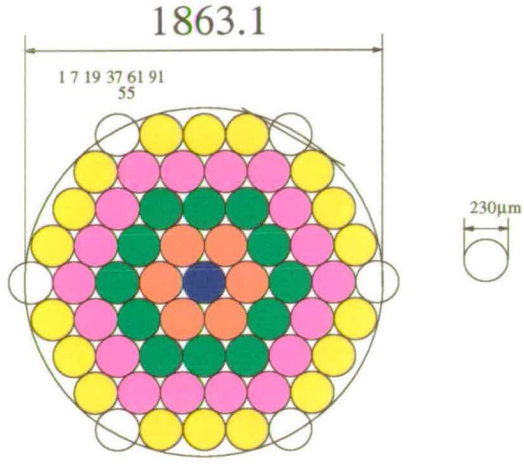

Figure 5-12. *The design of the hexagonally close packed module bundles*

Parameter	Specification
Core diameter / μm	200±4
Cladding diameter / μm	230±4.6
Jacket diameter / μm	500±25
Numerical aperture	0.37
Bending radius (long term) / mm	20
Acceptance angle	43.4°
Operating temperature	-40 to 150°C

of the calorimeter module. When the fibres reach their ring of crystals they run along the ring until they reach the correct crystal where they are attached. The details of the fibre attachment will be explained in the next section however the point to be noted is that the attachment requires that the fibres undergo a bend of radius 7 mm. This is well outside the specifications and needed to be tested, see figure 5-15.

The 200 μm fibres were tested using the set-up that is shown in figure 5-15. The modes of the fibre were filled using a microscope objective lens to couple in the light from a helium neon laser. This light is then readout at the other end of the fibre by a photodiode. The fibre was then adjusted to ever decreasing bending radii over a full 360° until the fibre finally failed.

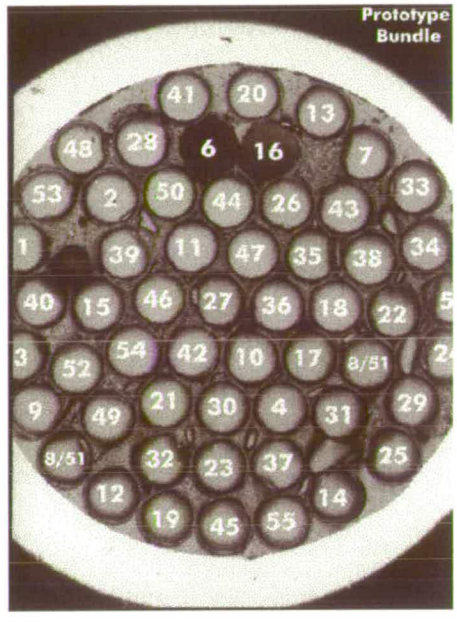

Figure 5-13. *Fibre numbering in bundles*

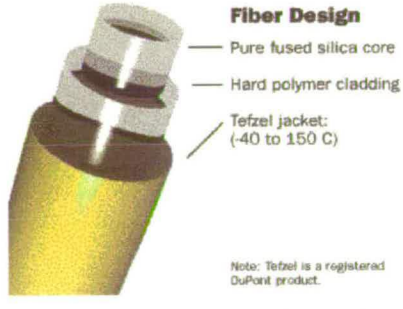

Figure 5-14. *The structure of hard clad silica fibre*

The results are shown in 5-16. This clearly demonstrated that the fibres could withstand small bends on a short term time scale. Later measurements were made in Bergen [76] which also proved the long term stability of the bends.

It is believed that the excellent performance of hard clad silica fibres under severe bends is due to the thinness of the cladding. This results in the lower stress in the material due to the outer and inner circumferences of the bends being closer. The first part of the fibre to break causing light loss is the cladding. These fibres also have a soft Tefzel jacket which protects the cladding from damage.

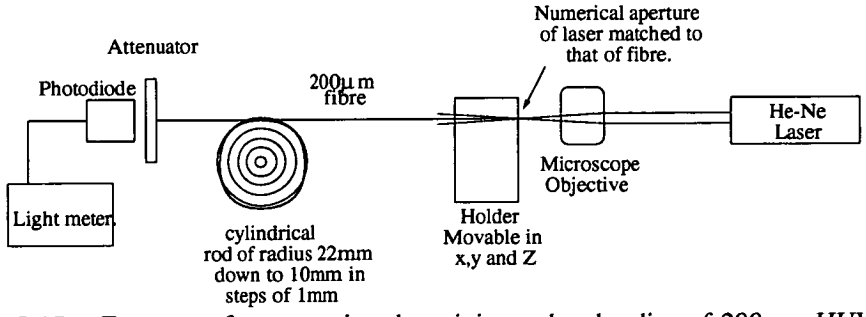

Figure 5-15. *Test setup for measuring the minimum bend radius of 200 μm HUV 200T fibre*

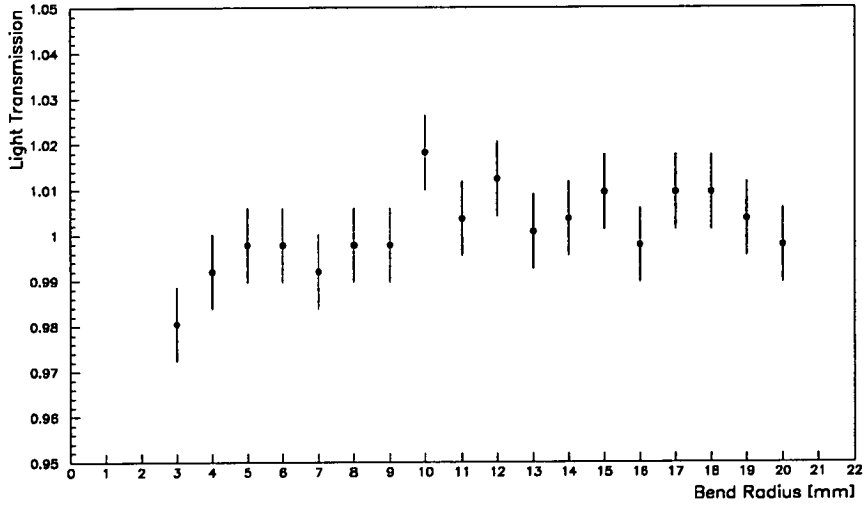

Figure 5-16. *Results from the bend measurements*

5.9.1 The fibre attachment

The attachment of the fibres to the rear face of the CsI crystals was particularly complicated due to various design constraints. The main physical constraint is that the amount of space which was available is particularly small and inaccessible. This made it impossible to use conventional connectors and a special connection method had to be designed. In addition there was a second design constraint which made things even more difficult: the endcap was designed to be disassembled for repairs *e.g.* preamplifier, photodiode and crystal replacement. This meant that it must be possible for all the fibres to be detached from the crystals and removed quickly. This must be done without damage to the fibres, electronics or crystals. Again due to the confined area this was difficult to implement and precluded the use of gluing materials.

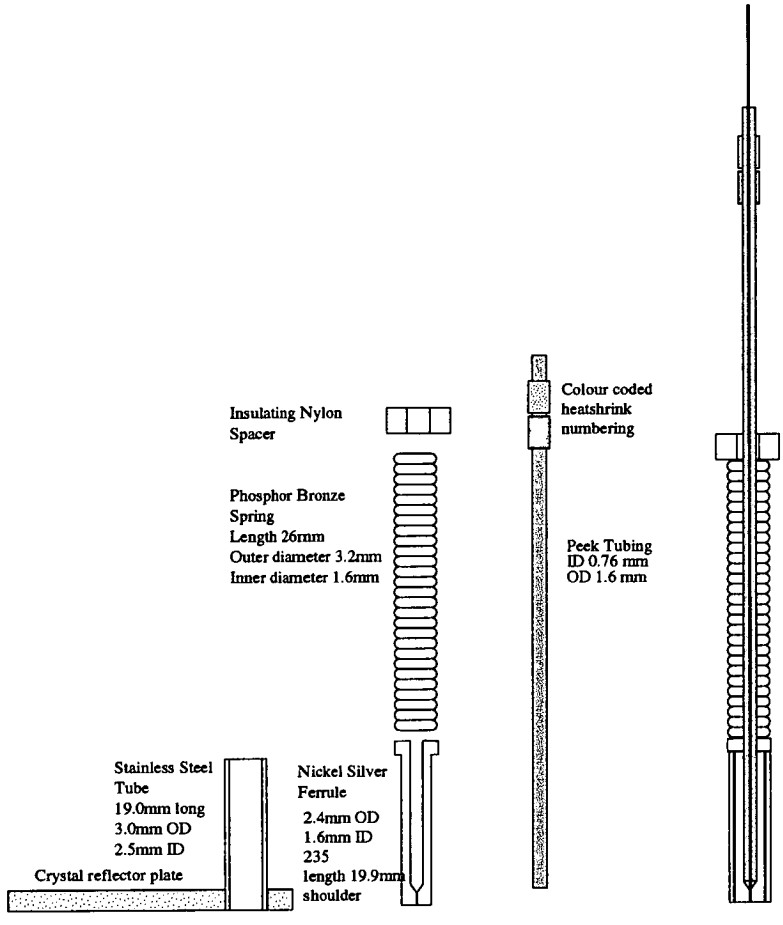

Figure 5-17. *The fibre optic attachment to the crystal*

Due to the routing, the fibres are running parallel to the cooling pipe when they reach each crystal and must undergo a 90° bend to become parallel to the crystal. The space allowed for this necessitates a bend radius of 7 mm. This bend has to be as uniform as possible, well protected and stable. The fibres are first encapsulated in a peek (polyetheretherketone) tubing. This is one of the strongest and most durable plastics available on the market today and is used in industry for chromatography. At the point where the peek tubing is bent there is a tightly wound phosphor bronze spring which helps to maximise the bend radius, makes the bend uniform and protects the tubing from shearing. The height of the crystals relative to the lid of the readout boxes can vary by +0/-5 mm which meant that any protective tubing could not be bent prior to installation. However, the spring is electrically conducting. To prevent all the crystal readout boxes from being electrically connected, via the cooling pipe, a nylon spacer is place between the spring and the cooling pipe. The fibre is terminated in a nickel silver ferrule. This ferrule had a large diameter opening at one end allowing the peek to be glued directly into it and has a 232 μm hole drilled on the other side for the fibre core and cladding (230 μm). This had to be precisely drilled to allow the best possible alignment of the fibre.

Nickel silver was chosen because it polishes well producing very little contamination to the fibre surface (unlike brass), it doesn't tarnish easily and is hard, but still allows the 232 μm hole to be drilled. On the back of each crystal there is a reflector plate which has a hole drilled into it and a stainless steel tube press fitted into it. The ferrule is inserted into this tube and stops at a precise height above the crystal due to the shoulder on the ferrule.

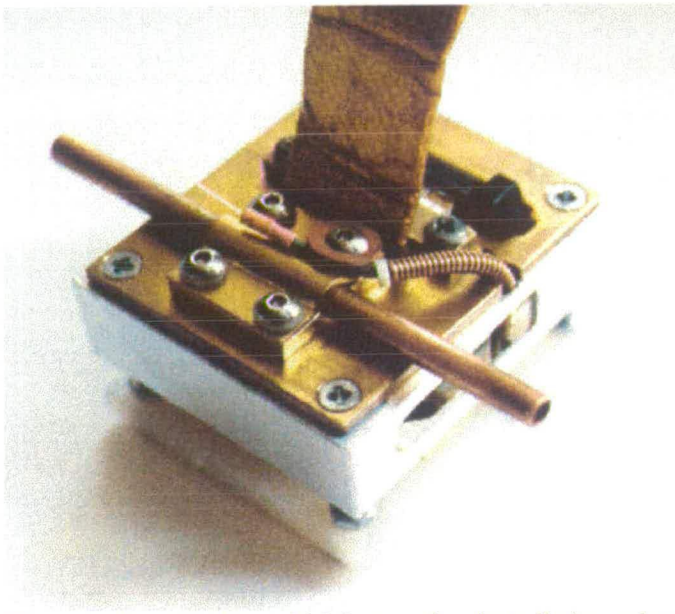

Figure 5-18. *The crystal readout box which houses the photodiodes and preamplifiers. The fibre optic attachment and the cooling pipe are shown.*

5.10 Quality assurance of the endcap fibre optics

To be able to achieve a system which has no faulty channels requires that everything is extensively tested before installation. For the endcap light pulser system a lot of care was taken to ensure that the module bundles are of the best quality possible and error free, since they are inaccessible once the endcap modules are closed and mounted onto the backplate.

For the first five bundles all the single fibre ends were examined under a high power microscope and photographed until we were satisified with the polishing quality coming from Fibertech. Later only the bundle ends were photographed. The transmission of all the fibres was measured using a large area photodiode connected to a EG&G Ortec 570 amplifier. The spectra were then digitised using a Aptec 5000 MCard ADC (12 bits). The lengths of the fibres, their transmissions and their geometrical position within each bundle were all documented and the ADC spectra stored. The fibre bundles were then despatched to the endcap module assembly. After and during assembly they were tested again in Liverpool and Manchester. Later when the modules arrived at SLAC they were opened again and inspected and any faulty fibres were replaced.

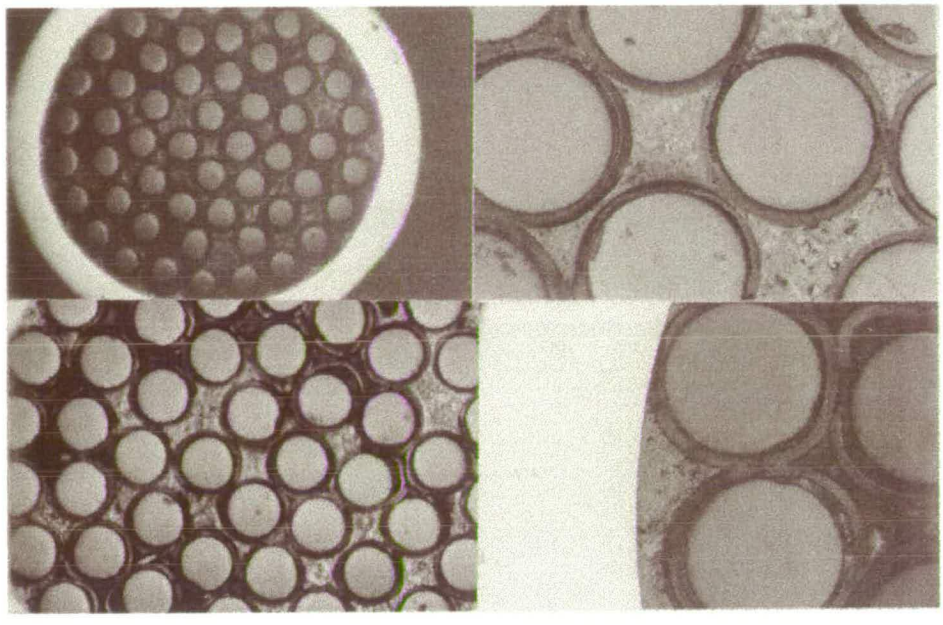

Figure 5-19. *Microscope examination of fibre ends*

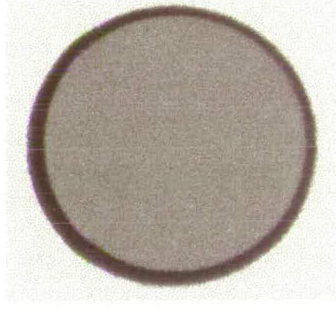

Figure 5-20. *Microscope examination of fibre ends*

5.11 Barrel light pulser system

The barrel light pulser system requires 280 primary fibres and is different from the endcap light pulser system in some respects. Instead of using microlenses to couple the light into the fibres they are packed together in a close packed arrangement in four rectangular sub-bundles and polished. The fibres are stripped down to their cladding and glued together with epoxy. Due to the large number of fibres the length over which they are stripped is much greater than for the endcap fibres to give more room to gradually pack the ends together. In addition the alignment of the four sub bundles to the mixer bar is more difficult compared to the endcap.

The primary fibres from each sub-bundle are routed to the four quadrants of the barrel calorimeter. For the routing they are grouped in bundles of seven inside a strong reinforced

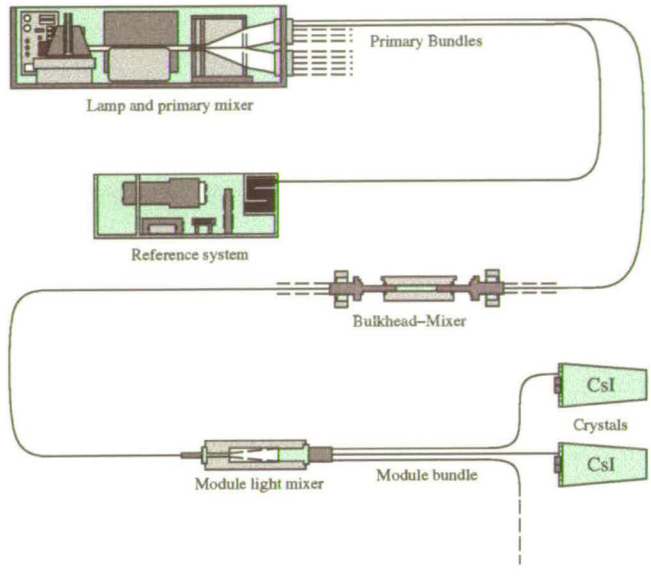

Figure 5-21. *Overview of the barrel light pulser system*

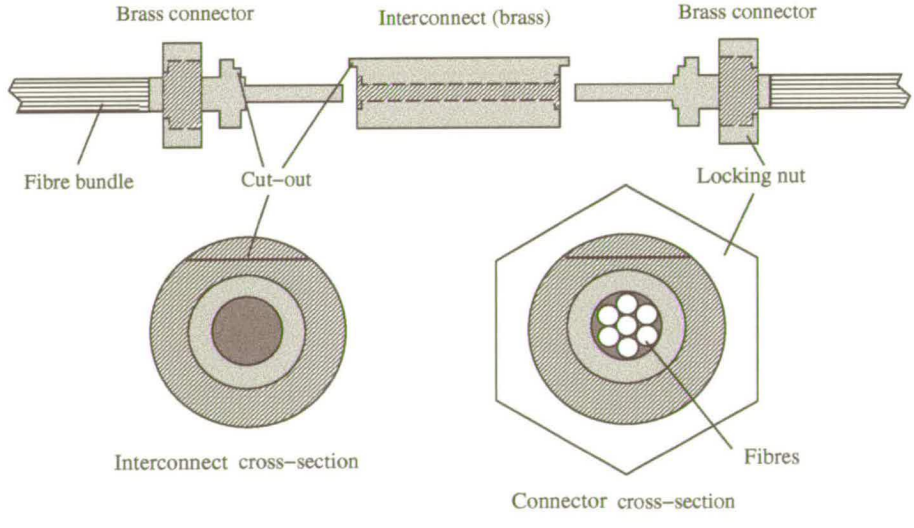

Figure 5-22. *The barrel calorimeter bulkhead connector*

protective buffer and jacket. Each of these cables serves a row of seven calorimeter modules. When the calorimeter was assembled it was necessary to have a break point in the routing. This made it necessary to have a bulkhead interconnection, shown in figure 5-22, at the back-

ward flang e of the calorimeter. Due to the lack of space there was not room for seven separate interconnections. Therefore the bulkhead connector had to be a single specially designed 7–7 connector. Seven fibres are grouped into a hexagonally close-packed arrangement inside the connectors on either side. A matching alignment piece was manufactured into the connector and the interconnect to ensure the correct orientation. The bulkhead connectors themselves are held within brass cups which are mounted in the flange of the calorimeter giving mechanical and thermal stability to the optical coupling.

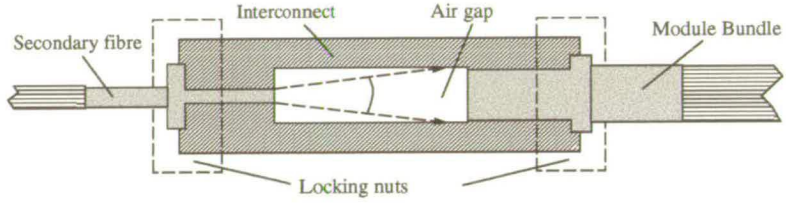

Figure 5-23. *The barrel module mixer*

From the bulkhead connectors secondary fibres are routed to the individual modules, at each of which there is a module mixer, similar in design to the endcap system, shown in figure 5-23. Since there are only 21 crystals in each barrel module, smaller fibre bundles could be used, each having a radius of 1.5 mm. There is a correspondingly smaller air gap in the module mixer of 3.4 mm. One difference between the two systems is that the endcap uses industry standard connectors whereas the barrel used specially made brass connections. The module fibres are routed from the module mixer to the indvidual crystals. They are held in place using glue, since it is not anticipated that the barrel calorimeter will need to be disassembled. A fibre attachment scheme was used where an outer ferrule was attached to the lid of the readout box. This was located in the corner. The module fibres are glued in inner ferrules which are then fed into the outer ferrules to obtain a precise height above the crystals. The length of the barrel ferrules is 35 mm and they have an inner diameter of 800 μm. The air gap between the fibre end and the crystal is 0.5 mm $\pm$ 0.5 mm.

5.12 Reference system

The "monitoring" reference system for the light pulser system is designed to normalize for the inherent pulse-to-pulse instabilities of the xenon flash lamp. These instabilities are mentioned in section 5.3. The components of the reference system are shown in figure 5-25 and the electronics are shown in figure 5-26. One reference fibre from each of the endcap and the barrel primary mixer systems is fed into the reference system box through a chicane, ensuring that the box is light tight. Each of the two fibres is suitably attenuated and the light is injected into a small CsI crystal which is readout by a photomultiplier tube and photodiode. The photodiode has better long term stability, but a lower signal to noise ratio. The photomultiplier tube has better timing resolution and signal, but has long term drift. The output of the preamplifier of the photodiode is connected to two amplifiers with amplification factor control

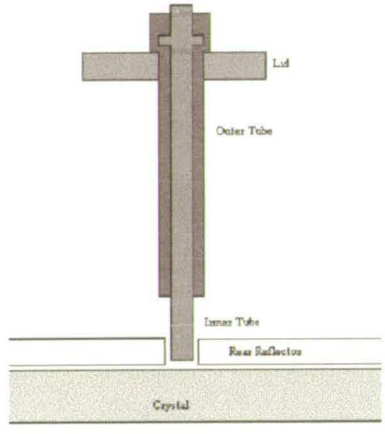

Figure 5-24. *The barrel module fibre attachment*

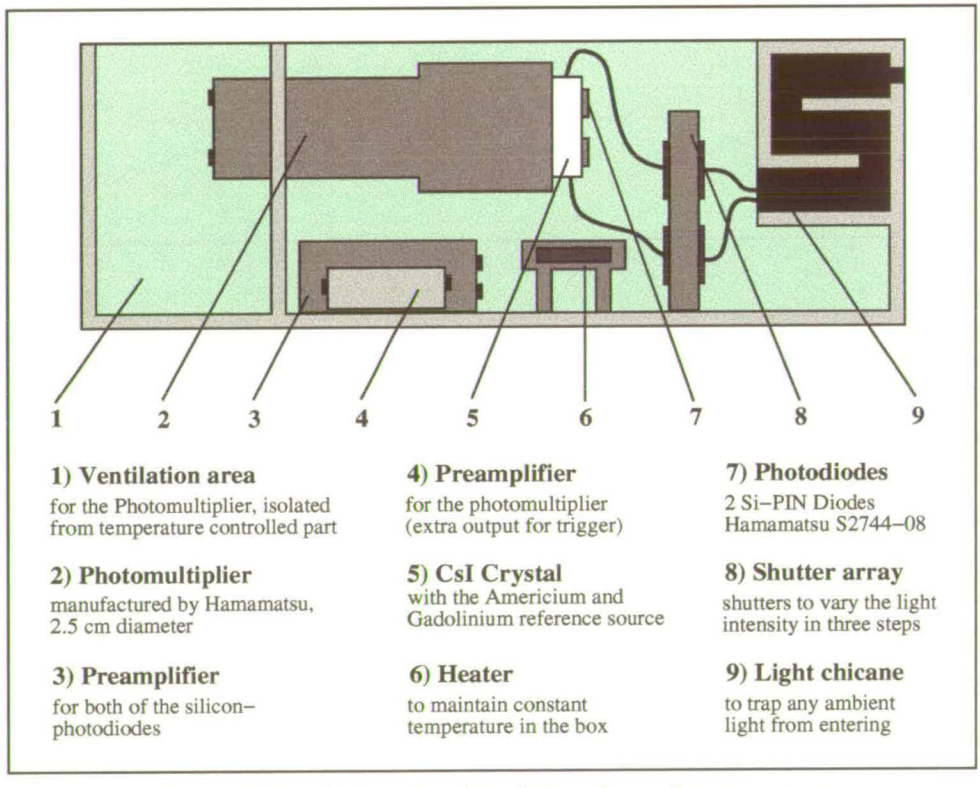

Figure 5-25. *Schematic of the light pulser reference system*

via CAN-Bus. The photomultiplier preamplifier has two outputs, one of which is for the light pulser trigger. To compensate for any drift in the reference system response there is a radioactive source next to the crystal. This contains gadolinium (^{148}Gd) and americium

(^{241}Am) providing two peaks corresponding to 5.49 MeV (85.2%) and 5.44 MeV (12.8%) alpha particles from ^{241}Am, and 3.18 MeV alpha particles from ^{148}Gd. The reason for having the two separate source peaks is to correct for any pedestal drift in the reference system electronics. The intensity of the sources are 44.56 Bq for the gadolinium and 29.05 Bq for the americium.

There is another "linearity" reference system which is used for a similar purpose to that above, but it can handle the large changes in the light intensity which occur when the light pulser is run in linearity check mode. This will be explained in the next section. Three reference fibres are taken from the barrel primary mixer and two from the endcap primary mixer. These are attenuated using an airgap and different neutral density filters with transmissions 100% (no filter), 25%, 5%. The airgap has a transmission of 75%. The different attenuations allow different fibres to be used in different intensity ranges whilst using a 12 bit ADC. The second reference system has all the features of the monitoring reference system and can be used as a replacement if it becomes necessary. Having a separate reference system for the monitoring isolated it from possible instabilities which may occur due the additional complexity of the linearity features.

The data from the reference system is recorded with a CAEN ADC, type V556S. It is a single width VME module which houses 8 12-bit peak sensing analog-to-digital converting channels. It has a multi-event buffer of 512 words. The ADC is controlled and set-up through the *BABAR* fast control system.

5.13 Light pulser operation

There are four basic modes of light pulser operation:-

Calibration This is the normal mode of operating for the light pulser monitoring. The run is taken using one intensity setting of both the high voltage and neutral density filter wheels. The length of each run is 1000 events and these data are automatically processed and difference plots are produced.

Linearity This is a run taken using a variety of light intensities. The range of intensities is achieved by driving the stepper motors to move the neutral density filter wheels and also by adjusting the high voltage supply to the xenon lamps. Data is taken for 2 seconds for each setting, with a trigger rate of 14.2 Hz, corresponding to about 28 events per setting. These runs are used to check the linearity of the calorimeter electronics. The calorimeter readout modules can be configured to have either the CARE chip auto-ranging or to force a particular range.

Diagnostic This is a very fast light pulser run taken for only 100 events for diagnostic purposes. This provides fast feedback on the electronics for diagnosing and fixing problems.

Diode A or B There are three possible modes of operation here. Light pulser runs can be taken using either A or B of the crystal readout diodes, or the sum A+B. This is useful to be able to diagnose faulty diodes and possible diode–crystal glue joint problems. The runs are taken using the standard electronic pulse calibration mode.

5.13.1 Trigger

The xenon lamps are triggered by pulses which are derived from the *BABAR* system clock. The frequency of the clock used is 59.5 MHz, and this is divided down in factors of two. The normal repetition rate for the light pulser system is 14.186 Hz which is a factor of 2^{22}.

The trigger signal for reading out a light pulser event is derived from the photomultiplier in the reference system which has as its input fibres from the primary mixer systems. This is more accurate than using the trigger of the lamps which has a time jitter of 200 ns.

The light pulser trigger rates are given in table 5.13.1.

Frequency for lamps / Hz	0.2	0.4	0.9	1.8	3.6	7.1	14.2	28.4
Frequency for source data / Hz	0.05	0.1	0.2	0.4	0.9	1.8	3.6	7.1

Between signals the ADC collects data from the sources and stores them in the multievent buffer. The source data from the peak sensing ADC are readout at the above rates. The pedestal data for the reference system can be taken at two different rates 907.90 Hz and 1815.80 Hz, where the data are collected for multiple gates by the multi-event buffer of the ADC. These data are then readout when a signal is given to fast control to readout the ADC. This occurs at repetition rates of 28.37 Hz and 56.74 Hz respectively.

5.13.2 The light pulser extension board

The light pulser extension board is designed to fit in a 9U VME slot in the DAQ crate. It houses the electronics to provide the following functions:-

1. Provide a system clock
2. Produce the light pulser trigger signal for the fast control.
3. Produce the gate signal for the ADC and control its running modes.
4. Produce the xenon lamp trigger signal.

The running modes for the ADC are to take normal light pulser data, to take source data, and to take pedestal data. The system is very flexible as all of these functions are implemented in a single XILINX chip, type XC3130A-2PC84C

5.13.3 Slow control and monitoring

The light pulser system is controlled by the *BABAR* slow control system. This is coordinated with the run control system because the settings change between the various runs. The parameters controlled are:-

- High voltage of the xenon lamps.
- Trigger of the xenon lamps.
- Stepper motors for the neutral density filter wheels.
- High voltage for the reference system photomultiplier tubes.
- Reference system shutters.
- Bias voltage for the reference system photodiodes.
- Various heating and environmental controls.

The environment of the reference system and the lamp assemblies must be stable and the temperature and humidity are continuously monitored. The output from temperature and humidity sensors is sent via CAN bus to the electronics house. There it is interfaced to VME for control by EPICS (Experimental Physics and Industrial Control System). All of the *BABAR* slow control is implemented by EPICS.

An overall schematic of the lightpulser electronics hardware and the interconnections is shown in figures 5-26 and 5-27. The EMC monitoring crate and the EMC data acquisition crate are located in the *BABAR* electronics house. The lamp boxes, reference system boxes and the NIM crate are located in the light pulser rack above the detector magnet.

5.14 Chapter summary

In this chapter we have presented in detail the design of the light pulser system. The system has been designed to look for short term changes in the calorimeter. The effect of radiation damage over short time scales is extremely small and a lot of work has been put into designing the system to be as stable as possible. It is also important for all the channels to be working reliably. The construction and commissioning of the system was completed successfully in 1999. In the next chapter results from the initial data demonstrating the performance are presented.

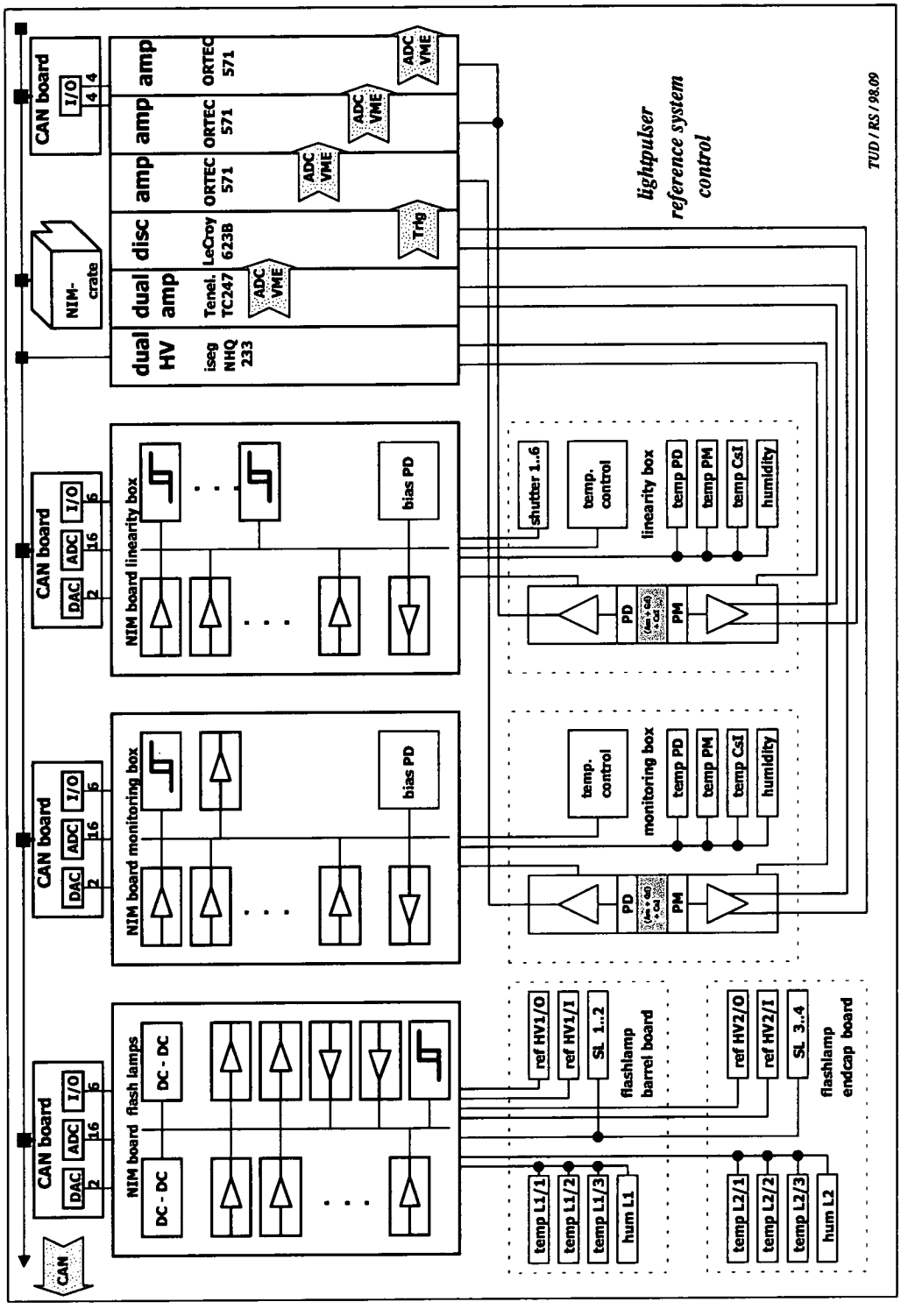

Figure 5-26. *Drawing of the light pulser reference system electronics*

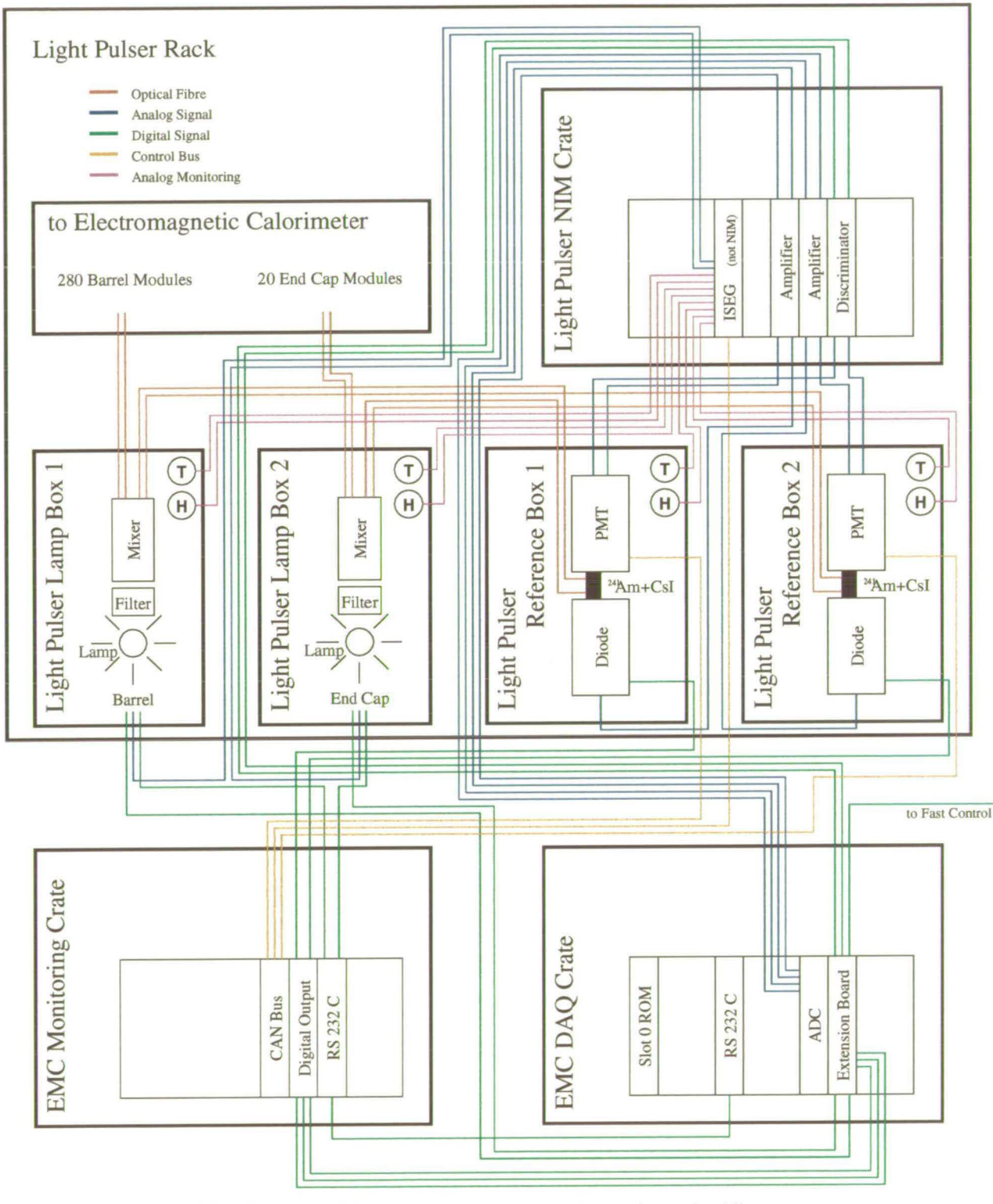

Figure 5-27. *Drawing of the complete light pulser electronics and cabling*

6

Light pulser system data analysis

6.1 Introduction

In the last chapter the hardware design of the light pulser system was covered. In this chapter initial results demonstrating the performance of the light pulser system will be presented. These will include the energy distribution and stability of the system, studies of the initial radiation damage, and a look at the importance of the light pulser system for diagnosing electronics problems. The changes and improvements in the light pulser system, which were made over the summer, will be discussed. For comparison purposes the results of other calibration and monitoring methods will be given. Lastly, a preliminary look at the correlation between the radiation damage and the total integrated luminosity from data-taking will be shown

6.2 The light pulser energy spectrum

The light pulser system injects a certain amount of light into each CsI(Tl) crystal in the calorimeter. The intensity of light in each crystal and the resulting amplitude of signal depends on a number of factors. There are many stages in the light distribution which may introduce non-uniformities in the light output of the respective channels. Every effort has been taken to ensure that the light output is as uniform as possible for the entire calorimeter.

The factors which can affect the uniformity of the light pulser system may be categorised into two types: optical couplings and light mixer systems. There are a number of places in the system where optical couplings were necessary. At these points high quality connectors were essential and sometimes had to be specially designed. Where there is such an optical connection, all the fibre optic terminations were assembled to as high a standard as possible and were polished to the same degree of optical finish. Different light outputs for each fibre can arise due to different qualities of the polishing finish and the possible damage of some fibre claddings during the gluing, polishing, and installation procedures. Lastly, the bulkhead connectors, used for the barrel calorimeter, are specially designed seven-to-seven connectors which may not uniformly distribute the light into each fibre with possible cross-talk between the fibres at this point.

The light mixer systems all have the same common feature. They take a large amount of light from a single source and distribute it into a large number of smaller fibre optics. There

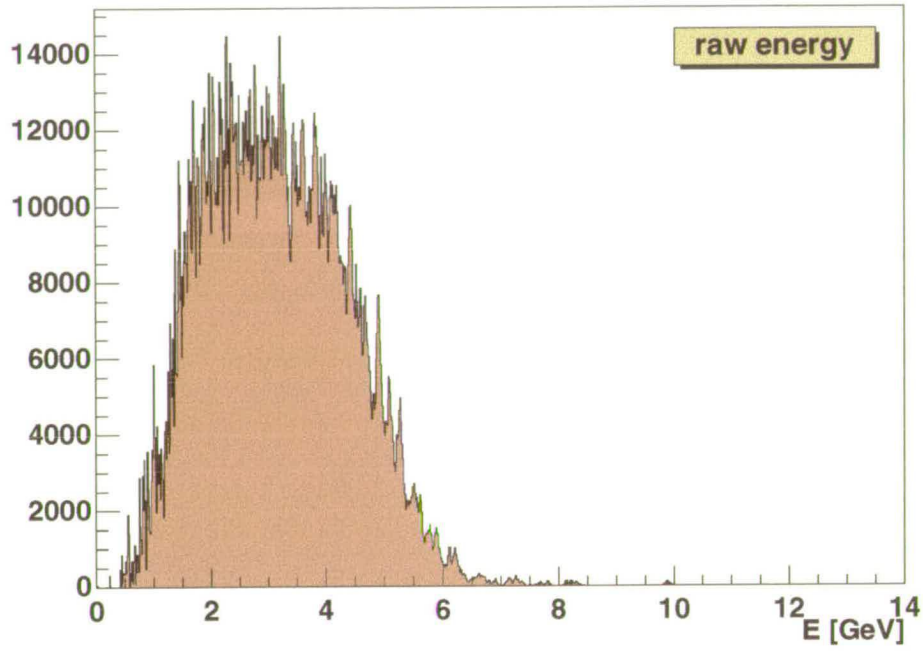

Figure 6-1. *The global unnormalised energy distribution of the light pulser system for the whole calorimeter*

As mentioned in the last chapter, the two systems endcap and barrel have hardware characteristics which differ considerably. The endcap light pulser system uses micro-lens technology to couple the light from the primary mixer systems into the primary fibres. This ensures that all the modes in the fibres are filled properly resulting in a full numerical aperture of light at the other end of the fibre and this properly illuminates the outermost fibres in the module mixer fibre bundle. Also there is no bulkhead connector in the endcap light pulser system. The seven-to-seven interconnect results in transmission losses which may not be uniform and in addition any interconnects generally lose the higher light modes in the fibres. Due to these reasons it was possible to achieve a better uniformity in the endcap light pulser system.

6.3 Stability of the system globally

It is important for the light pulser system to have as high a stability as possible. In figure 6-3 the stability of the system is shown. This is produced by a Gauss fit to the energy distribution in each channel. Some example plots of single channel energy spectra will be shown in the next section. The data is again normalised to the module mean to take out any pulse-to-pulse instabilities occurring due to the xenon flash lamps. From the plot it can be seen that there are a small number of channels which still have relatively large sigmas. This is due to the data

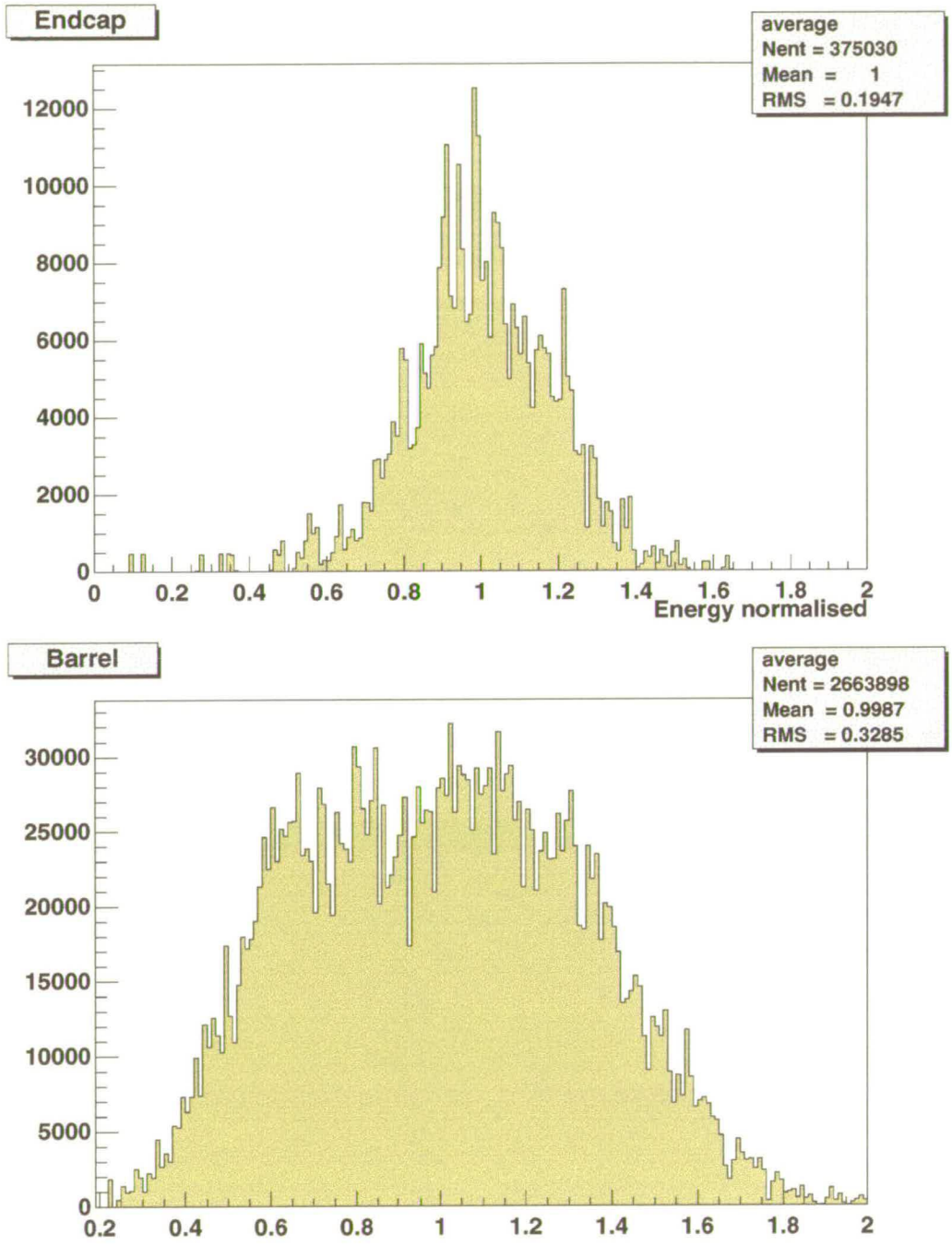

Figure 6-2. *The normalised energy distribution in the endcap (top) and barrel (bottom) light pulser systems. The energy is normalised to the mean energy of the crystals in each calorimeter module.*

being preliminary and there are still a few noisy channels present in the system for this run. Details of diagnosing such electronics problems will be covered in a later section.

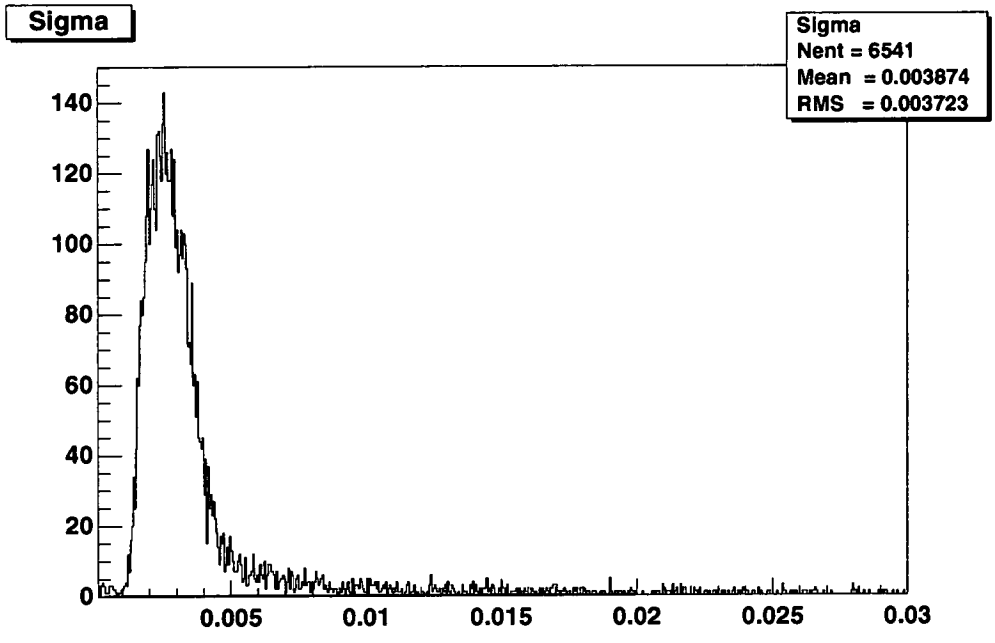

Figure 6-3. *The stability of the light pulser system where sigma is obtained by a Gauss fit to the normalised single crystal spectra.*

Scatter plots of the distribution in stability versus energy for the barrel and endcap light pulser systems are shown in figures 6-4 and 6-5 with a cut applied to channels with a sigma of greater than 0.5% to eliminate noisy channels. These plots show a correlation: the channels with larger mean energy tend to have better stability than those channels with lower energy. However, the change in stability is very small. There are a few possible reasons for this correlation. One possibility is that the channels with lower mean energies are likely due to having module fibres which are outermost in the fibre bundles, and the optical coupling at this point may be less stable.

6.4 Single crystal spectra

The signal in each channel of the calorimeter represents a single crystal readout by both photodiodes. Some sample spectra of the single channels are shown in figures 6-6 and 6-7. The energy distribution in single channels in the calorimeter is due to the light output of single crystal fibres. There are expected to be differences in the light intensity due to the profile across the module mixer. This will be looked at in the next section. The channels are normalised to the mean energy of the calorimeter module on a pulse-by-pulse basis. This leads to a stability in each channel between 0.1 and 0.4%.

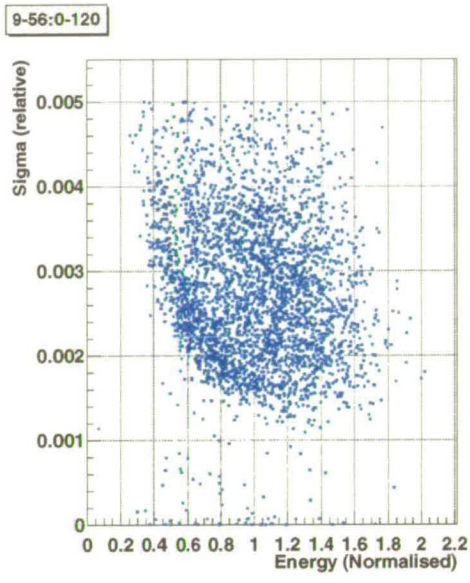

Figure 6-4. *The distribution of sigma in the barrel light pulser system. This shows a correlation between channels which have higher mean energy and those which have good stability. In addition the energy spread of the barrel light pulser system can be seen again in this plot.*

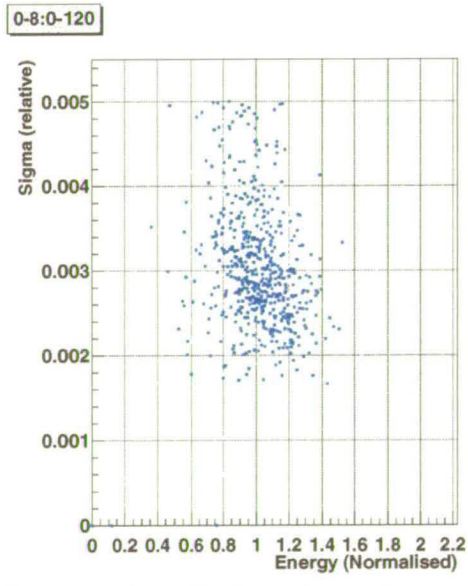

Figure 6-5. *The distribution of sigma for the endcap light pulser system. Again this shows a correlation between channels which have higher mean energy and those which have good stability. The good uniformity of the energy distribution in the endcap can again be seen from this plot.*

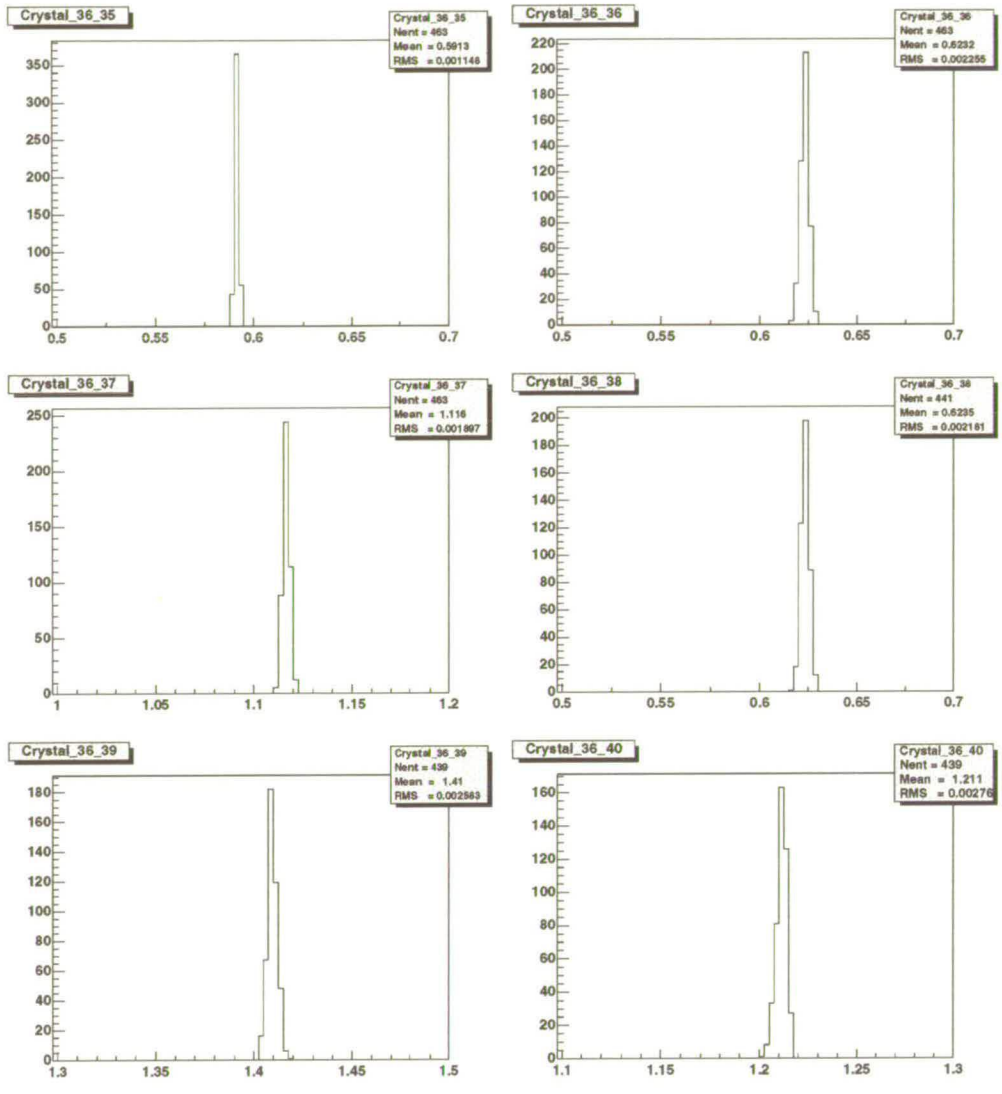

Figure 6-6. *Some normalised single crystal spectra in the barrel calorimeter.*

A few remarks can be made about the single crystal spectra. They clearly demonstrate that the modules mixers, fibre transmissions, and fibre-to-crystal optical couplings are all stable. These plots are all made by normalising the individual crystals to the light intensity of the primary fibre feeding the module mixer for that module. This primary fibre intensity is measured by taking the mean of all the crystals in each physical calorimeter module. The distribution of crystal energies in each module is shown in the next section.

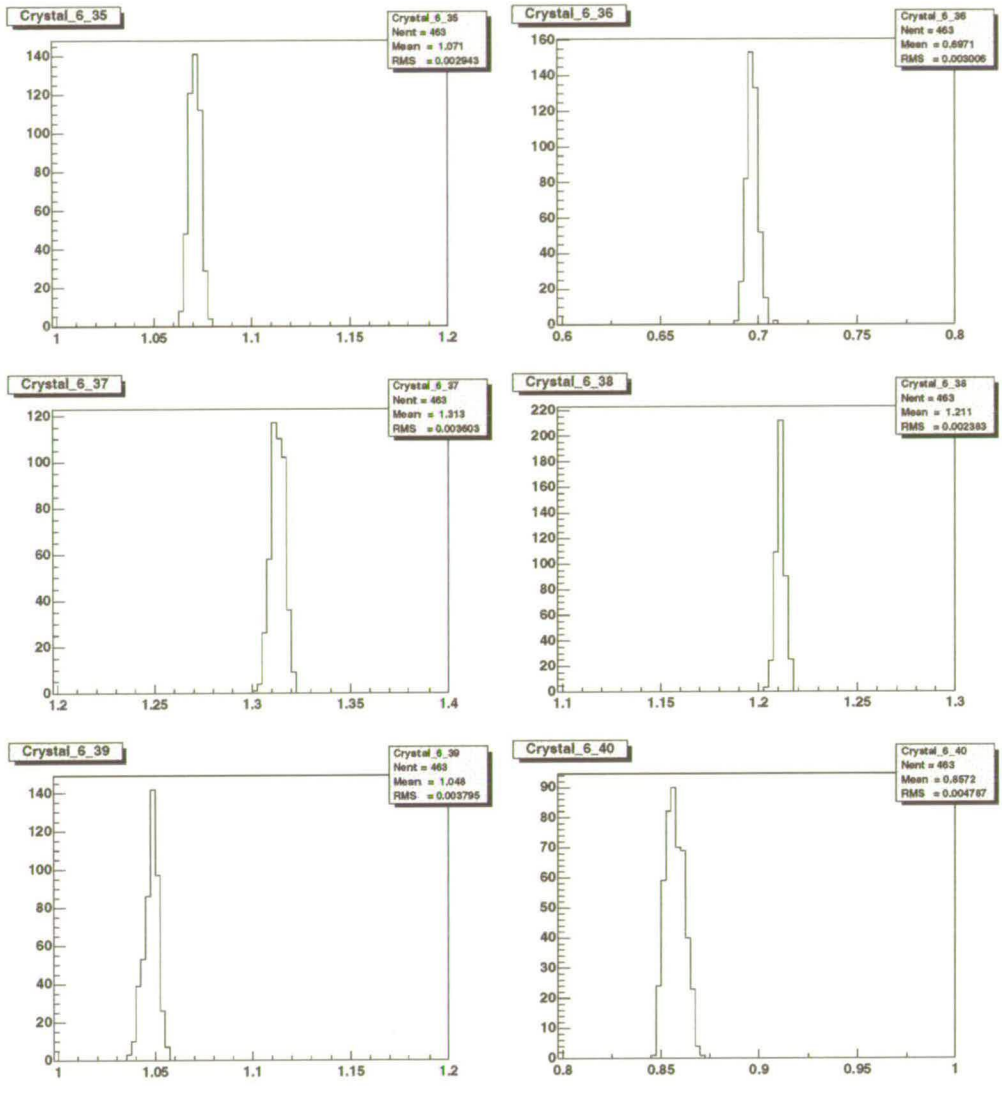

Figure 6-7. *Some normalised single crystal spectra in the endcap calorimeter.*

6.5 Module mixer distributions

The next area of non-uniformity of the system is at the module level. Here the spread of crystal energies in each module can be examined and this demonstrates how well the module mixers are performing. The distribution of crystal energies for four modules in the endcap, and the same for the barrel, are shown in figures 6-8 and 6-9 respectively. Each of the discrete peaks in the distributions represents approximately one or two fibres. The endcap light pulser has 41 crystals per module and the barrel 21 crystals per module. It can be observed from the

plots that the spread in energies for the endcap and barrel are essentially the same. The barrel module mixer has an air-gap of 3.4 mm and the endcap 4.0 mm.

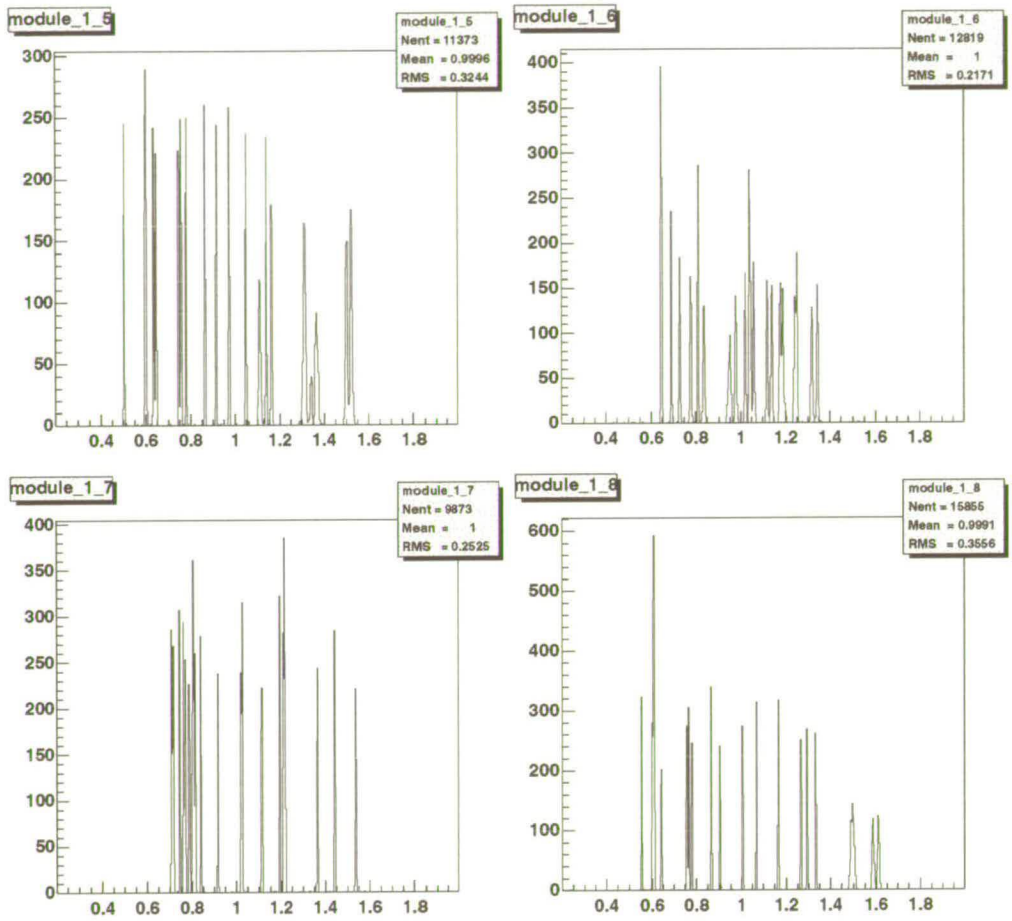

Figure 6-8. *The module mixer distributions for four calorimeter modules in the endcap.*

The main source of non-uniformities in the endcap light mixer system is due to this stage in the light transmission and it is a purely geometrical factor. When the module fibre bundles were quality assured it was observed that the light output of each fibre from the module bundles depends strongly on the geometrical position in the bundle. As you go out from the centre of the bundle the light output drops. The difference between the innermost and outermost fibres is approximately 30%. This is similar for endcap and barrel. Therefore it was important to densely pack the fibres to keep the endcap fibre bundles as small as possible. However, this had to been done carefully because if they are slightly over packed the 15 μm cladding gets squashed and light losses occur. The uniformity of the module mixers can be improved by a larger air-gap, but this induces a greater light loss and is less stable.

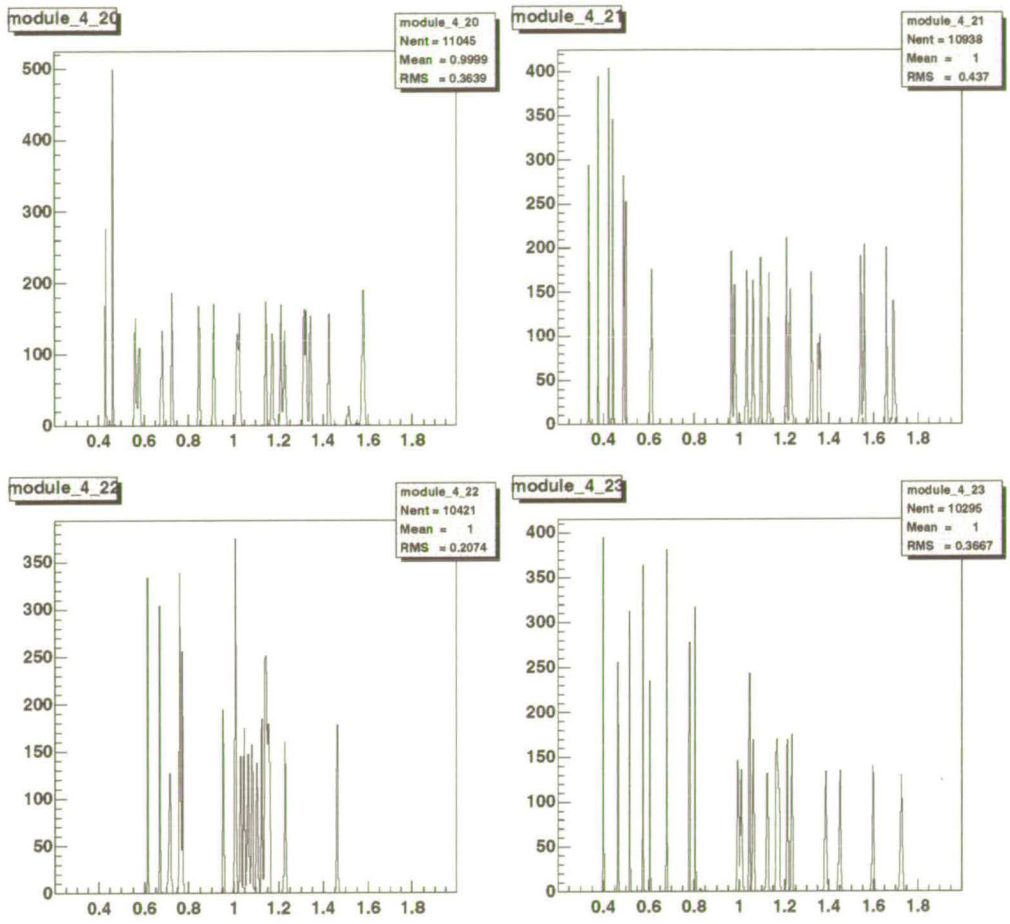

Figure 6-9. *The module mixer distributions for four calorimeter modules in the barrel.*

6.6 Primary mixer distributions

The last level to examine for non-uniformities in the endcap system is the primary mixer distribution. This shows how uniformly the primary fibres are illuminated by the light mixer bar. Uniformity is crucial at this point so that the light that is input into the reference system fibres is as close as possible to the the light that is sent to each module. The primary mixer distribution is shown in figure 6-10. It can be seen that there was one fibre which has a lower light output than the rest. However, this was fixed when a larger primary mixer bar was used, see section 6.10.

Each of the peaks in this distribution represents one or two of the twenty separate primary fibres feeding the twenty endcap calorimeter modules. The distribution shows that the spread across the primary mixer is around 9%. This is clearly less than the module mixer, but is still a contributing factor to the global energy spread shown earlier. The spread is due to a number

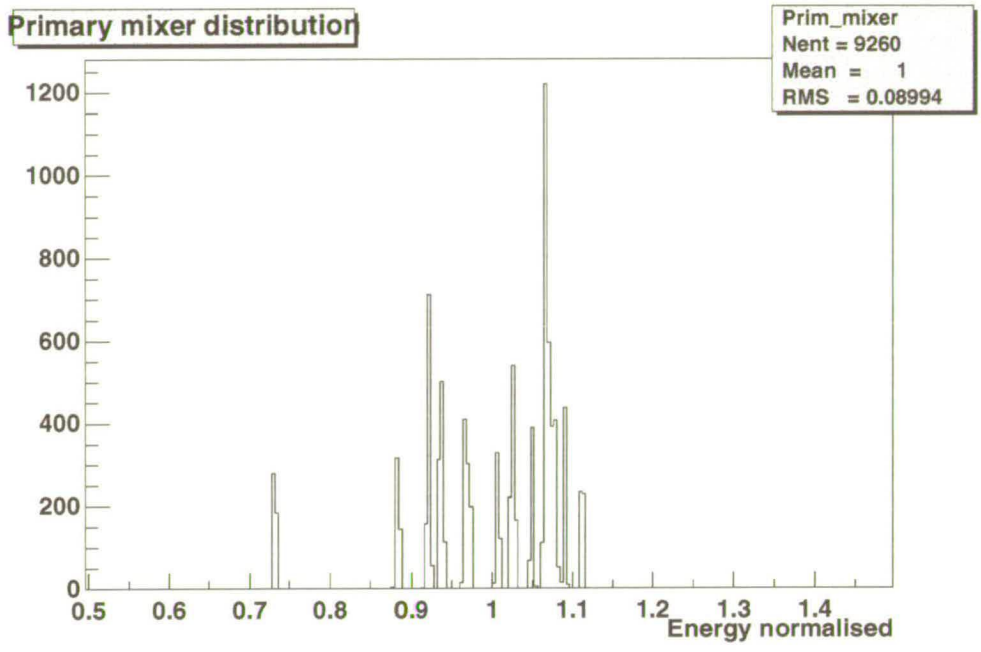

Figure 6-10. *The primary mixer distribution of the endcap primary mixer system*

of things. The profile of light intensity exiting the primary light mixer bars is an important factor. The optical quality, alignment, and gluing of the micro lenses is important. Another factor here is the transmission property of the primary fibre and the optical coupling to the module mixers.

This distribution is produced by using a different method to that of the previous plots. It is normalised to its own mean which represents the global energy of the whole endcap on an event-by-event basis.

6.7 The bulkhead connectors

For the barrel a similar plot to the primary mixer distributions can be shown. In figure 6-11 two distributions are shown for sets of seven modules. There are forty such distributions and these show the distribution across the bulkhead connectors. However, the bulkhead connectors are simply seven one-to-one connections so this distribution also contains the non-uniformities coming from the primary mixer.

The non-uniformity is around 15% which is twice as great as the primary mixer distribution for the endcap. This is probably due to the array of micro-lenses in the endcap primary bundle having better uniformity, or because additional non-uniformities are being produced

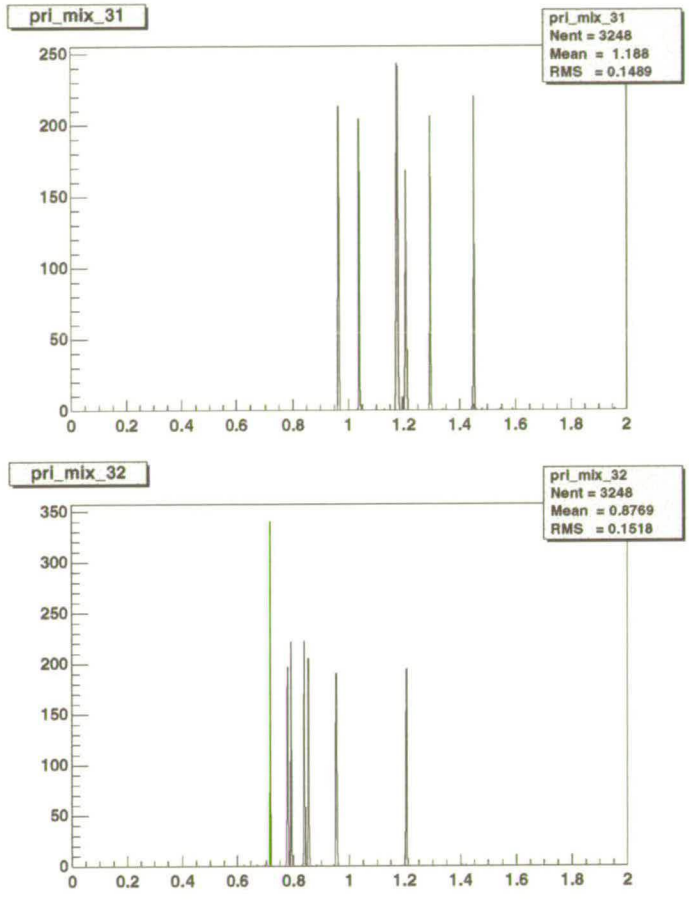

Figure 6-11. *The energy distribution of a bulkhead connector and primary mixer combined (barrel)*

in the barrel by the bulkhead connectors. These are the reasons why the barrel global energy distribution is much wider than that of the endcap.

6.8 The stability of the module means

The plots so far show the stability of the system within a light pulser run. It also important to have good stability between runs. This is crucial to measure absolute changes in the calorimeter due to radiation damage.

If we take the module means corresponding to each primary fibre and study their stability over time we can see the stability of the primary mixer system. The evolution over time of some sample module means is shown in figure 6-12. These data are normalised to the mean energy of the whole endcap to take out any global changes in the system. Unfortunately the primary mixer systems were not very stable during August and September 1999 and this is clear from

the plots. However, this was corrected by using a mixer bar with a larger cross-sectional area. This is discussed in section 6.10.

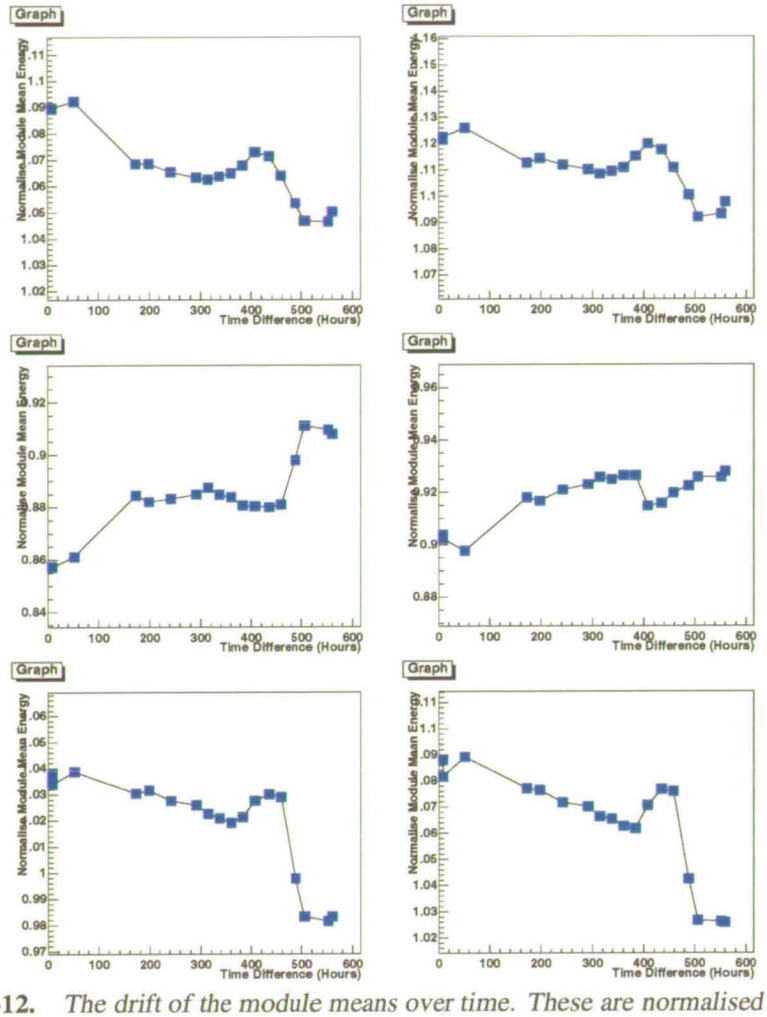

Figure 6-12. *The drift of the module means over time. These are normalised to the global mean of the endcap*

6.9 Long term stability of the global mean

In figure 6-13 the time evolution of the global endcap mean is shown. More precisely this is the average of all the endcap module means. The plot shows large systematic variations. These are mainly due to instabilities in the lamp assemblies and primary mixers. This is the main reason for having a reference system which should correct for such changes of the global mean over longer term time scales. However, due to the instabilities in the primary mixer distributions the fibre coming from the primary mixer, which feeds the reference system, could not be used to correctly normalise the changes in the system. However it was possible

to overcome this instability by investigating only relative changes in the calorimeter due to radiation damage. In the next section we discuss the changes to the system which were made in September and during the October shutdown to help improve the situation.

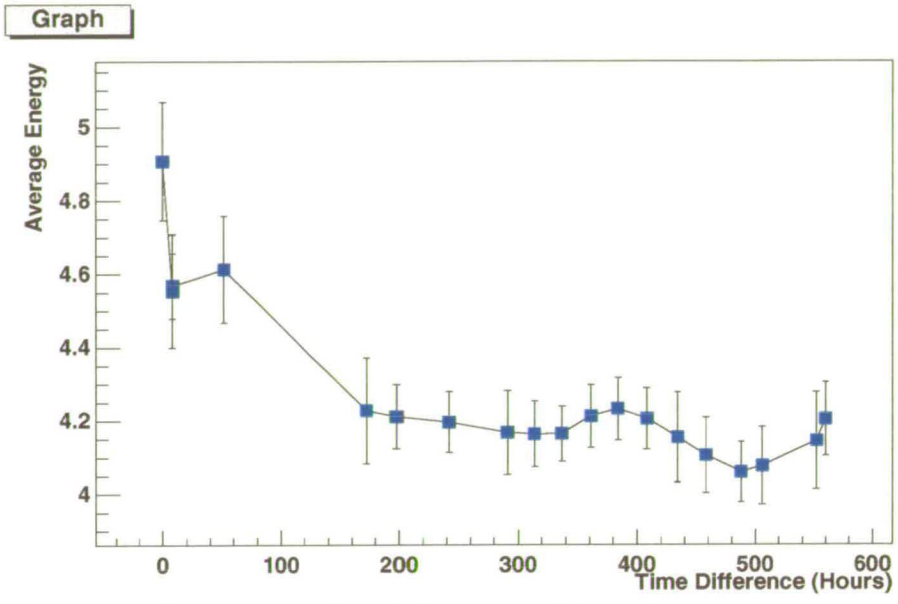

Figure 6-13. *The variation of the global energy of the endcap calorimeter over time, taken from the average of the module means for each run*

6.10 System improvements

During the summer of 1999 there were a number of changes to the light pulser system to improve the system. The first and most important change was to introduce climatic controls to the light pulser racks above the detector. The humidity and temperature of this environment were undergoing changes all the time and the change in humidity was correlated to instability between light pulser runs.

The light pulser system was split between two racks to provide more space. One rack contained the NIM crate, reference system and dehumidifier, the second the two lamp boxes which hold the xenon lamps, filters, and primary mixer assemblies for the endcap and barrel systems. Both racks were sealed to be as airtight as possible.

The climatic controls introduced were two AC units which are located on top of each light pulser rack. A dehumidifier unit manufactured by Munter now circulates dry air through the lamp boxes, extracting any moisture. The dehumidifier is working and controls the humidity to 8% $\pm$ 0.1%. The temperature is around 30 °C and controlled to $\pm$1°C.

Another change to the system was that the cross-section of both of the primary mixer bars was increased to 30×30 mm. This helped to increase the stability of the system. The energy distribution of the primary fibres exiting the mixer is shown in figure 6-14. The distribution has actually become wider and therefore the uniformity of light output across the mixer bar has decreased. However, this improved the stability between runs. In addition the widening of the distribution has meant that there is no longer a single fibre offset from the distribution as there was in figure 6-10

In the calorimeter electronics noisy low voltage power supplies were located. The coherent electronic noise in the calorimeter has now been reduced to less than 1 MeV. Some dead channels in the electronics were fixed.

Lastly, a new feature extraction for the light pulser system runs was introduced recently. This was found to improve the data significantly, especially in the linearity checks. There are more details on this in a later section.

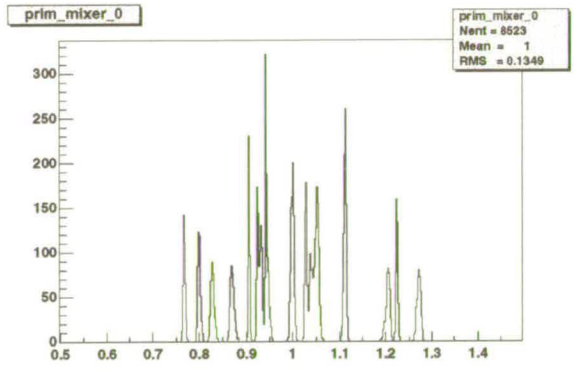

Figure 6-14. *The energy distribution of the primary mixer bar after the installation of the* 30×30 mm *mixer bar*

6.11 Electronics diagnosis

It was mentioned in the previous chapter that the light pulser is extremely useful for diagnosing electronics problems in the calorimeter. The system has proved itself to be useful throughout all stages of the calorimeter assembly. Firstly, it was used to check that each of the electronics channels was working during the calorimeter assembly. In particular using the data from the channels for diode A and diode B on each crystal it was possible to diagnose problems in the crystal to diode-plate glue joints. One module had many damaged glue joints after the ambient temperature went through a large fluctuation due to a power failure, resulting in stress on the glue joints. The light pulser was the primary method of diagnosing this. It also proved very useful when a module was damaged during the assembly. It quickly showed which crystals and channels were badly damaged and which were not.

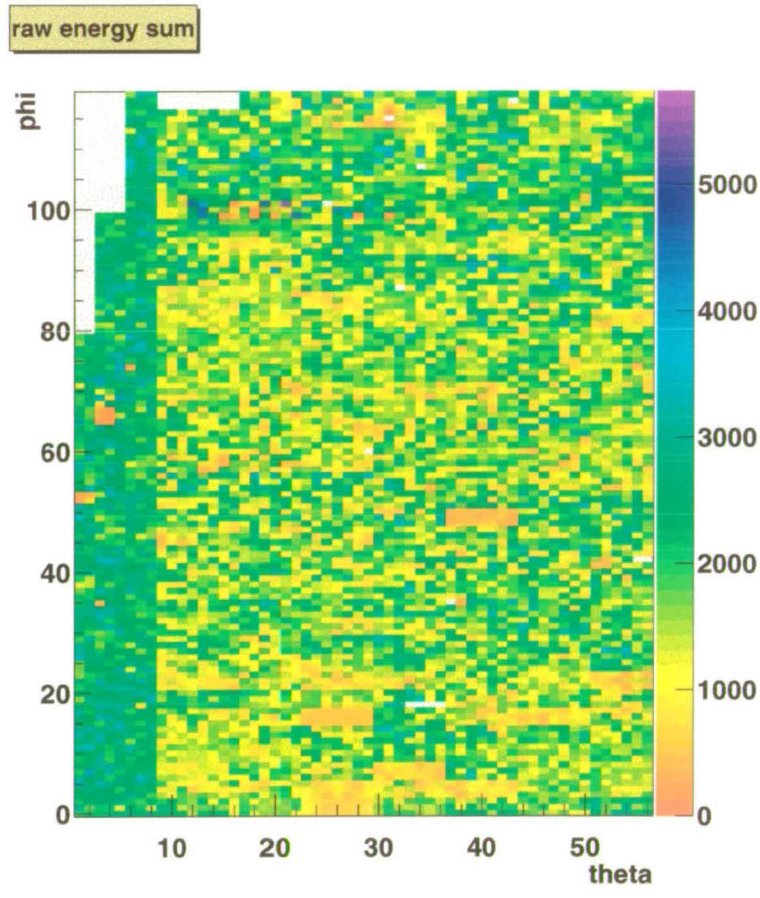

Figure 6-15. *For part of the data taking there was a damaged readout fibre. This light pulser run which was taken in a few minutes shows the missing section of the calorimeter in the top left corner. Also there is a noisy power supply around* $\phi = 100$

After the module assembly was complete the electronics calibration was used as the primary means for tracking electronics problems. However, this took a considerable amount of time and the light pulser system proved to be very fast and useful for this purpose. The entire readout chain for the calorimeter is quite complex and there are many places where an electronics problem may occur. First of all a readout module for the calorimeter may have failed to reboot properly and this results in a lot of crystals missing. For each readout module there are three readout fibres coming from the calorimeter and there may be missing channels if a fibre is damaged, or more likely if the Finisar transmitter for the readout fibre on the calorimeter fails. In figure 6-15 there is a two-dimensional energy plot produced using 100 light pulser events. This type of diagnostic run only takes a few seconds. In the top left corner of the plot there is a rectangular block of missing channels due to a damaged readout fibre. Another example is shown in figure 6-16. In this plot there are several readout modules missing from the barrel channels. These are easily spotted as the long straight strips of dead

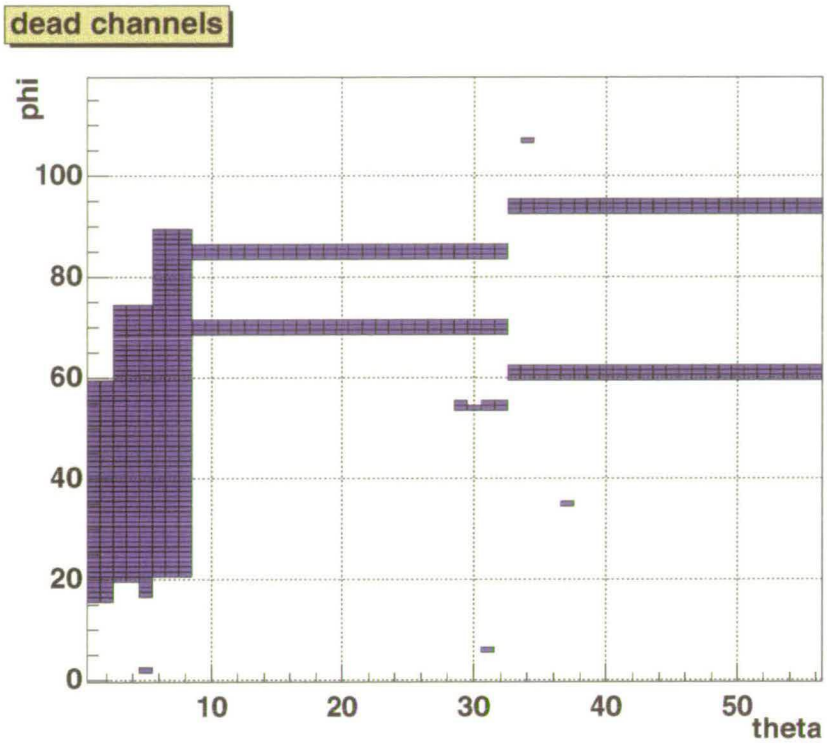

Figure 6-16. *An example of a light pulser run taken where there are missing readout modules. The strips of dead channels are due to missing barrel readout modules. The large area of dead channels on the left of the plot is due to various missing low voltage power supplies for the endcap.*

channels spanning half of the barrel. The sizeable chunk of data missing from the endcap at the left of the plot is due to missing low voltage power supplies. The last plot is shown in figure 6-17. This shows a very useful summary plot produced from the light pulser system which sums the energy in the channels corresponding to each readout module. This is useful to the person on shift because it shows quickly that there is a faulty readout module and gives the crate and slot where it is located.

6.12 Radiation damage in the calorimeter

In August and September 1999, there was a lot of initial data taken by the *BABAR* detector. This amounted to around 1fb^{-1} of data for the period of time studied in this analysis. The data taken are shown in figure 6-18. Using the light pulser runs taken on a daily basis during these two months it is possible to look at the radiation damage to the calorimeter. It is important to note that the changes due to the radiation damage are very small and the light pulser system must be particularly stable to measure them. There were many hardware changes and fixes which made the data particularly difficult to understand.

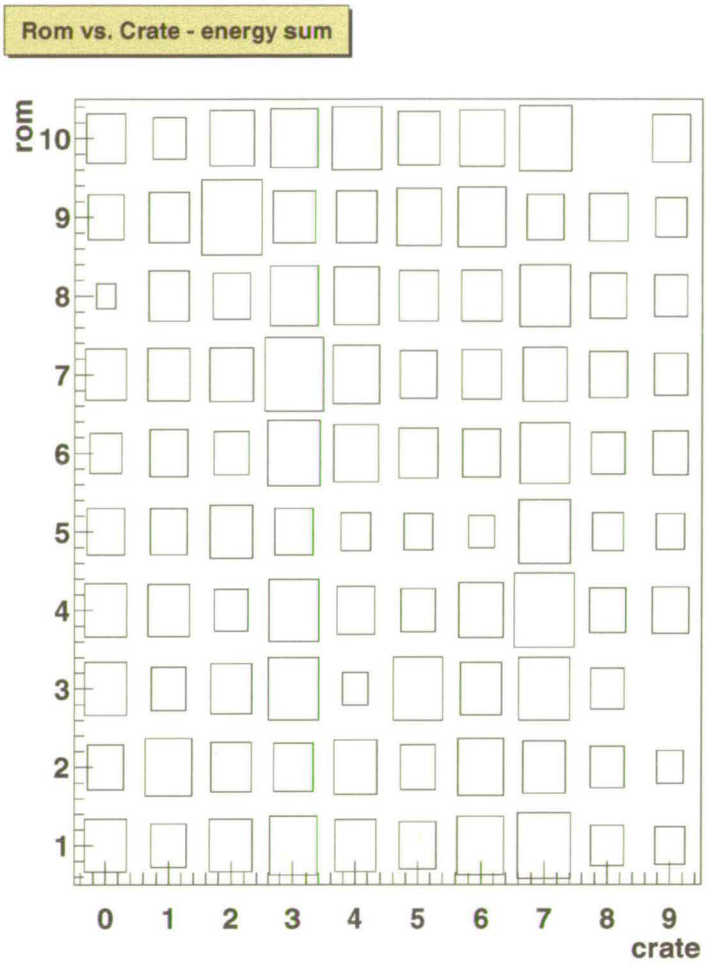

Figure 6-17. *A useful summary plot produced by the light pulser system which shows where there are bad or missing readout modules and their location in the calorimeter racks located in the electronics house.*

In figure 6-19 the change in light yield of the innermost rings and the outermost rings is shown. These data are normalised to the module means. Instabilities in the system on a module to module basis coming from the primary mixer system meant that normalising the light pulser data to the reference system was not possible. However, normalising to the module means is actually the most accurate way to get relative changes within a module, because any long term instabilities between the light pulser runs are factored out.

The changes in the innermost ring are expected to go down with respect to the module mean. This is due to the higher levels of radiation and resulting damage to which the inner ring is exposed. The outermost ring and most of the other rings will go up with respect to this module mean. This tendency can be seen in the data for August. However, the data are not

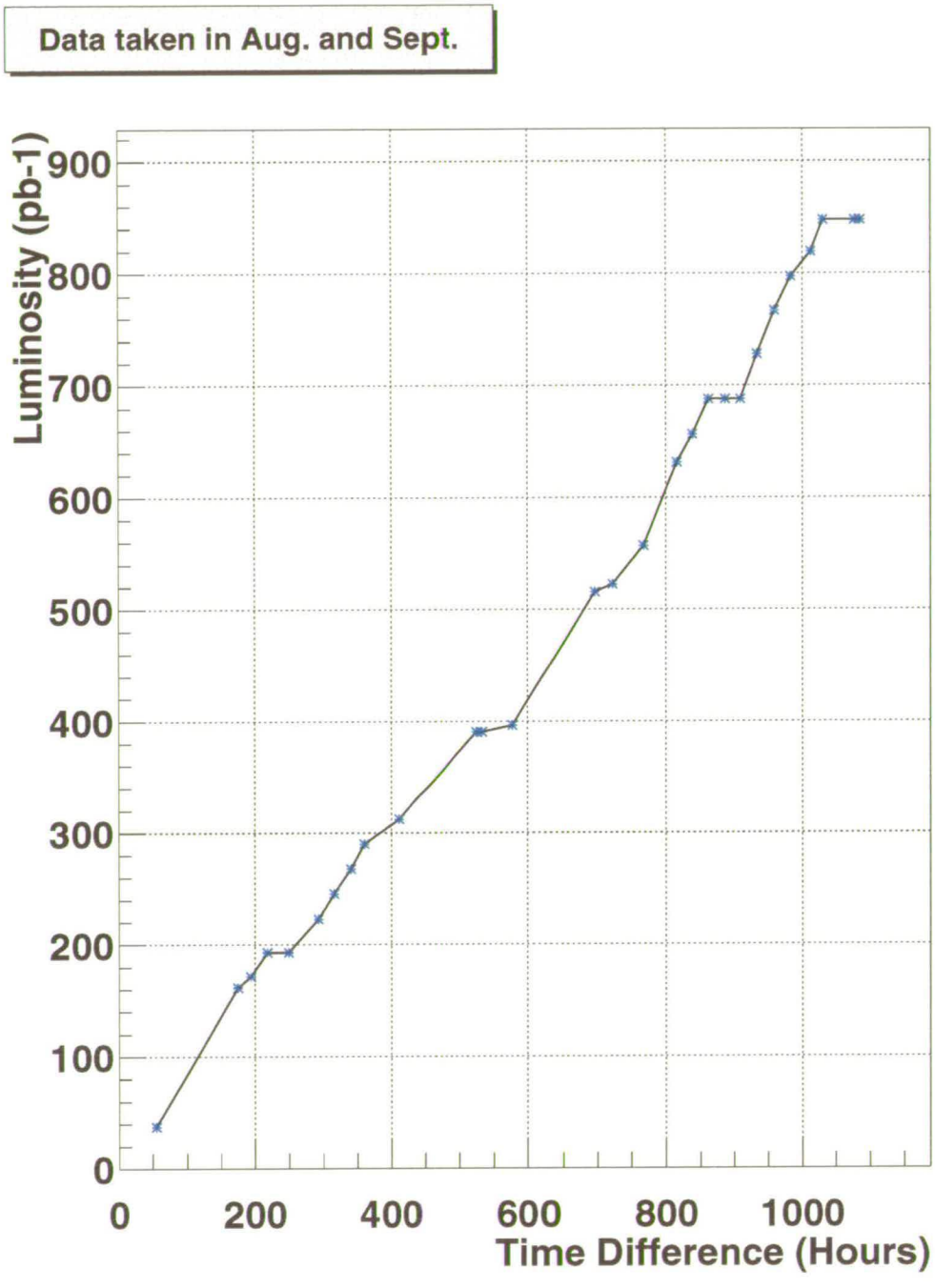

Figure 6-18. *Integrated luminosity taken by BABAR in the period studied in this analysis: August and September, 1999*

particularly good and the light pulser system and calorimeter electronics did undergo many changes during this period.

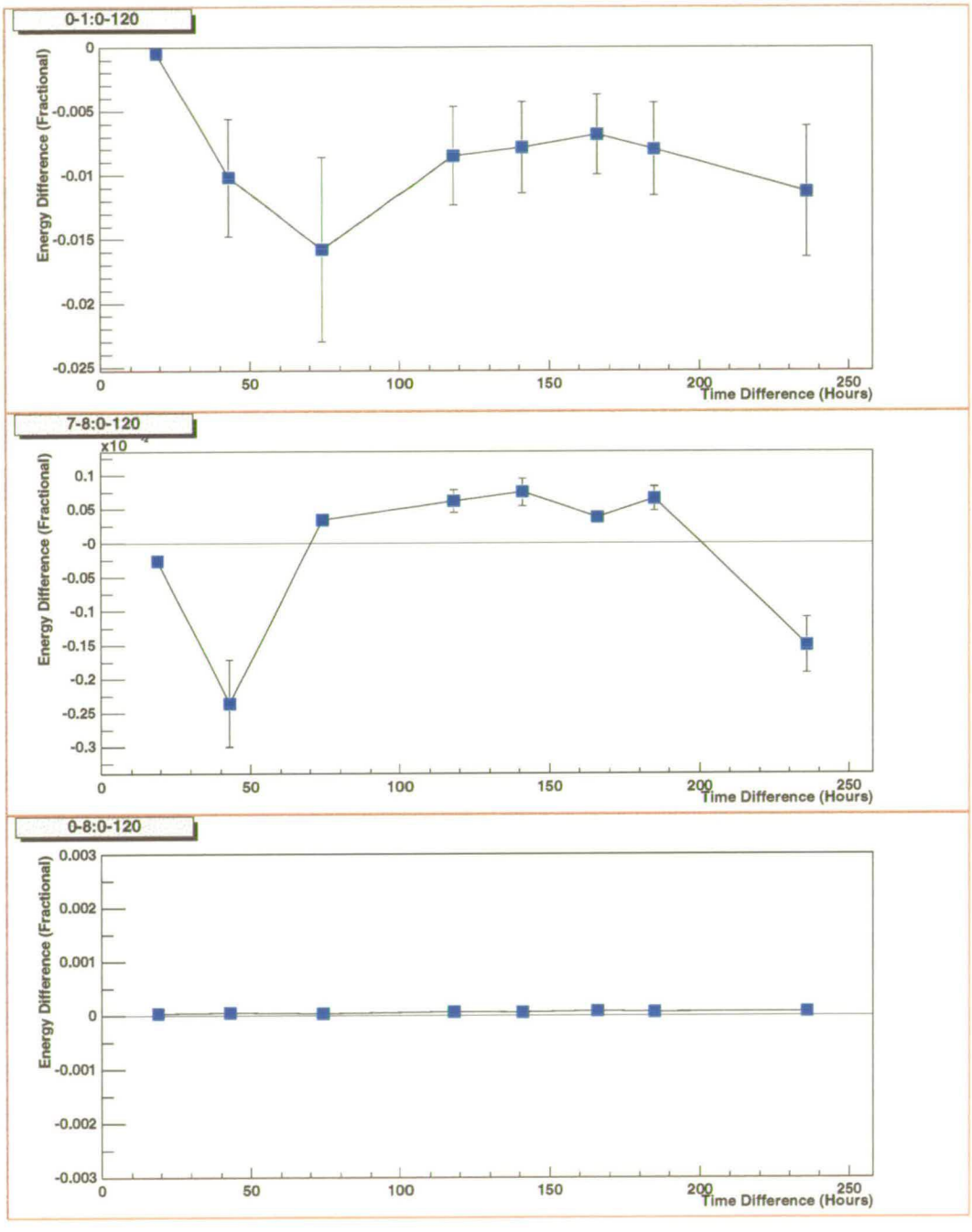

Figure 6-19. *Changes in the innermost (top) and outermost (middle) rings of the endcap, from August 23 to September 2, 1999. The bottom plot is a cross-check showing that the normalisation to the module mean gives an average change of zero when summed over the whole module*

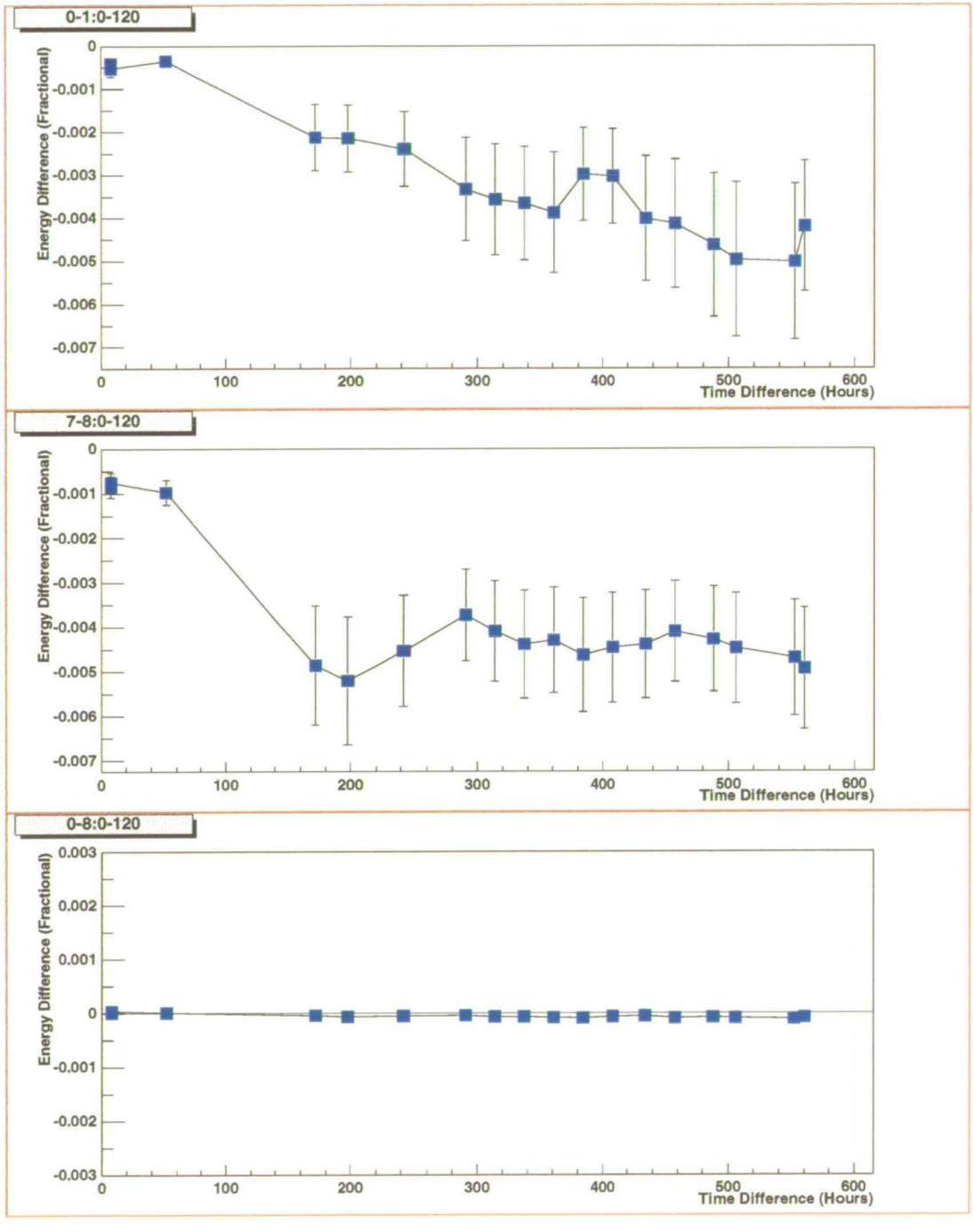

Figure 6-20. *Changes in the innermost (top) and outermost (middle) rings of the endcap, from September 7 to September 21, 1999, with respect to the normalised module mean.*

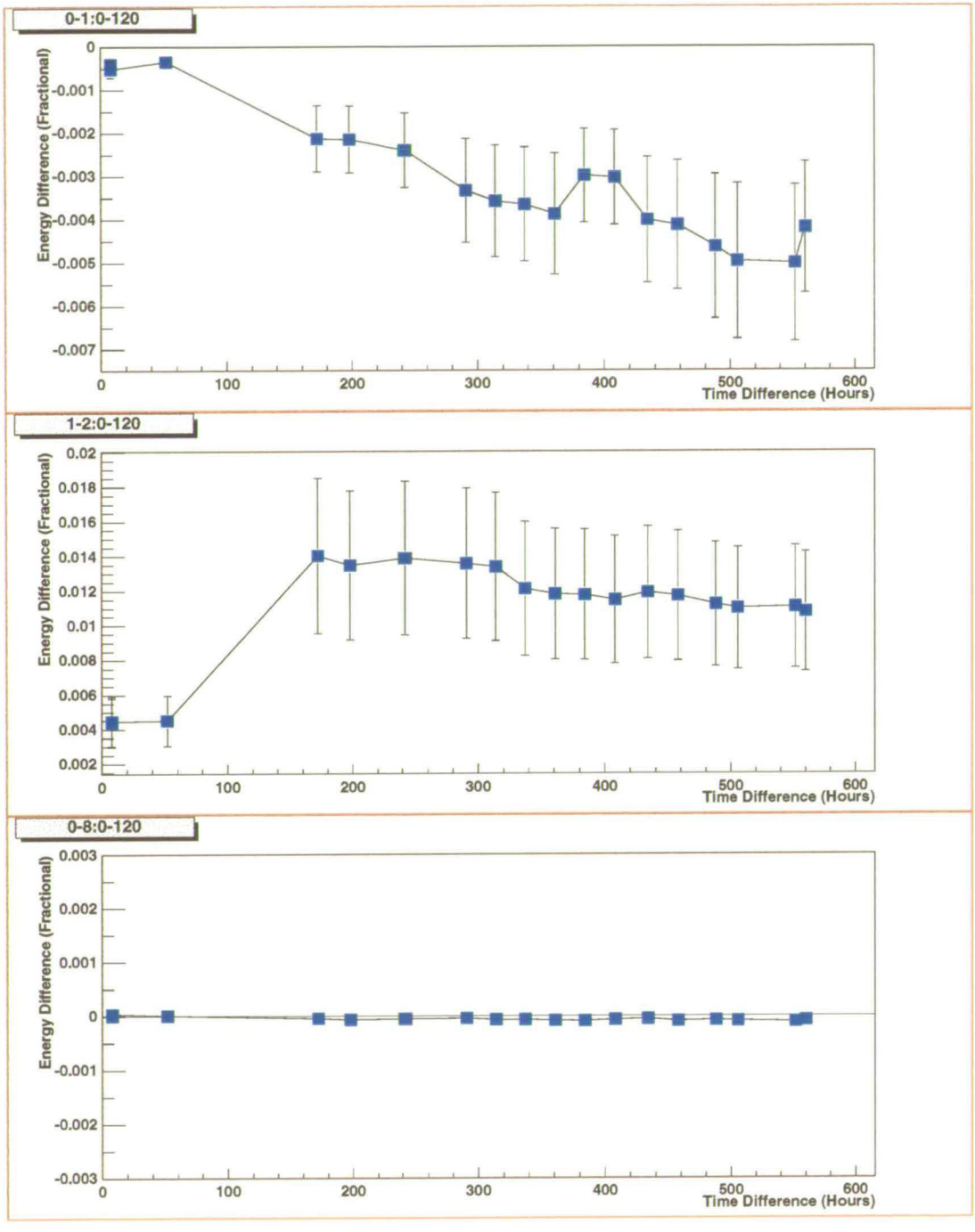

Figure 6-21. *Changes in the innermost (top) and 2nd innermost (middle) rings of the endcap, from September 7 to September 21, 1999, with respect to the normalised module mean.*

The data for September are better and the tendency for the innermost ring to go down is clearly seen in figure 6-20. There is still some change to the system between the second and third data points. This can also be seen in figure 6-21 which is the same plot, but the comparison is to the second innermost ring rather than the outermost one. This change to the system could be due to a large amount of radiation damage to the inner ring during this period but not to the other rings. It is expected that the radiation damage may be non-uniform in this respect. More likely there was again some small change in the electronics. The calibration constants in the front end changed around this period due to the radioactive source calibration. However, these plots indicate a clear decline in the light output. These data do not contain the global change in the endcap because this is normalised out of the data. To get the global change it is necessary to use the light pulser reference system.

6.13 Reference system source data

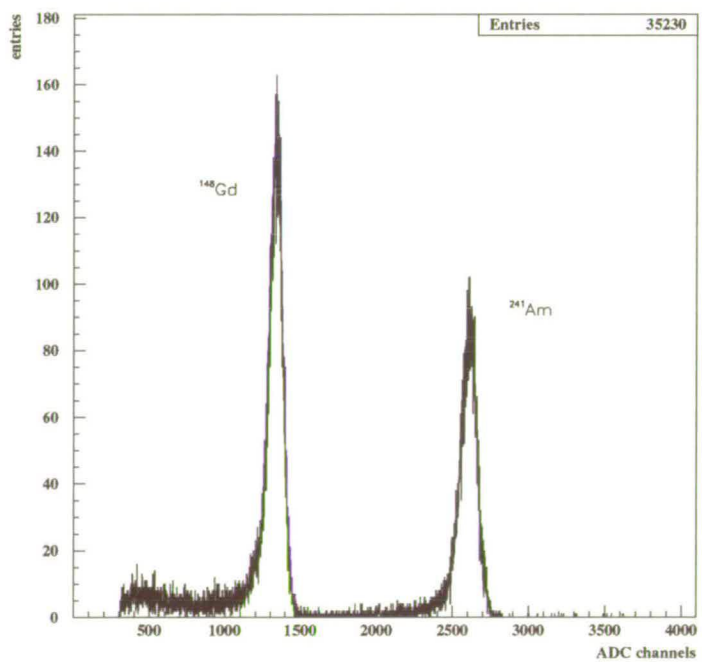

Figure 6-22. *The reference system source spectrum readout by the photo-multiplier tube.*

Using the reference system photo-multiplier tube and photo-diode the source spectrum was read-out and is shown in figure 6-22. The gadolinium peak and americium peaks are clearly shown. The relative rates of the the two sources which are combined were compared and found to agree with the manufacturer's specifications.

The sources are used to calibrate the reference system to correct for any long term drift. The combined source was chosen so that the separation of the two peaks could be used for the calibration and that this should be independent of any global shift in the system

6.14 Reference system light pulser data

The reference system collects data during a light pulser run in a photo-multiplier tube and photo-diode to normalise the light pulser system data on an event-by-event basis. However, most of my analysis has been carried out using the module means to normalise the system. As mentioned already this was due to instabilities in the primary mixer systems which made it difficult to use the reference system for this purpose. This is the main reason for all the improvements made to the light pulser system which were mentioned in section 6.10. However, the reference system itself is functioning correctly. In figure 6-23 the two peaks from the barrel and endcap light pulser systems are shown. The two systems have different hardware and filter settings and are therefore at different energies. This shows the reference system being successfully readout. The average energy recorded in the reference system over a period of 600 hours is shown in figure 6-24. This shows the drift of the light pulser system over time being recorded by the reference system.

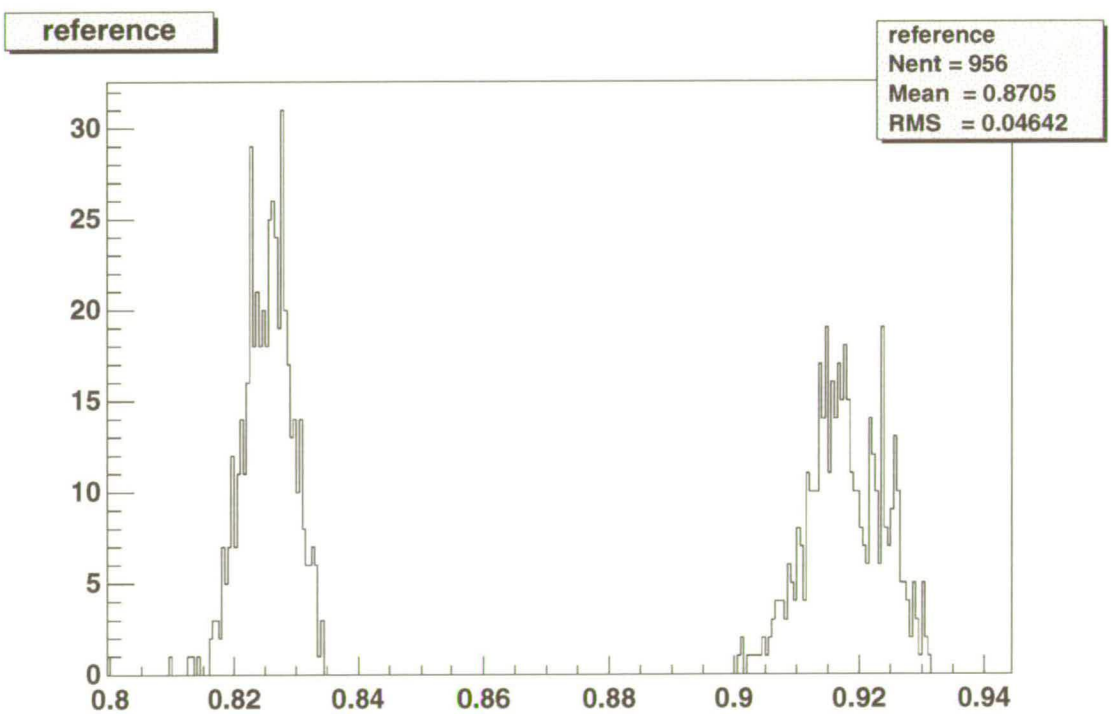

Figure 6-23. *The reference system lamp spectrum.*

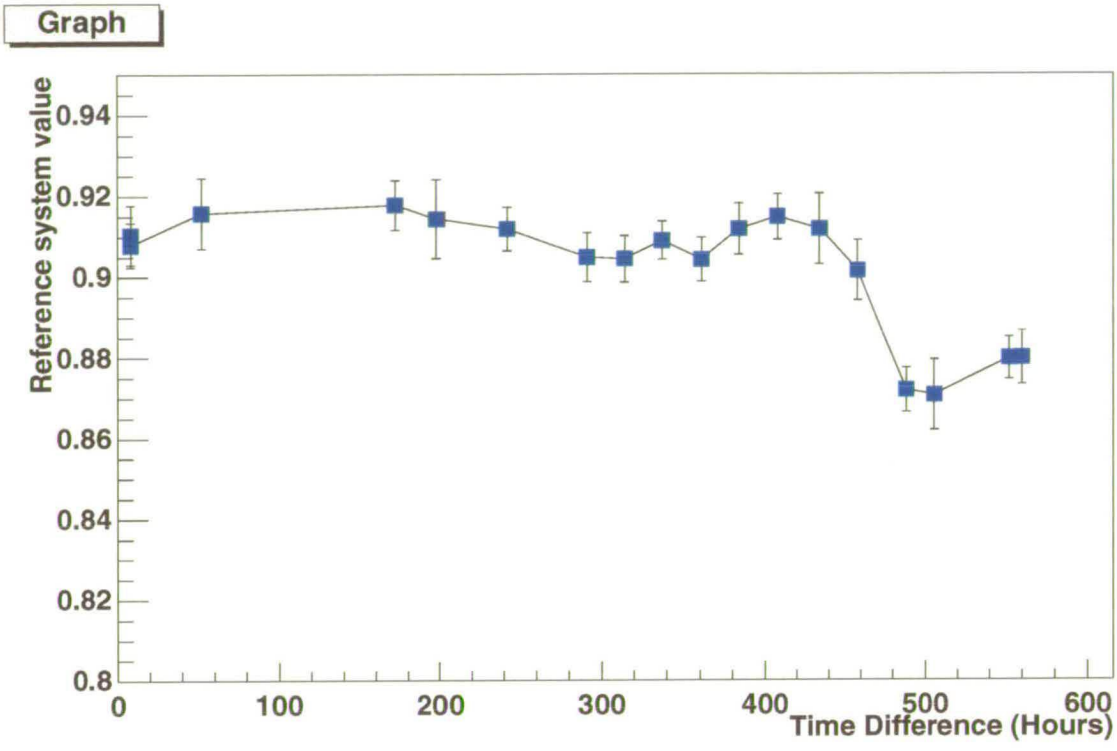

Figure 6-24. *The time evolution of the mean energy in the reference system*

6.15 Other measurements of radiation damage

There are a number of other methods which may be used to investigate radiation damage. There are the radiation doses measured by sensors on the calorimeter, the calibration constants from the liquid radioactive source calibration, and the calibration constants obtained from Bhabha events.

6.15.1 RADFETs

The calorimeter has a number of radiation sensitive field effect transistors (RADFETs) located on it to measure the radiation dose to which it is exposed from PEP-II. The readings of these sensors are given in table 6-1. There are clearly larger doses of radiation in the most forward parts of the endcap and there is also a noticeable azimuthal dependence. This is more clearly seen in figure 6-25. There are twenty sensors arranged azimuthally around the endcap corresponding to the locations of the endcap module, and three sensors arranged through the polar angle.

	θ		
ϕ Module	Inner	Middle	Outer
1	39.6	33.6	28.4
2	37.4	30.7	36.6
3	34.8	31.3	25.9
4	34.9	29.8	27.3
5	32.5	28.1	25.5
6	50.0	48.8	44.5
7	49.5	45.9	46.2
8	60.8	51.0	48.4
9	53.6	65.3	47.8
10	64.2	54.2	33.9
11	61.4	53.4	48.5
12	59.5	51.2	51.2
13	56.4	25.3	45.0
14	52.8	47.0	42.9
15	52.1	47.3	44.5
16	49.7	29.4	59.5
17	38.8	30.1	28.9
18	40.5	33.0	28.9
19	41.6	34.8	28.1
20	39.4	33.9	30.9

Table 6-1. *The total radiation doses (rads) measured by the RADFETs as of 6th October 1999*

6.15.2 Liquid radioactive source calibration constants

The radioactive source calibration constants from each source run can be compared. This is shown in figure 6-26. The different colours of points correspond to the different rings of the endcap. The lowest points correspond to the innermost ring of the endcap and the highest ones are the outermost ring. There is clear evidence for a 4% drop in the inner ring and a 2% drop in the outer ring. This agrees with the differential effect obtained from the light pulser system which is totalled to be around 2%, and it is also consistent with the radiation doses measured by the RADFETS.

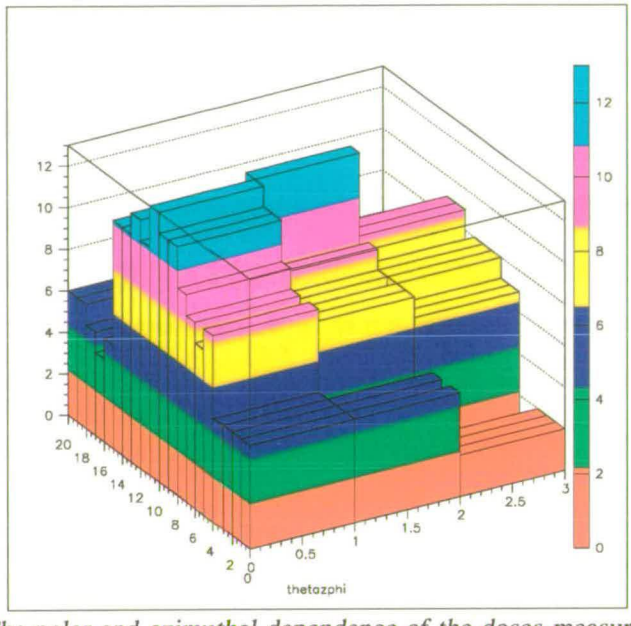

Figure 6-25. *The polar and azimuthal dependence of the doses measured on the endcap calorimeter.*

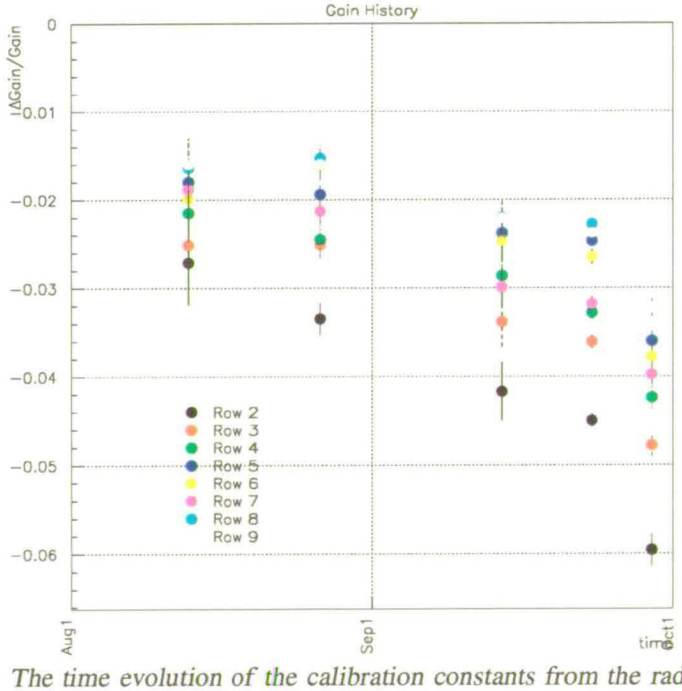

Figure 6-26. *The time evolution of the calibration constants from the radioactive source calibration for the rings of the endcap.*

6.15.3 The Bhabha calibration constants

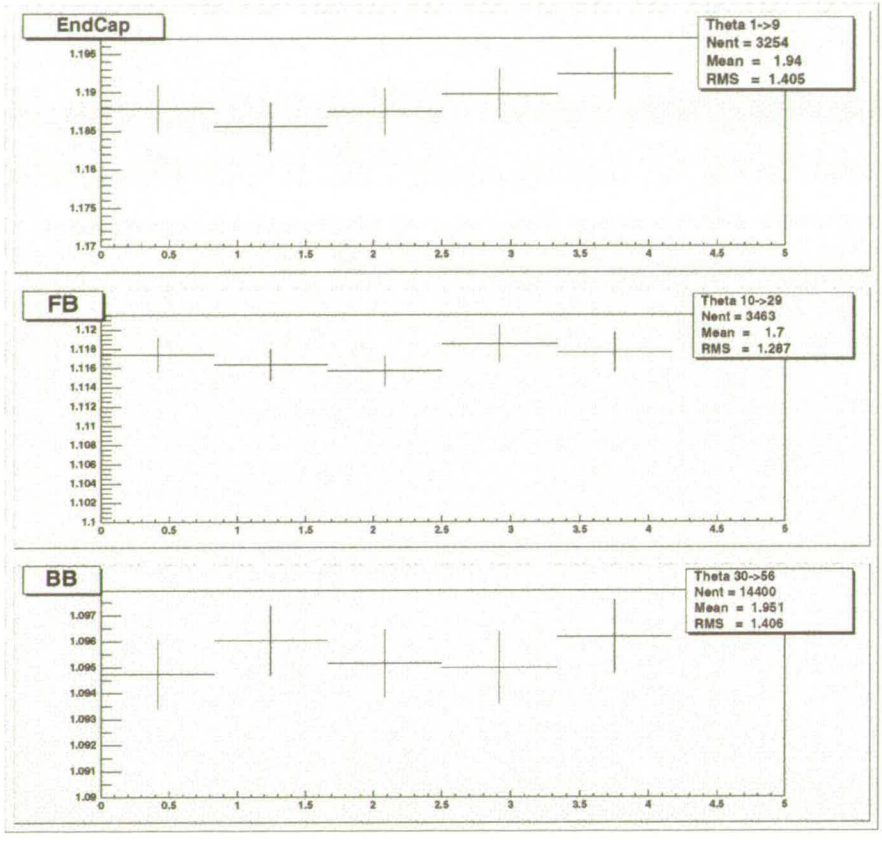

Figure 6-27. *The evolution of the Bhabha calibration constants over time*

It has not been possible so far to see a similar effect using the evolution of the Bhabha constants over time. This is shown in figure 6-27. It is curious that an effect has not been seen to date. The majority of the background from PEP-II is low energy photons which are absorbed in the front of crystals. Since the Bhabha events are higher energy and have correspondingly deeper showers this calibration may not be as sensitive to the radiation damage. However, the error bars on the calibration are still quite large and there may be an effect there, but it is less than that seen by the light pulser and the radioactive source system.

6.16 Linearity of the calorimeter electronics

The light pulser system can be used to check the linearity of the calorimeter electronics. In figures 6-28 and 6-29 two plots from the linearity check are shown. Between the plots a new improved feature extraction was added into the front-end. The new feature extraction has a 3rd order polynomial fitting algorithm whereas the original procedure used a parabolic fit. These plots show the change in the linearity check done by the light pulser system. They show the deviation for each crystal over the energy scale. The improvement by the new feature extraction can be seen, but there are still some improvements to be made to the linearity in the lower gain ranges of the electronics.

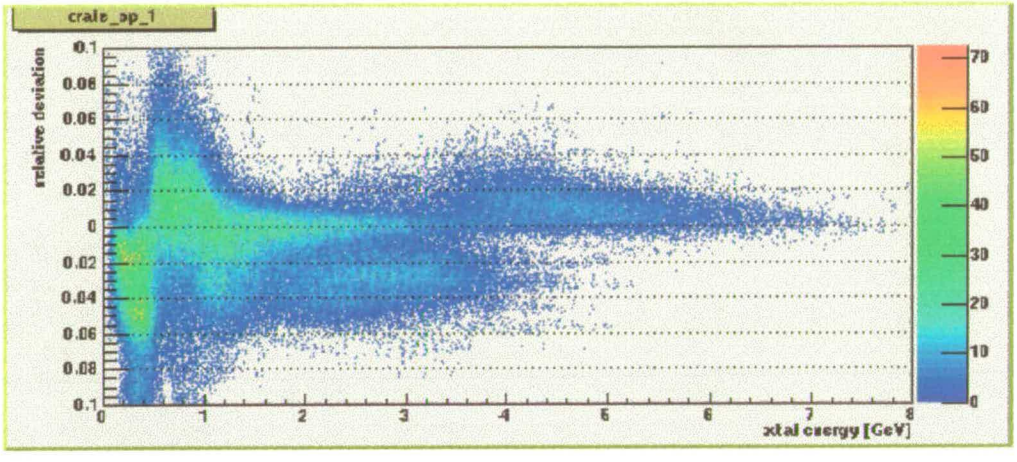

Figure 6-28. *Light pulser linearity check before the new feature extraction*

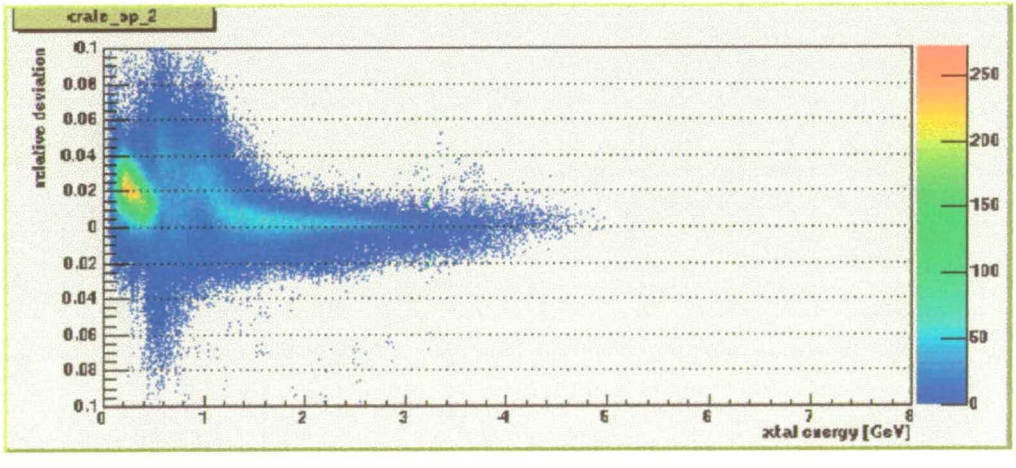

Figure 6-29. *Light pulser linearity check after the new feature extraction*

6.17 Radiation damage versus luminosity

It is possible using data from the inner ring of the endcap in September to obtain a correlation between the total integrated luminosity of data taken by *BABAR* and the differential radiation damage in the endcap. This radiation damage will affect any analyses or physics calibrations done using the endcap data. The correlation is shown in figure 6-30. These data correspond to a period of time of approximately 3 weeks. During this period PEP-II was producing a lot of data. This damage is consistent with expectations and can be extrapolated to a 20–30% change over the lifetime of *BABAR*, based on laboratory bench tests.

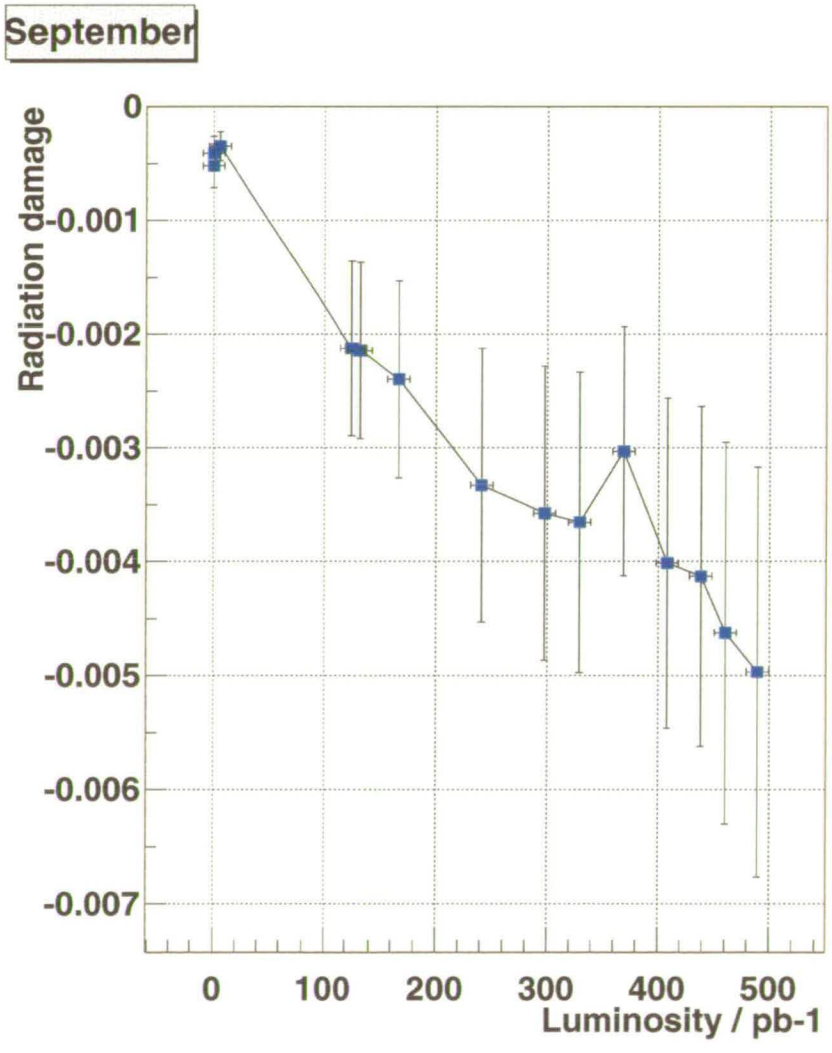

Figure 6-30. *The correlation between differential radiation damage in the endcap and the total integrated luminosity for September, 1999*

6.18 Chapter summary

In this chapter we have shown the performance of the light pulser system to date. We have closely studied the uniformity and stability of the system at various different stages in the light distribution. We have demonstrated that the light pulser can be used very effectively to diagnose electronics problems. In addition, the system can also be used to check the linearity of the calorimeter electronic readout. Preliminary radiation damage studies have been presented. These have been compared to the results from various other calibration procedures. Lastly, an initial correlation of radiation damage versus total integrated luminosity is presented.

7

Neutral particles in the calorimeter

7.1 Introduction

The electromagnetic calorimeter is an important part of the *BABAR* detector, and in order to realise its performance goals it must be well calibrated. In this chapter we will look briefly at some initial results from the calorimeter. This will give an indication of the status of the calibration and the functionality of the calorimeter for physics analysis studies.

A comparison of Bhabha electron events to Monte Carlo will be shown. The good agreement demonstrates that the calorimeter is well calibrated for high energy electrons. Studies of lower energy electrons are underway using radiative Bhabha events, and the results from this look promising. To identify differences between the photon and electron showers, results from $e^+e^- \rightarrow \gamma\gamma$ studies will be shown. These indicate that there may be a need for a separate calibration for neutral particles. To examine the status of the calibration at several different energy levels, several neutral pion peaks will be shown with different energy cuts. A short discussion of the importance of the calorimeter for physics studies will be given. Lastly, as a thesis summary, we will discuss the status of data-taking and the future outlook of the *BABAR* experiment.

7.2 Bhabha events

It is useful to look at the ratio of the energy measured for Bhabha events to that expected from Monte Carlo studies. Normally in a symmetric collider the energy expected is always the same in all directions. However, at PEP-II with asymmetric collisions it depends on the direction of the track angles and their correlation to the movement of the centre-of-mass. The Bhabhas therefore have different energies for the different parts of the detector. In figures 7-1 and 7-2 the ratio of the energy measured over the energy expected is shown for Monte Carlo and real data. The agreement is not so good in the backward barrel. This is due to an imperfect electronics calibration in this range and also a recently discovered cable swap. The Monte Carlo calculations are done without the quartz bars in the DIRC barrel, whereas the data are with the quartz bars in place.

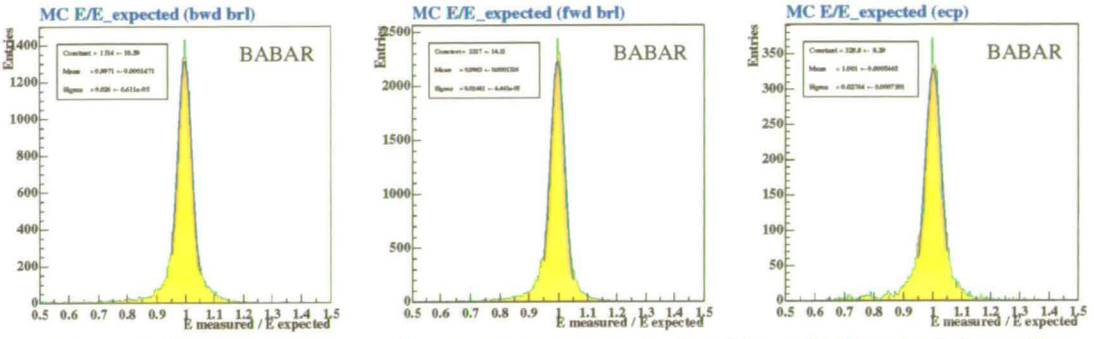

Figure 7-1. *Energy measured over energy expected using Monte Carlo calculations. The detector is broken up into three parts: the backward barrel, forward barrel, and the endcap*

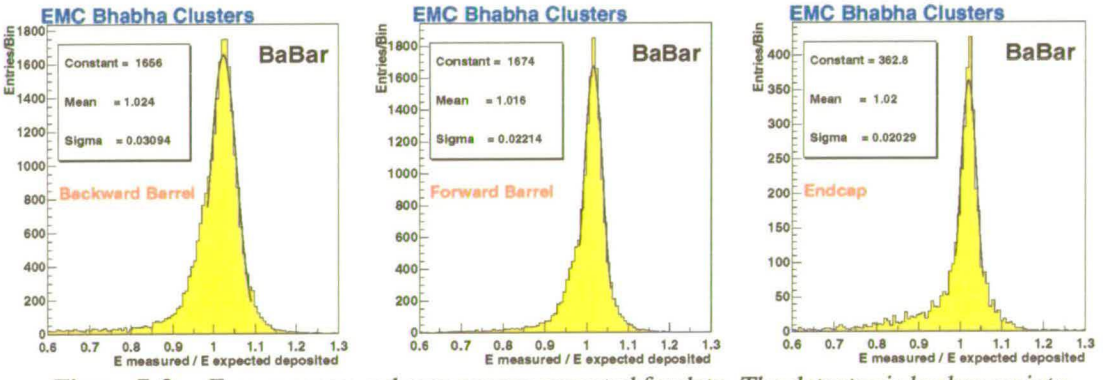

Figure 7-2. *Energy measured over energy expected for data. The detector is broken up into three parts: the backward barrel, forward barrel, and the endcap*

7.3 Radiative Bhabha events

The high energy electrons coming from Bhabha events can only be used for studying one end of the energy scale. It is important to look at electrons coming from radiative Bhabha events to improve electron identification at lower energies. Electron selection is achieved by cuts on the E/p ratio for particles, cuts on shower shape variables, and cuts on dE/dx.

In figure 7-3 the E over p distribution is shown for electrons at lower momentum than Bhabha electrons. The grey distribution is from before the October 1999 shutdown of *BABAR* and the red distribution is after the shutdown. This clearly shows the improvement made due to the October shutdown repairs and calibrations. There is still a lot of work being done in this area of the calibration and the position of the peak moves around depending upon which calibration or energy correction is being used.

There are electrons with low E/p in all momentum ranges. Examples can be seen in the low E/p tail in figure 7-3. These are due to hardware problems in the calorimeter *i.e.* swapped or dead readout fibres, or regions which were masked out due to noise. However, most of these effects were repaired during the October 1999 shutdown.

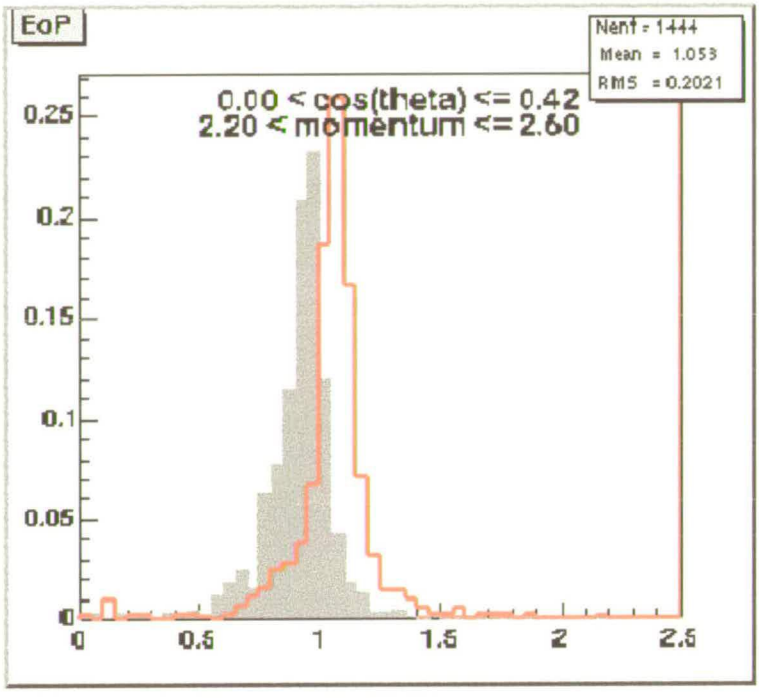

Figure 7-3. *E/p distributions for electrons in the momentum range 2.2 GeV to 2.6 GeV. The grey distribution is before the October 1999 shutdown and the red distribution is after the shutdown.*

7.4 Gamma gamma events

At energies greater than 10 MeV the interaction of photons in the calorimeter is via pair production, and the interaction of electrons is via bremsstrahlung. An electromagnetic shower is produced by an alternating sequence of these two types of interactions, leading to similar shower shapes for incident electrons and photons. The shower energy calibration for electrons and photons should be very similar and depends on Monte-Carlo studies. Radiation damage in the calorimeter is produced primarily due to low energy photons coming from PEP-II. Therefore the majority of the radiation damage occurs in the very front of the calorimeter crystals *i.e.* within the first radiation length.

It is important to check whether or not the Bhabha calibration constants are valid for high energy photons. To examine this studies were undertaken [72] using data sets of $e^+e^- \to \gamma\gamma$ events from Monte Carlo and data. In figure 7-4 the ratio of the central crystal energy to the sum of the nine nearest neighbour crystals is shown. In figure 7-5 the ratio of the sum of nine crystals to the sum of the 25 next-to-nearest neighbour crystals is taken. Both plots show the comparison of data to Monte Carlo. The good correlation demonstrates that the shower shapes for photons are quite accurate. There are slightly longer low energy tails for the data which may indicate that leakage may not be quite understood.

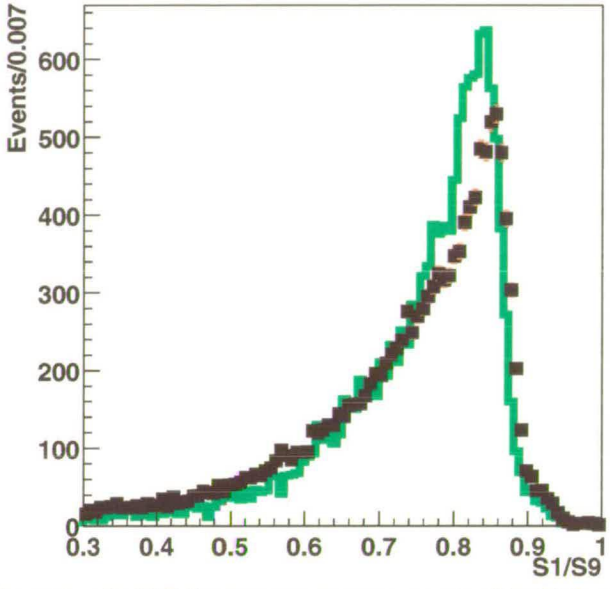

Figure 7-4. *The ratio of s1/s9 for gamma-gamma events (black) in the calorimeter compared to Monte Carlo predictions (green)*

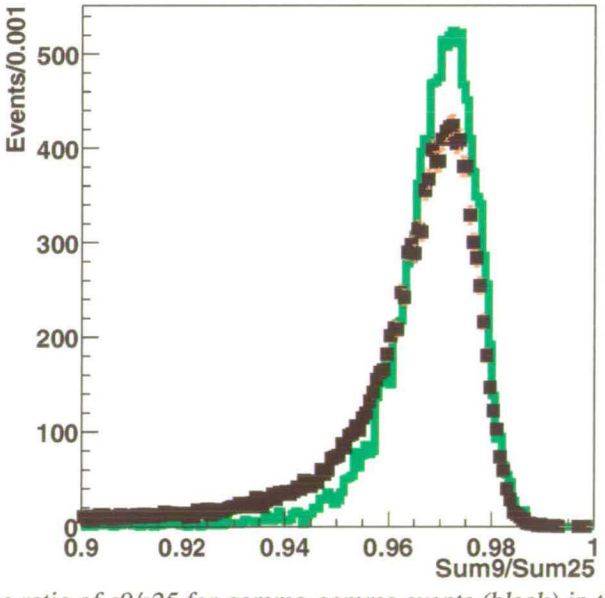

Figure 7-5. *The ratio of s9/s25 for gamma-gamma events (black) in the calorimeter compared to Monte Carlo predictions (green)*

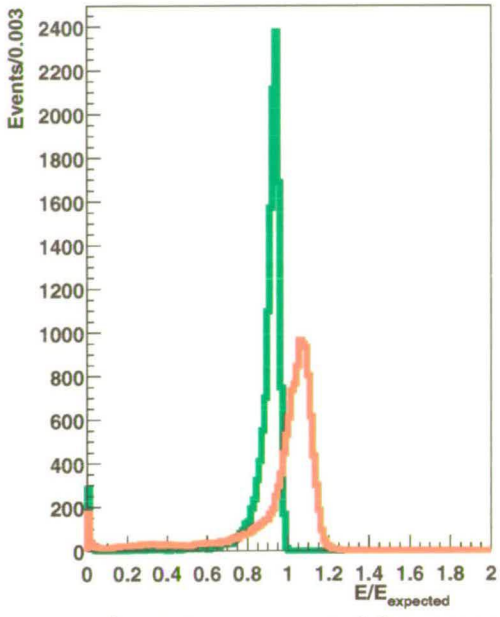

Figure 7-6. *Energy measured over energy expected for gamma-gamma events (red) and Monte Carlo events (green)*

In figure 7-6 the ratio of energy measured, over energy expected from Monte Carlo (s9 Bhabha calibration constants), is shown for $e^+e^- \to \gamma\gamma$ data (red) and Monte Carlo (green). There is clearly a discrepancy. The Bhabha calibration depends on the energy predicted from Monte Carlo and this energy predicted appears to be different for photons. This may be due to dE/dx losses in the drift chamber, and DIRC, not being completely understood. The amount of energy deposited in the calorimeter will depend on the bremsstrahlung/pair production encountered in the prior matter and this depends on the detailed kinematics *i.e.* the angle of the particles. The conclusion is that different shower energy calibrations may be required for electrons and photons.

7.5 Neutral pion width and relation to calibration

The ability to reconstruct neutral pions is an important part of the *BABAR* experiment. To achieve a narrow π^0 peak requires that the calorimeter be well calibrated and that the shower energy calibration is correct. The decay of boosted neutral pions produces photons covering a wide range of energies. Therefore the energy reconstructed by the calorimeter must be correct over a large energy range.

In figure 7-7 three neutral pion mass peaks are shown. They have energy cuts of $E_{\gamma\gamma} > 300\,\text{MeV}$, $E_{\gamma\gamma} > 500\,\text{MeV}$, and $E_{\gamma\gamma} > 1\,\text{GeV}$. The design width of the π^0 peak given by

Monte Carlo is 5 MeV indicating that there is still some work to be achieved. This could be due to the high energy photon problems which were discussed in the previous section. The plots shown are from 12th December 1999. They show that the π^0 mass is correct and that the calorimeter is calibrated.

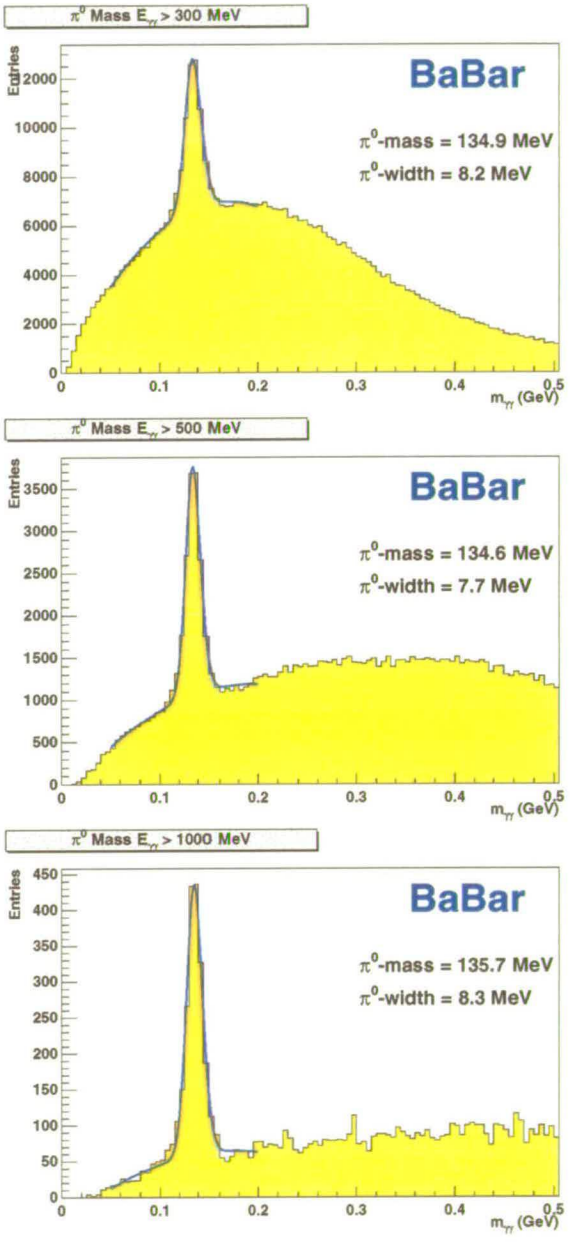

Figure 7-7. *π^0 mass peaks for a range of different energy cuts in the calorimeter*

7.6 η^0 mass peak

In figure 7-8 a preliminary η^0 mass peak is shown. This was one of the first η^0 mass peaks produced and was achieved using data taken in June 1999 immediately after the start of *BABAR* commencing to take data. This was prior to many of the later improvements and the correct calibration. Recent studies have produced η mass peaks at 547 MeV.

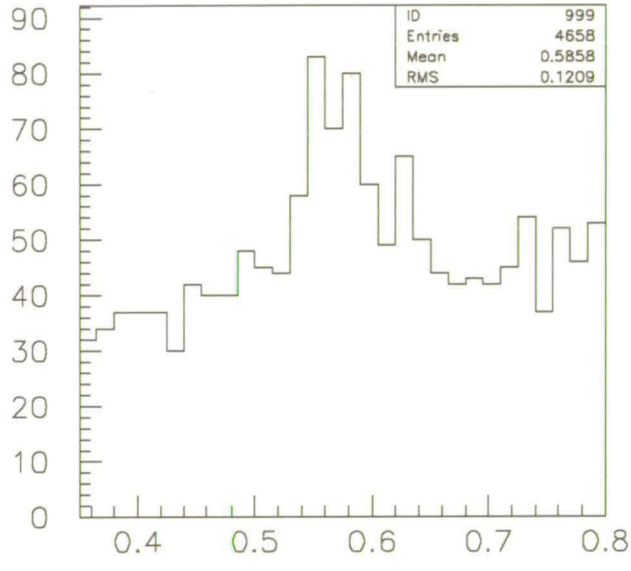

Figure 7-8. *Preliminary η^0 mass peak*

7.7 The calorimeter and physics analysis

It has been mentioned several times that the *BABAR* calorimeter is a vital part of the experiment. The main goal of the *BABAR* experiment is to study B decays in great detail and to make as many precise measurements as possible. This is necessary whether or not we are looking at CP violation, rare B decays, $|V_{cb}|$, $|V_{ub}|$, or something else. Generic B decays produce on average about 5.5 photons and 5.5 charged tracks. Therefore without the calorimeter many B decay measurements are impossible.

7.7.1 The importance of electron identification

In addition to photon detection the calorimeter is vital for electron identification using the ratio of energy measured by the calorimeter to the momentum measured by the drift chamber (E/p).

This is crucial to have a good efficiency for any B decays having charmonium final states ($J/\psi \rightarrow e^+e^-$). The electron identification is also crucial for tagging the B flavour using leptons. These two things are key parts of the measurement of $\sin 2\beta$ using $B^0 \rightarrow J/\psi K^0_S$.

To measure $|V_{cb}|$ and $|V_{ub}|$ requires that semileptonic decays, such as $B \rightarrow D^* l\nu$ and $B \rightarrow \rho l\nu$, are well reconstructed. To achieve good statistics and to make a correct measurement requires good electron identification.

The measurement of B mixing is another crucial part of making a CP violation measurement and is also an important measurement in itself. This must be done using dileptons to achieve good statistics. Electron identification from the calorimeter is again crucial for this measurement.

7.7.2 The importance of neutral pion reconstruction

The correct reconstruction of neutral pions is necessary for many B decay measurements. An example is $B \rightarrow J/\psi K^*$, from which CP violation and $\sin 2\beta$ may be measured. To reconstruct the K^* using the $K^* \rightarrow K^0_S\pi^0$ decay requires the correct reconstruction of the neutral pion.

There are many rare hadronic decays such as $B^+ \rightarrow \pi^+\pi^0$, $B^0 \rightarrow \pi^0\pi^0$, and $B^0 \rightarrow \rho\pi$ which contain neutral pions. The $B^+ \rightarrow \pi^+\pi^0$ is particularly interesting to look at. The total decay rate is expected to be the same for $B^+ \rightarrow \pi^+\pi^0$ and $B^- \rightarrow \pi^-\pi^0$. Any large CP asymmetries measured here would contradict the standard model. $B^0 \rightarrow \pi^0\pi^0$ and $B^0 \rightarrow \rho\pi$ can both be used to measure the angle α of the unitarity triangle. $B^0 \rightarrow \rho\pi$ provides a way to measure α using $B \rightarrow \pi\pi\pi$ rather than $B \rightarrow \pi\pi$ channels. It is interesting to note that $B^0 \rightarrow \rho^+\pi^-$, $B^0 \rightarrow \rho^-\pi^+$, and $B^0 \rightarrow \rho^0\pi^0$ all result in the same $\pi^+\pi^-\pi^0$ final state. The calorimeter is vital to make it possible to measure any of these rare decays.

7.7.3 The importance of high energy photon reconstruction

High energy photon reconstruction is important for rare B decays which involve radiative penguins. Some examples are the exclusive decays $B^0 \rightarrow K^*\gamma$, $B^0 \rightarrow \rho\gamma$, and the inclusive $b \rightarrow s\gamma$ transitions. $B^0 \rightarrow \rho\gamma$ in particular has not been measured to date and would provide information on the ratio $|V_{td}|$ to $|V_{ts}|$ which can only otherwise be measured from the ratio of B_d mixing to B_s mixing. BABAR is an ideal environment to measure this because the DIRC provides the K/π discrimination which is necessary for this analysis.

7.8 Thesis summary and future outlook

The *BABAR* detector and PEP-II have now been fully built and commissioned. Data taking commenced in early May 1999 and was followed by a very successful running period. During September the machine recorded a world record instantaneous luminosity of $2 \times 10^{33}\,\mathrm{cm}^{-2}\mathrm{s}^{-1}$. The highest daily integrated luminosity was $60\,\mathrm{pb}^{-1}$, and the total data sample taken on tape was $1.7\,\mathrm{fb}^{-1}$. The total luminosity delivered was over $2\,\mathrm{fb}^{-1}$. A plot showing the evolution of the total integrated luminosity is shown in figure 7-9. The period of the most intense data taking is the same period of data which I have used for the light pulser analysis studies.

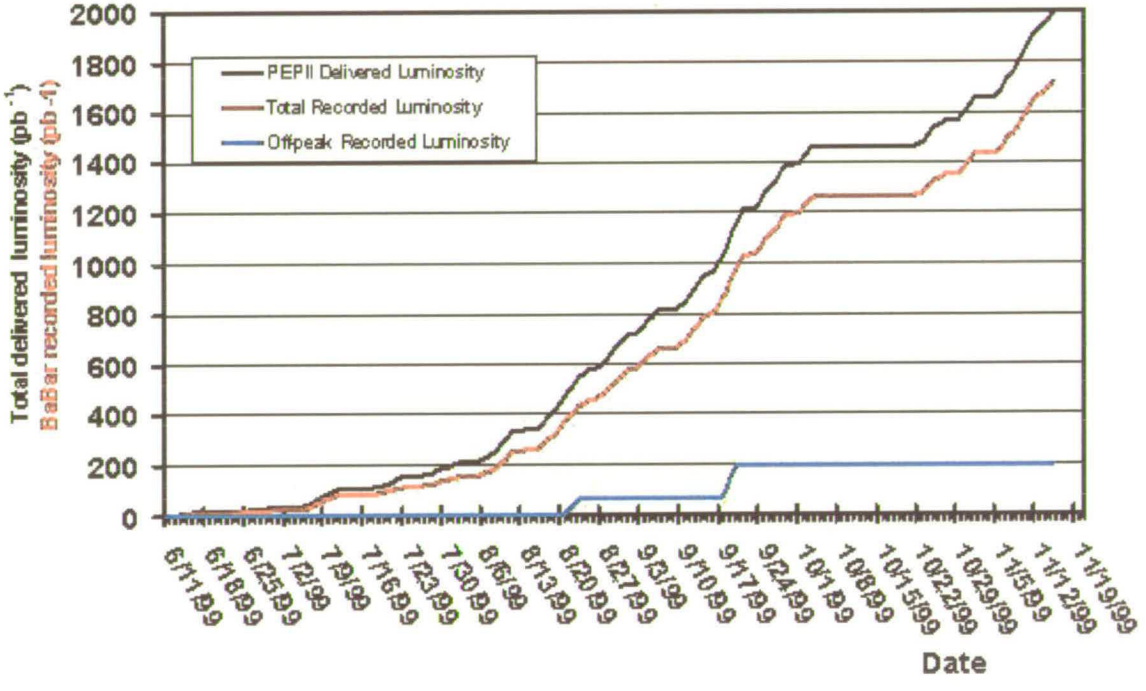

Figure 7-9. *The total integrated luminosity of BABAR as a function of time*

The light pulser calibration and monitoring system is now complete and fully commissioned. There are some hardware changes still to occur to better implement the linearity check of the calorimeter electronics. The neutral density filter settings need to be fine tuned to carefully look at the range switching boundaries of the CARE chip to closely test linearity at these points.

The calorimeter has been well calibrated using a variety of methods, but there is still a lot of work to be done. There are discrepancies of 15% between the calibration constants coming from the liquid source calibration and the Bhabha calibration which need to be understood.

There is still a lot of work to be done in the areas of reconstructing high energy photons and electron identification.

The *BABAR* experiment has started to take data again and has just completed an energy scan with PEP-II. The PEP-II storage ring looks set to break many new records by delivering an unprecedented luminosity in 2000. The performance of the machine is expected to improve steadily with the luminosity design goals being met in 2000. A correct B mixing measurement is expected for the summer of 2000 and a possible *CP* violation measurement using the golden channel $B \to J/\psi K_S^0$ shortly afterwards.

References

[1] V.F. Weisskopf and E.P. Wigner. *Zeitschrift für Physik*, 63(1930):54. In German.

[2] V.F. Weisskopf and E.P. Wigner. *Zeitschrift für Physik*, 65(1930):18. In German.

[3] G. Feinberg and S. Weinberg. *Nuovo Cimento*, 16(1959):571.

[4] A. Pais. *Phys. Rev.*, 86(1952):663.

[5] M. Gell-Mann. *Phys. Rev.*, 92(1953):833.

[6] M. Gell-Mann and A. Pais. *Phys. Rev.*, 97(1955):1387.

[7] K. Lande et al. *Phys. Rev.*, D103(1956):1901.

[8] C. Caso et al. Review of particle physics. *Eur. Phys. J.*, C3(1998).

[9] V.L. Fitch J.H. Christenson, J.W. Cronin and R. Turlay. *Phys. Rev. Lett.*, 13(1964):138.

[10] R.M. Barnett et al. Review of particle physics. *Phys. Rev.*, D54(1996).

[11] K.M. Watson. *Phys. Rev.*, D95(1954):228.

[12] A. Alavi-Harati and others [KTeV collaboration]. Observation of direct *CP* violation in $K_{S,L} \to \pi\pi$ decays. *Phys. Rev. Lett.*, 83(1999):22.

[13] A. Ceccucci. New measurement of direct *CP* violation in two pion decays of neutral kaons by experiment NA48 at CERN. *CERN particle physics seminar*, (2000).

[14] G.D. Barr and others [NA31 Collaboration]. *Phys. Lett.*, B317(1993):233.

[15] Yosef Nir. CP violation in and beyond the standard model. *SLAC Summer Institute*, (1999). hep-ph/9911321.

[16] M. Neubert. B physics and CP violation. *Int. J. Mod. Phys.*, A11(1996):4173–4240. hep-ph/9604412.

[17] M. Kobayashi and T. Maskawa. *CP* violation in the renormalizable theory of weak interactions. *Prog. Theor. Phys.*, 49(1973):652.

[18] N. Cabibbo. *Phys. Rev. Lett.*, 10(1963):531.

[19] C. Jarlskog. *Phys. Rev. Lett.*, 55(1985):1039.

[20] L. Wolfenstein. *Phys. Rev. Lett.*, 51(1983):1945.

[21] J.P. Silva G.C. Branco, L. Lavoura. *CP violation*, chapter 18. Oxford University Press, 1999.

[22] P. F. Harrison ed. and H. R. Quinn ed. *The BABAR physics book: physics at an asymmetric B factory*. Papers from workshop on physics at an asymmetric B factory (BaBar collaboration meeting), Rome, Italy, 11-14 Nov 1996, Princeton, NJ, 17-20 Mar 1997, Orsay, France, 16-19 Jun 1997 and Pasadena, CA, 22-24 Sep 1997.

[23] PEP-II: an asymmetric B Factory. Conceptual design report. June 1993.

[24] P. J. Oddone. Linear collider $B\overline{B}$ factory conceptual design. In D. Stork, editor, *Proceedings of the UCLA workshop*, page 243. World Scientific, 1987.

[25] D. Hitlin. The physics program of a high luminosity asymmetric B factory at SLAC. SLAC-0353.

[26] Tatsuya Nakada. Prospects for a CP violation experiment with an asymmetric e+ e- B meson factory. Invited talk at rencontres de Moriond, electroweak interactions and unified theories, Les Arcs, France, Mar 15-22, 1992.

[27] D. Hitlin et al. Workshop on physics and detector issues for a high luminosity asymmetric B factory at SLAC, January - June 1990. Proc. of workshop on physics and detector issues for a high luminosity asymmetric B factory at SLAC, encompasing the period Jan 26 to Jun 8, 1990. SLAC-0400.

[28] Stuart Henderson. Beam backgrounds at CLEO: design and performance of the CESR high luminosity interaction region. CLNS-97-1528.

[29] A. Snyder. Effect of vertex cuts on *CP* reach. *BABAR Note 177*, (1994).

[30] J. D. Richman. The *BABAR* silicon vertex tracker. *Nucl. Instr. and Methods* , A409(1998).

[31] F. Forti. TRACKERR studies for optimization of vertex detector resolution. *BABAR Note 195*, (1994).

[32] R. Johnson et al. Silicon vertex detector readout chip, requirement specification. *BABAR Note 213*, (1995).

[33] R. Johnson et al. Silicon vertex detector readout chip (target design specifications). *BABAR Note 214*, (1995).

[34] V. Re et al. The rad-hard readout system of the BaBar silicon vertex tracker. *Nucl. Instrum. Meth.*, A409(1998):354.

[35] A. Boucham et al. The BaBar drift chamber project. *Nucl. Instrum. Meth.*, A409(1998):46.

[36] G. Sciolla et al. The BaBar drift chamber. *Nucl. Instrum. Meth.*, A419(1998):310.

[37] D. Coupal et al. Drift chamber electronics system description. *Drift Chamber Technical Note*, (1997). TNDC-97-68 v4.0.

[38] J. Albert et al. Electronics for the BaBar central drift chamber. (1998). Contributed to IEEE 1998 Nuclear Science Symposium (NSS) and Medical Imaging Conference (MIC), Toronto, Ontario, Canada, 8-14 Nov 1998.

[39] D. Boutigny et al. Report on the status & analysis of the *BABAR* drift chamber (august cosmic Run. *BABAR Note 469*, (1998).

[40] C. Lu et al. Detection of internally reflected Čerenkov light, results from the *BABAR* DIRC prototype. *Nucl. Instrum. Meth.*, A371(1996):82.

[41] I. Adam et al. An internally reflecting Čerenkov detector (DIRC): properties of the fused silica radiators. *IEEE Trans. Nucl. Sci.*, 45(1998):450.

[42] R. Aleksan et al. Test of a large scale prototype of the DIRC, a Čerenkov imaging detector based on total internal reflection for BaBar at PEP-II. *Nucl. Instrum. Meth.*, A397(1997):261.

[43] I. Adam et al. DIRC, the internally reflecting ring imaging Čerenkov detector for *BABAR*. *IEEE Trans. Nucl. Sci.*, 45(1998):657. hep-ex/9712001.

[44] P. Bailly et al. A 16-channel digital TDC chip with internal buffering and selective readout for the DIRC Čerenkov counter of the BaBar experiment. (1999). hep-ex/9902015.

[45] P. Bailly et al. BaBar DIRC electronics front end chain. Talk given at 3rd Workshop on Electronics for LHC Experiments, London, England, 22-26 Sep 1997.

[46] P. Bailly et al. DIRC electronics. *BABAR Note 469*, (1996).

[47] Y. Kubota et al. The CLEO II detector. *Nucl. Instrum. Meth.*, (1992).

[48] LEAR experiment PS-197: status report and further activities. CERN-SPSLC-92-37.

[49] J. Brose, G. Dahlinger, and R. Waldi. The light yield of CsI(T1) crystals. *BABAR Note 320.*

[50] G. Haller and Freytag D. Analog floating-point BiCMOS sampling chip and architecture of the *BABAR* CsI calorimeter front-end electronics system at the SLAC B-Factory. *BABAR Note 285*, (1996).

[51] Dieter Freytag. Calorimeter preamplifier final design review documents. *BABAR Note 362.*

[52] P. Sanders et al. Evaluation of the electromagnetic calorimeter single channel demonstrator. *BABAR Note 325.*

[53] J. Brose et al. The performance of the photodiode readout of the barrel calorimeter crystals. *BABAR Note 452.*

[54] L. Lista and S. Mele. Study of the iron segmentation optimization of the I.F.R. detector for μ/π discrimination. *BABAR Note 194.*

[55] F. Anulli et al. The muon and neutral hadron detector for BaBar. *Nucl. Instrum. Meth.*, A409(1998):542.

[56] R. Santonico and R. Cardarelli. Development of resistive plate counters. *Nucl. Instrum. Meth.*, 187(1981):377.

[57] R. Santonico, R. Cardarelli, A. Di Biagio, and A. Lucci. Progress in resistive plate counters. *Nucl. Instrum. Meth.*, A263(1988):20.

[58] V. Ammosov, V. Korablev, and R. Santonico. Induced charges and voltage signals in resistive plate chambers. IFVE-97-83.

[59] N. Cavallo et al. Front-end readout development for the IFR muon detctor at *BABAR*. *Nucl. Instrum. Meth.*, A409(1998):297–299.

[60] D. Piccolo. The IFR level 1 trigger system. *BABAR Note 420.*

[61] T.O'Connor et al. Design study for the *BABAR* superconducting solenoid. *BABAR Note 233*, (1995).

[62] N. Dyce and The *BABAR* trigger group others. The *BABAR* trigger system. (1997). V4.00.

[63] S. K. Gehrig. Design and simulated performance of the level 1 trigger system. *BABAR Note 380*, (1997).

[64] E. Frank et al. Architecture of the *BABAR* level 3 software trigger. *BABAR Note 463*, (1998).

[65] CsI Calorimeter Group. Calibration and monitoring for the BaBar calorimeter. *BaBar Preliminary Design Review*, (1996).

[66] D. Boutigny et al. BaBar technical design report. SLAC-R-0457.

[67] Roger J. Barlow et al. Results from the BaBar electromagnetic calorimeter beam test. *Nucl. Instrum. Meth.*, A420(1999):162.

[68] R. Zhu. CsI (Tl) radiation damage and quality improvement. *BABAR Note 166.*

[69] J. Brose and G. Dahlinger. Temperature dependence and radiation hardness of Cs (Tl) crystals. *BABAR Note 355.*

[70] N. J. Gunawardane. Investigation of the resolution of the *BABAR* electromagnetic calorimeter digital filter algorithms. *BABAR Note 487.*

[71] The Calorimeter Calibration Task Force. Use of radioactive photon sources with the *BABAR* electromagnetic calorimeter. *BABAR Note: 322*, (1996).

[72] Francesca di Lodovico. Private Communication.

[73] Jörg Heckmann. Aufbau und test eines lichtpulser-prototyps für das *BABAR*-kalorimeter. Master's thesis, Ruhr-Universität Bochum, October 1998.

[74] Jean Ossmann. *Le systeme de monitoring de haute precision du calorimetre electromagnetique de L'experience L3*. PhD thesis, Universite de Geneve, 1989.

[75] Thomas Deppermann. Simulation und messung der lichtintensitäten des lichtpulsersystems für den *BABAR*-Detektor. Master's thesis, Ruhr-Universität Bochum, May 1998.

[76] G. Eigen and B. Stugu. Private Communication.